An Investigation of Backgrounds in the DEAP-3600 Dark Matter Direct Detection Experiment

by

Laurelle Maria Veloce

A thesis submitted to the
Department of Physics, Engineering Physics & Astronomy
in conformity with the requirements for
the degree of Master of Science

Queen's University
Kingston, Ontario, Canada
October 2013

Abstract

Astronomical and cosmological observations reveal that the majority of the matter in our universe is made of an unknown, non-luminous substance called dark matter. Many experimental attempts are underway to directly detect particle dark matter, which is very difficult to measure due to the expected low interaction rate with normal matter. DEAP-3600 is a direct dark matter search experiment located two kilometres underground at SNOLAB, in Sudbury, Ontario. DEAP-3600 will make use of liquid argon as the detector material, which scintillates as charged particles pass through. The work presented here is an investigation of expected background sources in the DEAP detector.

Because DEAP-3600 is a noble liquid-based experiment, a thin film of [1,1,4,4]-tetraphenyl-[1,3]-butadiene (TPB) is coated on the detector walls to shift the scintillation peak from the UV to visible regime for detection. However, alphas passing through TPB produce scintillation signals which can mimic recoil events. Because scintillation properties can change with temperature, we have conducted an investigation of alpha-induced TPB scintillation at temperatures ranging from 300 K to 3.4 K. We were able to characterize the light yield and decay times, and demonstrated that these background events should be distinguishable from true recoil events in liquid argon, thus enabling DEAP-3600 to achieve higher dark matter sensitivity.

Additionally, we investigate the performance of the liquid argon purification systems, specifically the activated charcoal used for radon filtration. Previous measurements with the DEAP prototype experiment have demonstrated the necessity of removing radon from the argon prior to filling the detector, due to the release of contaminates from the argon storage systems. Charcoal radon filters are extremely efficient, however, if the emanation rate of the charcoal is too high, there is the possibility of re-contamination. We performed a measurement of the radon emanation rate of a charcoal sample using a radon emanation and extraction system at Queens University. We demonstrated that the emanation rate of the charcoal was consistent with zero. We also show that the number of residual radon atoms which reach the detector would not be an issue for DEAP-3600.

Acknowledgments

First and foremost, I must thank Dr. Tony Noble. It is no exaggeration to say that without his expertise, guidance, and support, this thesis would not have been possible. Thanks also to the DEAP collaboration for their help and advice, and of course for the opportunity to work on such an exciting project. Thank you especially to Marcin Kuzniak for his invaluable help with the TPB scintillation analysis (and with the painful process of debugging my Root macros), and also to Wolfgang Rau for his advice and guidance with the radon emanation process. Special thanks also to Tina Pollmann, Mark Ward, Mark Boulay, David Bearse, Rob Gagnon, and Bei Cai. My time at Queen's University was much more enjoyable thanks to the antics of my officemates: Kedar Page, Matt Walker, and Alvine Kamaha; and my fellow DEAP graduate students Corina Natais, Paradorn Pasuthip, and Ben Broerman. Finally, my sincerest thanks to my parents, grandparents, and family for always believing in me. And, of course, thank you to Alex for always being there!

Contents

List of Tables

List of Figures

Glossary of Terms

AV Acrylic Vessel

CDMS Cryogenic Dark Matter Search

CERN Conseil Européen pour la Recherche Nucléaire (European Organization for Nuclear Research)

CMB Cosmic Microwave Background

CoGeNT Coherent Germanium Neutrino Technology

CRESST Cryogenic Rare Event Search with Superconducting Thermometers

CP Charge-Parity

DAMA/LIBRA DArk MAtter / Large sodium Iodide Bulk for RAre processe

DEAP Dark matter Experiment using Argon Pulse-shape discrimination

dru differential rate unit

DM Dark Matter

ERC Electron Recoil Contamination

HQE High Quantum Efficiency

LAr Liquid Argon

LET Linear Energy Transfer

LHC Large Hadron Collider

LUX Large Underground Xenon dark matter experiment

LY Light Yield

MACHOs MAssive Compact Halo Objects

MIPs Minimum Ionizing Particles

MOND Modified Newtonian Dynamics

MPCC Multiple Photon Counting Coincidence technique

MPV Most Probable Value

MSSM Minimalistic Supersymmetry

m.w.e meters water equivalent

PMT Photomultiplier Tubes

PSD Pulse Shape Discrimination

ROI Region Of Interest

singlePE Single Photoelectron Charge

SM Standard Model

SUSY Supersymmetry

TPB 1,1,4,4-tetraphenyl-1,3-butadiene

UV Ultraviolet

WIMPs Weakly Interacting Massive Particles

XENON XENON dark matter experiment

Λ**CDM** Lambda-Cold Dark Matter

Chapter 1

Introduction

The existence and nature of so-called "Dark Matter" has been a puzzling and controversial topic in physics for the last 80 years. The presence of dark matter in the universe is revealed through its gravitational interactions with ordinary matter in the form of stars, galaxies, and galaxy clusters. There are many well-motivated reasons which indicate that dark matter is made of particles; however, an unambiguous positive identification of such a particle here on Earth has not yet been accomplished. Many dark matter detection experiments have been built over the years, each striving to become more sensitive than the last. DEAP (Dark matter Experiment using Argon Pulse-shape discrimination) is one such experiment, making use of liquid argon as a detection medium. The work detailed in this thesis was done in support of the DEAP experimental program, and focuses on the mitigation of background signals in the detector. These signals are caused by conventional particles passing through the detector, which can mask the hoped-for dark matter signal.

In particular, I study the behaviour of a wavelength shifting compound, used in the DEAP experiment to shift the detector signal to an observable wavelength. However,

the scintillation properties of this compound at liquid argon temperatures (87 K) have not been studied before, and determining its scintillation properties in response to backgrounds at the appropriate temperatures is essential to our understanding of DEAP. This is one of the main objectives of this thesis.

Furthermore, a particularly troubling background signal can be present due to the introduction of radon into the detector. Radon is radioactive, inert, and because it is a gas, mobile, which is why considerable effort has gone into removal techniques of radon and its progenies from the detector medium. The construction and initial tests of a radon trap, designed to prevent radon from entering into the detector volume, is another background mitigation topic discussed in this thesis.

I begin with a broad discussion of dark matter in Chapter 2. I outline the evidence for the existence of dark matter, describe some possible candidate particles, and discuss detection techniques with a focus on direct detection. A summary of the present-day situation of the field concludes this chapter. Chapter 3 describes the DEAP dark matter detection program, and explains the motivation behind the research done for this thesis. In Chapter 4 I investigate alpha-induced scintillation of the organic wavelength shifter 1,1,4,4-tetraphenyl-1,3-butadiene at temperatures spanning 300 K to 3.4 K. Both the light yield and time constants of the scintillation were measured, and the results are discussed in the context of DEAP and other liquid noble detectors. Chapter 5 focuses on radon emanation measurements of the filtration medium of the DEAP-3600 radon trap. In Chapter 6 I summarize and provide an outline for future work.

Chapter 2

Dark Matter: A Review

One of the most compelling questions in modern physics is the nature of "Dark Matter" (DM), the name given to the mysterious substance which thus far has only revealed itself to us through its gravitational influence on luminous matter. The term was first coined by Fritz Zwicky, who discovered evidence of "missing" matter in galaxy clusters in the 1930s (for instance, [111, 112]). Observations and data from a wide range of sources point consistently to dark matter's existence, where it accounts for 26.8% of the energy-density of the Universe [40]. In comparison, only 4.9% of the mass-energy of the Universe is made of the kind of matter we are familiar with (baryonic matter), while the remainder is made of dark energy [40]. In spite of this, dark matter has proven to be notoriously difficult to study. All known particles have been excluded from being major contributions to the dark matter density, while conclusive evidence for the direct detection of dark matter particles has remained elusive. Because of this, dark matter is an exciting avenue of study for the pursuit of new physics. In this chapter, we shall provide an overview of dark matter physics, first summarizing the evidence for the existence of dark matter, then discussing dark

matter properties and candidate particles, and finally providing an overview on the methods of experimentally studying dark matter, with a focus on direct detection.

2.1 Evidence

2.1.1 Galaxy Clusters

In the 1930s, it was Fritz Zwicky who first noticed, by studying the Coma galaxy cluster, that the dynamics of clusters suggest that there is more matter present in these environments than could be accounted for using just the matter detectable by telescopes (i.e.: the luminous matter) [111]. In order to determine the amount of mass in a galaxy cluster, the orbital motions of the member galaxies are studied. Using the Virial theorem ($< K >= -\frac{1}{2} < U >$), the gravitational mass of a cluster can be determined using the distribution of the radial velocities of its galaxies. Comparing the mass of a cluster obtained using detected light with the mass obtained gravitationally, the conclusion is that less than 13% of the mass of a cluster is made of visible matter [29].

Rather than using velocity dispersions, one can also study the mass of galaxy clusters using weak gravitational lensing [30]. The bullet cluster is a famous example (refer to Figure 2.1.1), and is often hailed as the smoking gun for evidence of non-baryonic dark matter. This cluster is actually the result of a collision between two individual galaxy clusters. By combining the optical, X-ray, and weak gravitational lensing observations of this cluster we find that the main part of the cluster reacts predominantly through gravity. This is in contrast to the characteristics of ionized hydrogen gas, which is the largest baryonic component of clusters, indicating that the

majority of the mass in galaxy clusters is non-baryonic "dark matter" [31]. Additionally, maps of the luminous and gravitational mass of the cluster demonstrate that the gravitational centre of mass is not located in the same place as the luminous centre of mass [31]. One attempt to explain anomalous gravitational observations without the use of dark matter is to introduce changes to Newtonion gravity on large scales (i.e.: **Mo**dified **N**ewtonian **D**ynamics, MOND). However, observations like the bullet cluster rule out many of these modified theories, as they can not easily explain the difference in centres of mass, and do not work at all distance scales.

Figure 2.1.1: The Bullet Cluster, where the distribution of hot gas (the dominant form of baryonic matter) is coloured red, and the gravitational centres of mass are in blue [80]. Because dark matter is weakly interacting, the dark matter halos of the parent clusters passed through each other after colliding, while the hot gas from the two clusters was slowed down due to interactions between baryons.

2.1.2 Galactic Rotation Curves

Galactic rotation curves are the classic example given when discussing evidence for the existence of dark matter. Rotation curves are plots of the rotational velocities of the stars and gas content of galaxies as a function of the distance from their

galactic centres. These curves are made using measurements of the 21 cm emission line of neutral hydrogen combined with optical surface photometry. This 21 cm line (1420 MHz) is particularly useful because neutral hydrogen is ubiquitous across the universe and is present in galaxies out to eight exponential disc scale lengths [1] beyond the optical disk [9], thus allowing for the investigation of galactic rotations outside of the visible portion of galaxies.

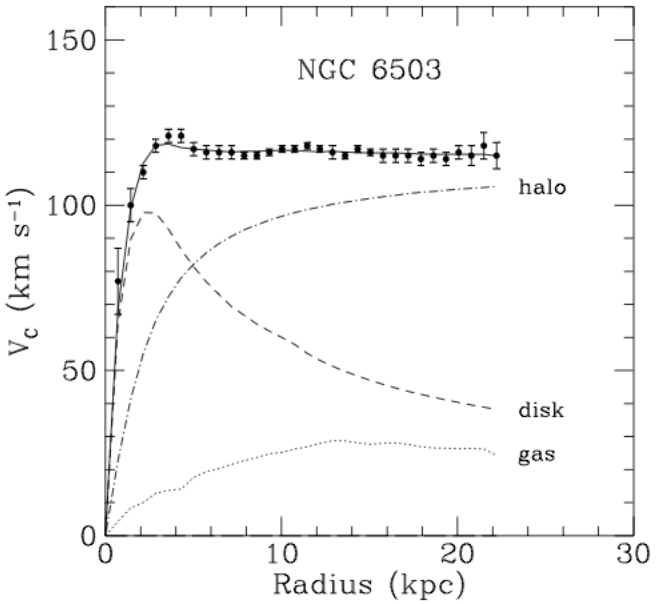

Figure 2.1.2: The rotation curve of galaxy NGC 6503, measured using the 21 cm line of neutral hydrogen (HI). The dashed and dotted lines represent the contributions of various galactic components, as labelled [9].

Rotation curves usually have a characteristic flat shape at large radii, beyond the visible disk (for instance, refer to Figure 2.1.2). This shape is in direct contradiction with the expected shape of a galactic rotation curve based only on the visible matter

[1] An exponential scale length is the radius at which the brightness of a galaxy has fallen off by a factor of e. The brightness follows the form $b = b_0 e^{-r/r_0}$ where b_0 is the brightness at the centre of the galaxy, and r_0 is the scale length.

contained within the galaxy. If we are to assume that the mass within a galaxy moves according to the observed distribution of matter, the calculation for expected rotational velocity is quite simple. Most of the matter is concentrated at the centre (i.e.: in the bulge), and so at radii outside the bulge we can equate the gravitational force to the centripetal force experienced by an orbiting mass:

$$\frac{GM_1M_2}{r^2} = M_2\frac{v^2}{r}$$

$$v = \sqrt{\frac{GM_1}{r}} \tag{2.1}$$

After some simple manipulation, we can see that $v \propto \frac{1}{\sqrt{r}}$, and so we expect the rotational velocity of a galaxy to fall off with radius, while observations show that this is not the case.

Since 1970, when Vera Rubin first observed the rotation curve of the Andromeda galaxy [96], many other curves have demonstrated similar characteristics [14], so much so that the discrepancies between theory and observation with regards to rotation curves is firmly established. The generally accepted explanation is the proposal of the presence of "dark" matter, which dominates the gravitational field in the outer regions of galaxies, thus causing the unexpected flat rotation curve (see for example [61]). Of course, one could also propose a break-down of the law of gravity at large scales to explain this discrepancy; however, as mentioned, these theories do not easily explain the bullet cluster findings discussed in the previous section, nor do they work for all distance scales.

2.1.3 The Cosmic Microwave Background

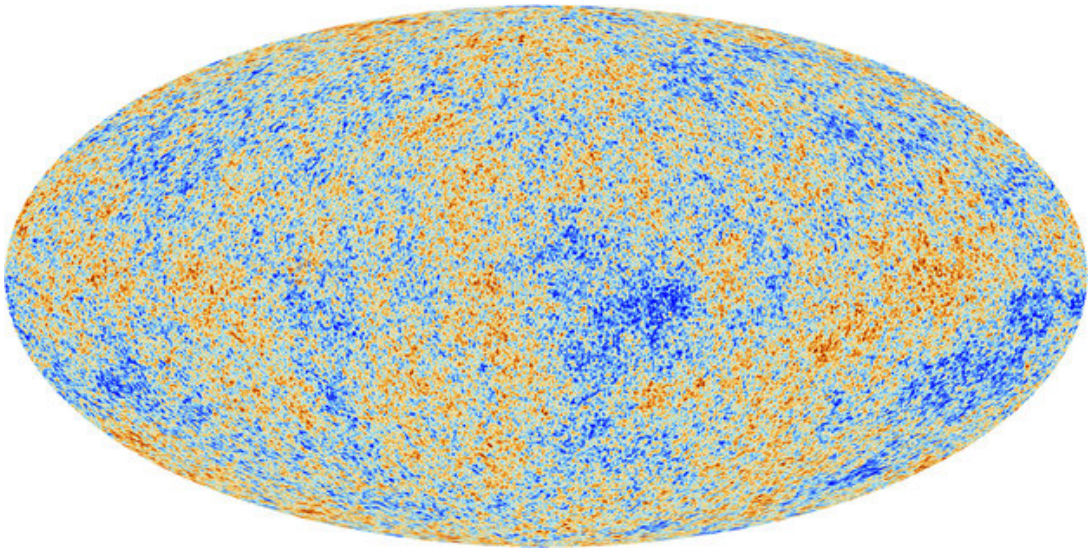

Figure 2.1.3: Map of CMB anisotropies from the Planck satellite [42].

The Cosmic Microwave Background (CMB) (Figure 2.1.3) is a remnant from the Big Bang and contains information on the conditions of the early universe. The most striking characteristics of the CMB are its omni-presence and constancy, which indicate that no single astronomical process could have produced it, and that it was formed long before the structure of our universe appeared [83]. Faint anisotropies are caused by conditions in the early universe, and so by studying the power spectrum of the CMB (the magnitude of the variations against angular size), patterns in the anisotropies can be interpreted (see Figure 2.1.4). The effects of dark matter manifest themselves in the ratios of the first three peaks of the power spectrum. The amounts of ordinary matter and dark matter can be determined in this way, while any leftover density is attributed to dark energy, which causes universal expansion [83], [10].

Cosmic microwave background measurements indicate that 68.3% of the universe

is made of dark energy (also confirmed through measurements of type 1A supernova [93]), 26.8% is made of dark matter, and the remaining is made of baryonic matter [40].

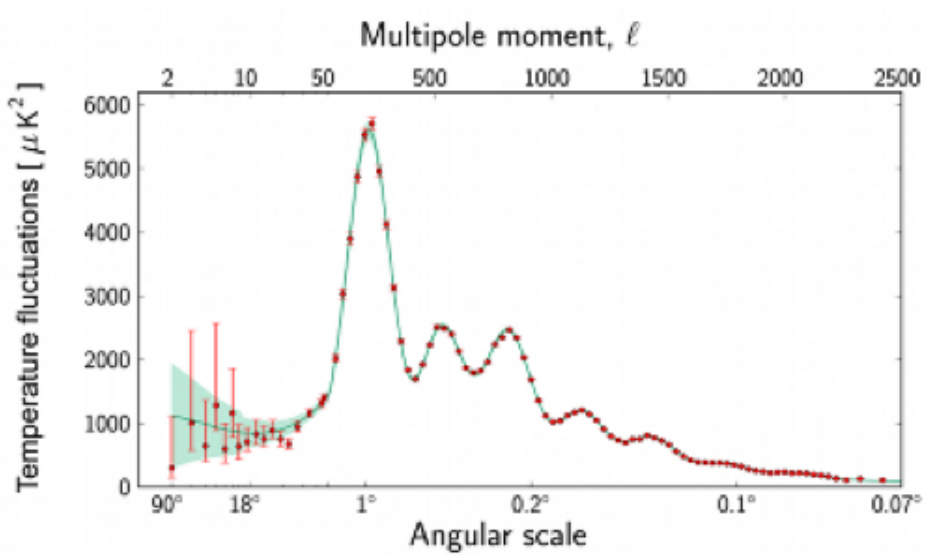

Figure 2.1.4: The power spectrum from the Planck satellite [42]. This shows the temperature fluctuations of the CMB detected at different angular scales across the sky. The largest scales, beginning at 90°, are on the left. The green curve represents the best fit of the standard model of cosmology to the data, while the pale green regions surrounding the curve represent variations to the model which also agree with the data.

2.2 Dark Matter Candidates

Although the existence of dark matter is very well-motivated, its exact nature has proven difficult to determine. Dark matter is so difficult to study precisely because it is "dark", i.e.: it does not emit light and so cannot be investigated using conventional techniques in observational astronomy. Distributions of dark matter (from gravitational observations) show that it is pervasive within galaxies, and yet dark

matter particles have never been detected here on Earth. From this we can conclude that dark matter does not interact via the electromagnetic or strong forces. Dark matter obviously has a gravitational influence, and may interact via the weak force as well [73]. Dark matter is also expected to be cold, or slow-moving (i.e.: non-relativistic) at the time of structure formation, in order to explain the structure, or "clumpiness", of the universe we observe today [34]. The currently favoured theory is that dark matter is made up of massive particles called WIMPs (Weakly Interacting Massive Particles) [73], but there are many other theoretically-motivated options which could also explain these observations.

Weakly Interacting Massive Particles (WIMPs) are attractive dark matter candidates which arise naturally from a range of theoretical frameworks. The idea that the Standard Model (SM) is an incomplete theory is well accepted within the physics community, and a myriad of theoretical "extensions" have been proposed which attempt to provide more complete explanations of our universe. WIMPs, as implied by their name, are particles which are weakly interacting with weak-scale mass. If we assume that WIMPs are thermal relics of the Big Bang, with several reasonable properties (for instance, a mass of about 100 GeV/c^2 and cross section of the scale of weak interactions), then the abundance of such a relic is close to the current abundance of dark matter in the universe [64]. By considering issues with electroweak symmetry breaking, such relic densities are naturally produced by WIMP candidates [25]. This is because extensions to the Standard Model which attempt to solve the hierarchy problem associated with electroweak symmetry breaking (for example, supersymmetry) predict particles which are weakly interacting, massive, and stable - exactly the characteristics which a WIMP particle must possess [101].

Of course, baryonic matter such as MACHOs (MAssive Compact Halo Objects which do not give off light, for example, brown dwarfs or neutron stars), or standard model neutrinos have been proposed as components of dark matter. However, experimental searches for MACHOs as well as stellar remnant limits demonstrate that faint astronomical objects cannot fulfill the place of exotic dark matter [46]. Standard model neutrinos also cannot be a major component of dark matter for a number of reasons. From recent observations, we know that neutrinos have very little mass [8]. Additionally, standard model neutrinos are hot (relativistic), collisionless particles, which would imply a top-down formation history of the structure in the Universe, where large structures form first and then split into smaller ones [14]. However, various observations indicate that our Universe formed from small "seeds" which merged to form larger structures (for instance, [17, 84]) and so neutrinos as a major component of dark matter cannot explain galactic structure [8].

Some non-baryonic dark matter candidates are listed below.

1. **Supersymmetric Particles**

   One well-motivated extension to the Standard Model is Supersymmetry (SUSY), which postulates the existence of a symmetry between fermions and force-carrying bosons. This essentially doubles the number of fundamental particles by providing a "supersymmetric" partner for each known elementary particle. The lightest supersymmetric particle, known as the neutralino, emerges naturally from minimal supersymmetric theories (MSSM). The neutralino is heavy (between 10 to 10 000 GeV), weakly interacting, and electrically neutral. This theoretical particle is not the only contender for dark matter, but because supersymmetric theories explain a host of other physics problems (for instance, the

mass hierarchy of fundamental particles), the neutralino has become a favourite dark matter candidate [75]. Supersymmetry also provides several other candidates for particle dark matter, for instance, sneutrinos, the superpartners of neutrinos [43] or gravitinos, superpartners of the graviton [44]. Of course, with the emergence of the Large Hadron Collider results, in which preliminary data show no evidence for SUSY, other standard model extensions are now receiving more attention.

2. **Axions**

   Axions arise from theories which attempt to find a solution to the strong CP violation problem (CP violation is not observed in strong interactions even though there is no reason that it should be forbidden). Introducing an extra scalar field solves this issue, and its corresponding "particle" is known as an axion. Axions are expected to be extremely weakly interacting. In the case of cold axion dark matter, they can be produced, for example, via the vacuum realignment mechanism, in contrast to the thermal production of WIMP particles [41]. Their mass is expected to fall anywhere between 10^{-6} and 10^{-2} eV [95]. It is possible to find a range of axion characteristics which satisfy all constraints, and so it remains a plausible dark matter candidate.

3. **Kaluza-Klein States**

   Kaluza-Klein theories arose from attempts to unify gravitation and electromagnetism by introducing a fifth dimension [58]. Kaluza-Klein states, a popular alternative to SUSY WIMP dark matter particles, are excitations of standard model fields, where particles propagate in extra spacetime dimensions [25]. Such

particles have an infinite tower of partner states [58]. In the case where all standard model particles can propagate in this way (so-called universal extra dimension theories), stable Kaluza-Klein partners become dark matter candidates [36]. These particles typically have the correct relic density, and it is possible to detect them through indirect or direct detection techniques [25].

It is important to note that dark matter is not necessarily made of a single kind of particle. For instance, as discussed above, neutrinos make up some fraction of dark matter but cannot account for all, or even a significant portion, of the dark matter density.

2.2.1 Dark Matter Detection

Because the existence of dark matter is inferred by its effects on luminous matter through astronomical observations, the detection of this substance would shed light on its important characteristics, including mass and cross section. There are essentially three approaches an experimentalist can take when trying to detect dark matter [11]:

1. **Create dark matter particles in accelerators on Earth**

   Refer to Figure 2.2.1, viewed right to left. Collider experiments look for new particles by annihilating known particles to create unknown ones. Some of these particles could conceivably be dark matter candidates, where their signature would be due to missing energy in interactions [107]. This is one of the main goals of the Large Hadron Collider (LHC) at CERN. However, it would be difficult to verify that the discovered particle is actually dark matter without confirmation from other measurements. So far, no dark matter candidates have been observed [59].

2. **The detection of products of dark matter interactions**

   Refer to Figure 2.2.1, viewed left to right. It is thought that dark matter particles may undergo interactions similar to baryonic matter, for instance annihilation interactions. Such processes could produce detectable final products in the form of exotic cosmic rays, including high-energy positrons, antiprotons, neutrinos, and gamma rays. This is perhaps the most convincing way to determine the make-up of dark matter halos. Searches for dark matter annihilation or decay products take place in areas where the dark matter density is likely to be large enough to produce an enhanced signal (for instance, at the centre of the Milky Way, in cluster environments, or in dwarf galaxies). The difficulty is that dark matter products must be extracted from other astronomical backgrounds. Some hints, in the form of a surplus of events, can therefore be explained with a variety of theoretical models [107].

3. **Detection of dark matter recoil interactions**

   Refer to Figure 2.2.1, viewed bottom to top. This method of detection involves the use of extremely sensitive detectors, which are typically very large and are built deep underground to take advantage of the natural shielding from cosmic rays provided by the Earth's crust. These detectors search for interactions between WIMP particles and detector nuclei, specifically the transfer of kinetic energy through scattering. The energy of the recoiling detector nucleus is measured by the detector. Because the energies are small and interactions are extremely rare, extracting dark matter recoil signals from backgrounds is extremely difficult [107].

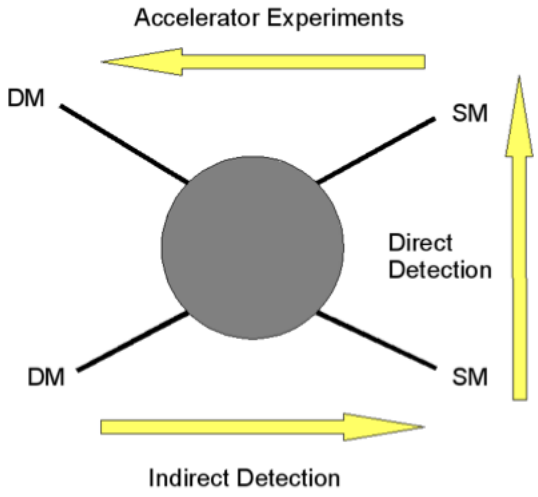

Figure 2.2.1: Schematic showing the different ways to approach dark matter detection [107].

All three techniques are crucial to the advancement of our understanding of dark matter particles. Ideally, both direct and indirect observations would find a particle of similar mass and characteristics, therefore providing strong confirmation of the results. This thesis focuses on direct dark matter detection, which is discussed in more detail in the following section.

2.3 Direct Detection

Direct detection experiments focus on observing scattering interactions between WIMPs and detector nuclei. These experiments look for WIMPs present in our solar neighbourhood, due to the dark matter halo surrounding our Milky Way galaxy. Because the nature of dark matter particles is unknown, direct detection experiments attempt to systematically test areas of the parameter space where WIMPs are expected to reside by building increasingly sensitive detectors.

2.3.1 Dark Matter Recoil Signal

It is assumed that WIMPs in the galactic halo behave according to the Standard Halo Model. This means that WIMPs behave like a gas with a Maxwell-Boltzmann velocity distribution, where their bulk velocity with respect to the Milky Way's rest frame is zero [45]. Therefore the motion of our solar system and the Earth with respect to the centre of the galaxy will be equivalent to the speed of the WIMPs which pass through Earth-bound detectors. Due to the gravitational pull of the Milky Way, the galactic disk (and therefore our solar system) rotates at about 220 km/s. The Earth rotates around the sun at a speed of 48 km/s. These produce the effective WIMP speed with respect to the Earth. The kinetic energy transferred to detector experiments is therefore on the order of 10-100 keV, with more events expected at lower energies [107]. Therefore, the lower the threshold of an experiment, the higher the WIMP rate is expected to be (see Figure 2.3.1).

The WIMP rate is expected to be extremely small, much less than 1 event per day per kilogram of target mass (specific rates depend on what substance is used as the target), while the ambient background signal is typically of the order 10^6 events per day per kg or higher [106]. This means that detectors must have a large mass, a low energy threshold (and consequently, excellent knowledge and control of background events), and they must run for a long time. In addition, sensitive background discrimination techniques must be developed to identify background particles, including beta, gamma, alpha, and neutron events.

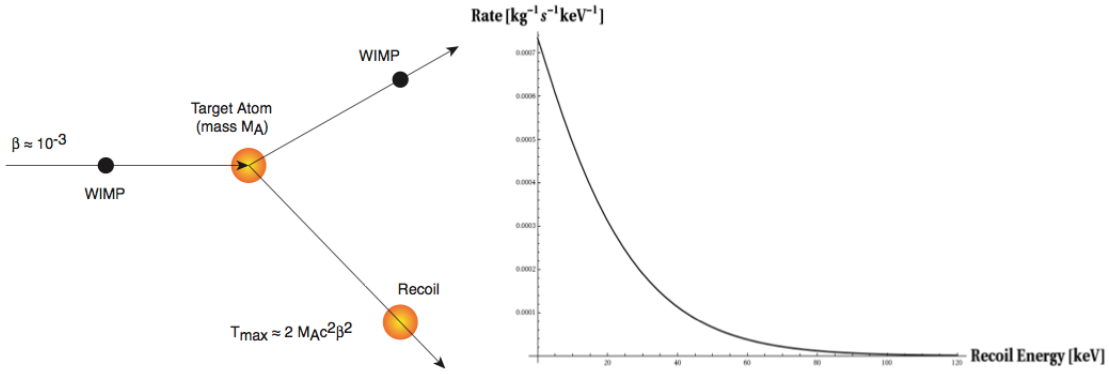

Figure 2.3.1: WIMPs collide elastically with the detector nuclei. The WIMP event rate increases with decreasing energy threshold [107].

The following discussion is from [67], unless otherwise cited.

The differential energy spectrum of WIMPs is expected to be featureless and smoothly decreasing. In the case normally assumed for the dark matter distribution,

$$\frac{dR}{dE_R} = \frac{R_0}{E_0 r} e^{\frac{-E_R}{E_0 r}} \tag{2.2}$$

where E_R is the energy of the recoiling target nucleus, E_0 is the most probable incident kinetic energy of a dark matter particle, $r = 4m_\chi m_T/(m_\chi + m_T)^2$ (where m_χ and m_T are the mass of the dark matter particle and target nuclei respectively), R is the event rate per unit mass, and R_0 is the total event rate:

$$\int_0^\infty \frac{dR}{dE_R}\, dE_R = R_0 \tag{2.3}$$

Units of $dR\,/\,dE_R$ are number of events per kg of detector mass per day of runtime per keV of energy; this is often referred to as the **d**ifferential **r**ate **u**nit (dru). The integrated total event rate for a specific detector (events per kg per day) is found by integrating the dru within the energy Region Of Interest (ROI). The total number of

events is the total event rate multiplied by the exposure of the experiment, where the exposure is the product of the detector's mass and runtime [57].

Dark matter experiments attempt to set increasingly strict limits on the differential rate, which can then be translated into a corresponding limit for the total event rate using Equation 2.2 for specific values of m_χ. The dark matter density and flux in the vicinity of the solar system can be estimated (see Table 2.1 for typical values), allowing for limits on R_0 to be converted into cross sections. Experimental limits are then typically depicted as contours on a plot of cross-section versus WIMP mass, normalized per nucleon for comparison between experiments.

Equation 2.2 is in reality much more complicated than what is shown above. Corrections to the differential rate must take into account:

1. the motions of the Earth around the Sun, and the solar system itself around the galaxy,
2. the detection efficiency for nuclear recoils in comparison to the detection efficiency for other interactions by the detector itself (i.e.: the true recoil energy differs from the observed energy by some factor),
3. different detection limits for different elements, should the target consist of more than one element,
4. resolution and threshold effects associated with the detector,
5. spin-independent or spin-dependent WIMP-nucleon interactions, and
6. form factor corrections.

Equation 2.2 can therefore be rewritten as,

$$\frac{dR}{dE}|_{\text{observed}} = R_0 S(E) F^2(E) I \tag{2.4}$$

where S is a modified spectral function to correct for #1-4 (deals with masses and kinematics), F is the form factor correction (#6), and I is an interaction function (#5) for spin-independent or -dependent interactions.

In-depth discussions of dark matter scattering interactions and direct detection can be found in, for example, [14], [56], or [67].

2.3.2 Velocity Distribution and Local Density

The velocity distribution of the dark matter halo is often assumed to be isotropic, spherical and Maxwellian:

$$f(v) = 4\pi v^2 (\frac{3}{2\pi\sigma})^{3/2} e^{-\frac{3v^2}{2\sigma^2}} \tag{2.5}$$

where σ is the velocity dispersion of the dark matter halo. In an isothermal system, the velocity dispersion of dark matter particles in our locality can be written in terms of the circular velocity v_0 of our Sun around the Milky Way, where $\sigma = 3v_0^2/2$ [45]. Of course, the velocity distribution is cut off at the escape velocity of our galaxy, v_{esc}, while only velocities larger than the minimum velocity, v_{min}, required to produce a signal in the dark matter detector will influence the rate seen by that detector. Therefore, the values that influence the dark matter rate are v_0, v_{esc} and v_{min}.

These values, along with the local dark matter density ρ_χ, must be determined though observation. These can be measured using our galactic rotation curve, but accurate values are difficult to obtain due to our location in the galaxy. Therefore observations of other galaxies with characteristics similar to our own are used to

Parameter	Definition	Value	Uncertainty	Source
ρ_χ	local DM density	0.3 GeV/cm^3	factor of 2	[67]
v_{esc}	galactic escape speed	544 km/s	$\approx$ 9%	[104]
v_0	dispersion velocity of DM	250 km/s	$\approx$10%	[99]
v_E	average speed of Earth relative to DM halo	263 km/s	$\approx$10%	[99]
Δv_E	amplitude of annual modulation of v_E	15 km/s	small	[99]

Table 2.1: Canonical values for galactic halo and velocity parameters [70].

estimate these values.

2.3.3 Kinematics

We now refine our earlier estimate for recoil energy due to the scattering interaction between a dark matter particle with speed v and a detector particle (see Figure **??**).

Using standard kinematics, the recoiling energy E_R is found to be:

$$E_R = E_i r \frac{(1 - \cos\theta)}{2} \tag{2.6}$$

where E_i is the incident kinetic energy of the dark matter particle. If we assume isotropic scattering (i.e.: scattering is uniform in $\cos\theta$), then the recoil energies are distributed uniformly between $E_R = 0$ to $E_i r$. We must therefore integrate over the range of incident energies [4]:

$$\frac{dR}{dE_R}(E_R) = \int_{E_{\min}}^{E_{\max}} \frac{dR(E_i)}{E_i r} \tag{2.7}$$

$E_{\max}$ corresponds to the escape velocity of our galaxy, while $E_{\min} \geqslant E_R/r$. dR is the event rate per unit mass, given by

$$dR = \frac{N_A}{A}\sigma v\, dn \tag{2.8}$$

where A is the atomic mass (AMU) of the target material, N_A is Avogadro's number, σ is the cross-section per nucleus, v is the speed of the dark matter particle, and dn is the differential particle density of dark matter:

$$dn = \frac{n_0}{k}\, f(v, v_E)\, d^3v\,. \tag{2.9}$$

Here v_E is the Earth's velocity relative to the dark matter halo, $n_0 = \rho_\chi/m_\chi$, and k is the normalization constant so that the integral of dn is n_0. R_0 is defined as the event rate per unit mass for $v_E = 0$ and $v_{esc} = \infty$. In this case, the integral of 2.8 is

$$R_0 = \frac{2}{\sqrt{\pi}}\frac{N_0}{A}\frac{\rho_\chi}{m_\chi}\sigma_0 v_0 \tag{2.10}$$

Note that the discussion in this section assumes collisions with zero momentum transfer, where the cross section remains constant (σ_0). Form factor corrections are discussed in the following section.

For the simplest case of $v_E = 0$, $v_{esc} = \infty$, integrating $\frac{dR}{dE_R}(E_R)$ yields equation 2.2. Correcting for v_{esc} introduces a maximum cut-off recoiling energy, while correcting for v_E introduces modulation effects into the expected rate (refer to [67] for in-depth derivations of these corrections). We simply present the numerical approximation

here. In this case, a local WIMP density of 0.4 $\mathrm{GeVc^{-2}cm^{-3}}$ and a galactic escape velocity of 600 km/s are assumed [14]:

$$\frac{dR}{dE_R} = c_1 \frac{R_0}{E_0 r} e^{-c_2 E_R / E_0 r} \tag{2.11}$$

where $c_1 = 0.751$, $c_2 = 0.561$, and R_0 is defined as in 2.10. The constant values c_1 and c_2 depend on the choice of WIMP density, escape velocity, and mean WIMP velocity. This is where the modulation of the WIMP rate (discussed below) appears [14].

2.3.4 Cross Section and Nuclear Form Factors

The expected shape of the WIMP spectrum is given by equation 2.11 multiplied by both the cross section and an additional term related to detector characteristics and defects. Using Fermi's Golden Rule, the cross section can be divided into σ_0 and the Form Factor, which is a term that contains the dependence on momentum transfer (specifically, the loss of coherence with increasing momentum transfer). From [56], the general differential cross section is,

$$\frac{d\sigma(q)}{dq^2} = \frac{\sigma_0}{4 m_r^2 v^2} F^2(q) \tag{2.12}$$

where q is the momentum transfer, σ_0 is the cross section when the momentum transfer is zero, v is the velocity of the WIMP relative to the target, $F^2(q)$ is the form factor (the Fourier transform of the nuclear density, normalized so that $F^2(0) = 1$), and m_r is the reduced mass:

$$m_r = \frac{m_T m_\chi}{m_T + m_\chi} \tag{2.13}$$

The form of Equation 2.12 depends on the nature of WIMP/quark interactions, which is determined by the choice of particle physics model. In general, however, the cross section depends on whether the WIMP in question couples to the spin of the target nucleus or whether it couples to all nucleons (spin-dependent or spin-independent, respectively). The momentum-independent cross section (σ_0) can be divided into spin-independent and spin-dependent components. For spin-independent WIMPs [65]:

$$\sigma_{0,SI} = \frac{[Zf_P + (A-Z)f_N]^2}{f_P^2} \frac{m_{r(\mathrm{T})}^2}{m_{r(\mathrm{P})}^2} \sigma_P^{SI} \tag{2.14}$$

where Z is the atomic number of the target nucleus, A is the atomic mass of the target nucleus, $m_{r(\mathrm{T})}$ and $m_{r(\mathrm{P})}$ are the reduced mass of the dark matter particle with the target nucleus and a single proton, respectively, and σ_P^{SI} is the DM-proton cross section (target-independent (and spin-independent) cross section, used to compare results from different experiments to each other and to theory). f_N and f_P are the couplings of dark matter to neutrons and protons, respectively, and can be calculated from quark couplings to dark matter according to the quark content of the universe. In many theorized treatements, $f_N \approx f_P$, yielding a simplified momentum-independent cross section [101]:

$$\sigma_{0,SI} = \sigma_P^{SI} \frac{m_{r(\mathrm{T})}^2}{m_{r(\mathrm{P})}^2} A^2 \tag{2.15}$$

Equation 2.15 is proportional to the atomic mass squared, thus more massive nuclei are preferable for the detection of spin-independent WIMPs. In contrast, spin dependent interactions only occur with nuclei that have a net spin [101]. In the case

of argon, which is used in the DEAP experiments, the even number of protons and neutrons means that DEAP is not sensitive to spin dependent interactions.

2.3.5 Detector Response

Thus far, the discussed corrections apply to an ideal detector with 100% detection efficiency, and a target consisting of one element. Of course, detector characteristics must be taken into account in order to interpret the data. Some considerations are discussed briefly below.

Often, the recoil signal does not contain the total energy deposited by an incoming particle. This is due to a quenching of the signal, often caused by the presence of impurities or other processes (discussed in Chapter 3). This means that observed recoil energies are less than their true values by some quenching factor, determined through calibration measurements. One also expects a drop in single efficiency at low nuclear recoil energies. This is because the energy transferred to the target nuclei may not be large enough to cause excitation, thus resulting in an absent signal. The effects of energy resolution and detector threshold are also important when interpreting the detector signal. A finite energy resolution has the practical result of smearing equal energy events, so that the measured values are spread about their true values. This effect is especially important when discriminating background and recoil signals, particularly in cases where the separation is not wide. Additionally, every detector has energy threshold, which corresponds to the lowest energies that the detector can reliably measure. This threshold is usually set above the energy of the main background signals.

Excluding detector response effects, together equations 2.10, 2.11, and 2.15 provide

the necessary corrections for the observed differential energy rate (equation 2.4) in the case of spin-independent interactions.

2.4 Expected Dark Matter Signatures

The usual method of identifying dark matter candidate interactions is to reject all known interactions and look at the remaining events. These events should have specific characteristics. They must be uniformly distributed throughout the detector due to the expectation that the local dark matter density is homogeneous. WIMP interactions should also be single-site events, while events due to cosmic rays, for instance, can interact multiple times in the detector. Dark matter detectors therefore use an "anti-coincidence veto system", which rejects events that occur within nanoseconds of each other [49].

Additionally, one could also look for very specific dark matter signatures. These expected signatures are based on the movement of our earth through the dark matter halo of our galaxy. Our solar system rotates around the galactic centre at 220 km/s, while our Earth travels around the sun at 29.8 km/s (for an in-depth discussion see [47] and references therein). This creates an annual modulation in the expected WIMP rate due to the yearly movement of the Earth around the Sun, i.e.: the effective speed of the detector in comparison to the halo changes as the Earth travels around the Sun. This change creates a sinusoidal modulation of the event rate with a period of one year. The event rate is at a maximum in June, when the Earth is moving with the rotation of our solar system, and at a minimum in December, when the Earth is moving against the rotation of our solar system (refer to Figure 2.4.1) [107].

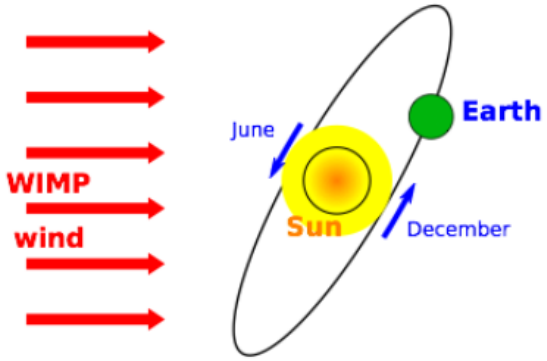

Figure 2.4.1: Diagram demonstrating how the expected dark matter rate changes with time of year [47].

The WIMP event rate also has a diurnal directional modulation due to the rotation of the Earth about its own axis. Because the Earth is tilted with respect to the galactic plane, the effective velocity of the "WIMP wind" (the dark matter halo moving with respect to the Earth) changes (see Figure 2.4.2). This signal is extremely hard for background events to imitate, and so can be considered a kind of "smoking gun" for the detection of dark matter. Essentially, the peak WIMP flux arrives from the direction of our solar system's motion through the galaxy (i.e.: we move towards the Cygnus constellation), which means that the recoil rate peaks in the opposite direction of our motion. If we assume that the WIMP distribution is smooth, this peak varies in direction during a sidereal day due to the rotation of the Earth. However, measuring this modulation presents a very difficult experimental challenge due to the extremely low energies of these interactions. Particularly in the case of directional measurements, the current technique involves detectors which must have very low densities and are difficult to scale to large sizes [3].

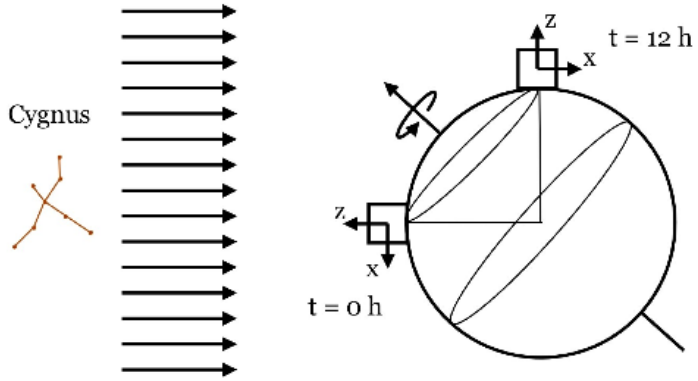

Figure 2.4.2: The effect of the rotation of the earth about its axis causes the direction of the WIMP wind to modulate diurnally [3]. At $t = 0$ h the peak direction is $-\hat{z}$, while at $t = 12$ h the peak direction is $\hat{x}$.

2.5 Experimental Considerations

Current dark matter detection experiments are pushing towards sensitivities which reach a WIMP-nucleon scattering cross section of 10^{-46} cm^2. Detectors respond to different particles in a variety of ways, and experiments typically exploit one or some combination of ionization, scintillation, and/or heat signals for particle identification (refer to Figure 2.5.1).

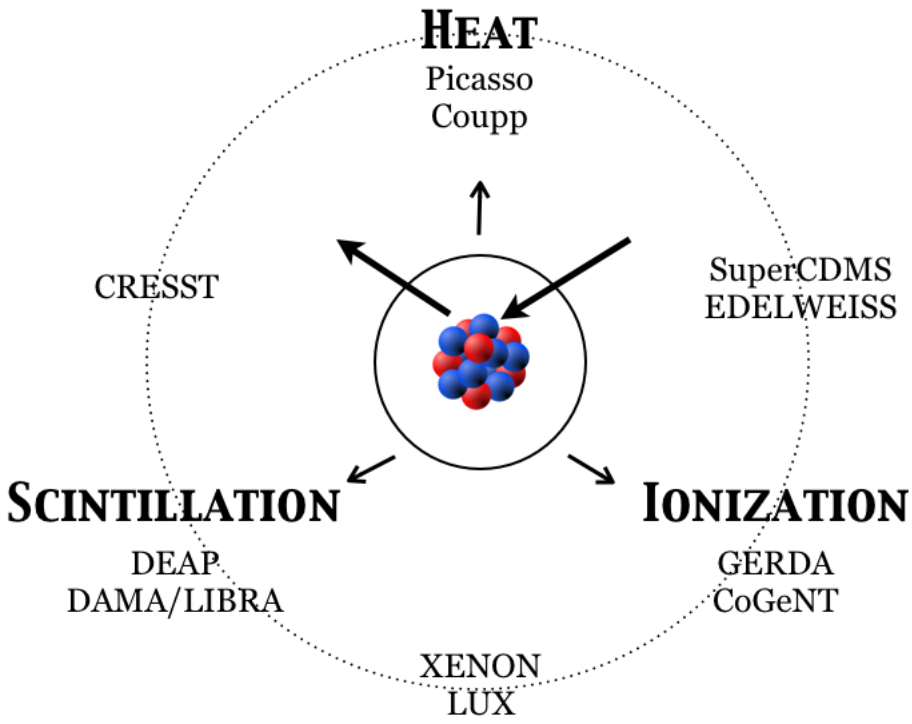

Figure 2.5.1: Dark Matter experiments make use of scintillation, ionization, and heat deposition signals. Most experiments exploit signals from more than one of these categories for particle identification. Some examples are given here.

The variation in detector response occurs due to the different ways in which particles interact with target atoms. Because WIMPs can interact with the nucleus of detector atoms due to their lack of charge, minimum ionizing particles like electrons, or photons are expected to interact differently in the detector. This is because these particles interact primarily with the electron shell rather than the nucleus (Figure 2.5.2). For a given kinetic energy, a recoiling nucleus will typically travel a smaller distance in comparison to a recoiling electron, resulting in a larger locally-deposited energy density for the nuclear recoil [97]. This allows for the identification of recoil-like and electron-like events. Suppression of beta and gamma events can be accomplished

using a variety of techniques, which are often based on differences in ionization density, scintillation light, or phonon signals. Usually detectors use more than one of scintillation, ionization, or heat (phonons in a crystal lattice) to discriminate between interactions [107].

Of course, some background events produce nuclear rather than electronic recoils (for example, incoming neutrons), effectively evading any discrimination techniques developed for electronic recoils. The main difference between WIMPs and neutrons is in their interaction cross-sections; WIMPs interact very rarely with the detector while neutrons interact very often. If an experiment is quite large, neutrons should in fact interact more than once within the detector volume [107]. Another technique for identifying neutron events is to separately measure the neutron rate in the detector components and in the areas surrounding the detector. Together these values represent the expected neutron flux, usually from uranium and thorium daughter interactions. A large experimental effort is put in to every new experiment to construct detectors from ultra low background materials in order to avoid neutron events, and effectively eliminate this neutron flux [107].

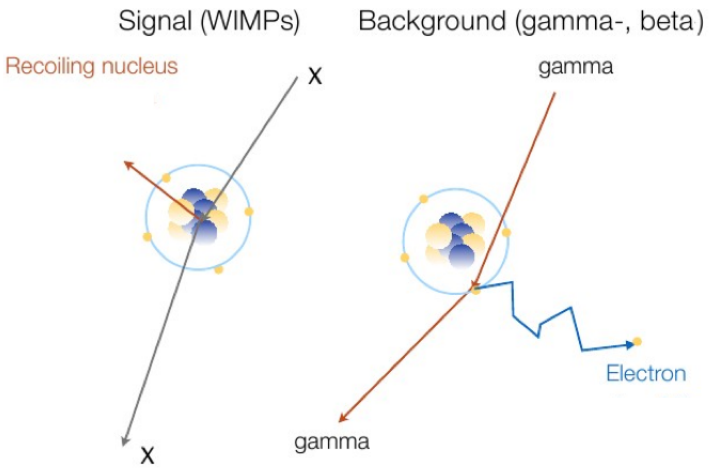

Figure 2.5.2: Left: An event which produces a recoiling nucleus is known as a "nuclear recoil event" or "nuclear recoil" (e.g.: WIMPs produce recoiling nuclei). **Right**: Events which produce an electron as a recoil are known as "electronic recoil events" or "electronic recoils" (e.g.: beta or gamma particles interact primarily with the electron shell of the target atom). Figure from [102].

Additionally, experiments control for the muon flux, which can cause neutron interactions in the detector via muon spallation, by placing dark matter experiments deep underground in order to halt the muons before they reach the detector. Energetic neutrons are created through the interactions of cosmic ray muons with an experiment's surroundings, which is why a large overburden of rock is necessary for shielding these experiments [97]. Depths of different laboratories are often quoted in "meters water equivalent (m.w.e)" for comparison purposes, since the characteristics of rock at different locations can vary. Figure 2.5.3 displays the muon flux at various particle physics laboratories.

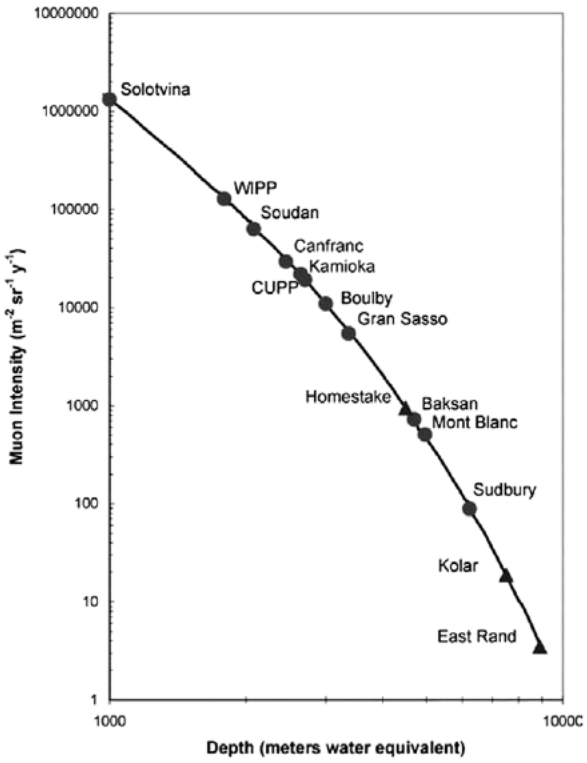

Figure 2.5.3: Vertical muon flux for underground laboratories as a function of depth. The circles are current facilities, while the triangles are closed [48].

The current best limits for dark matter detection are from the XENON and CDMS experiments. The DAMA and DAMA/LIBRA collaborations have a controversial detection claim [13], but the mass and cross section measured by their experiment is excluded by many other detectors [47]. CoGeNT, CRESST, and recently the CDMS experiment, using silicon, find an excess signal which may be compatible with a dark matter particle [5, 1, 6].

Liquid noble gas detectors have recently become popular target masses because they have good discrimination power (using scintillation and ionization or scintillation signals), are relatively simple and easily scalable to large masses, have good self-shielding, and are easily purified. DEAP-3600 is one such experiment, and is well

positioned for leading sensitivity in direct detection (see Figure 2.5.4). Competing experiments include the XENON project, which detects both scintillation and ionization signals for particle identification, and the LUX experiment, a 350 kg liquid xenon time-projection chamber. With its relatively large size, and given the current status of construction of these experiments, DEAP anticipates having the competitive results for many years to come.

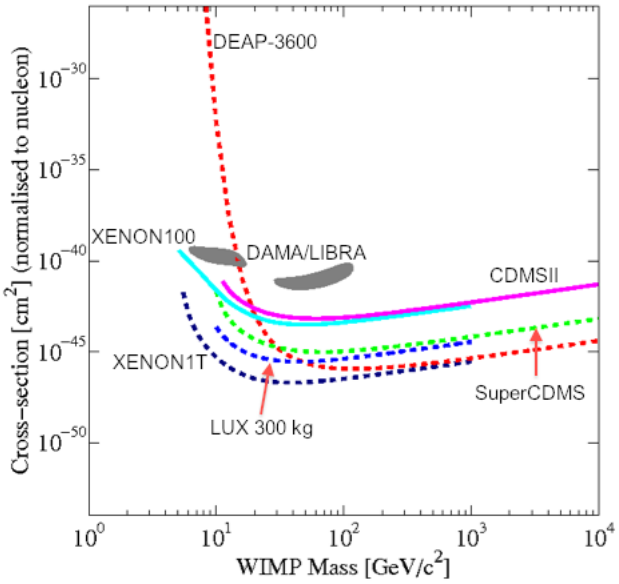

Figure 2.5.4: Sensitivities (solid lines) and projected sensitivities (dashed lines) in comparison to DEAP-3600 projected sensitivity for a 3 year background-free run (with 90% recoil acceptance and 15 keV threshold, for 8 PE/keV light yield) (red line). The LUX 300 kg projected sensitivity for 3000 kg-d, 5-30 keV, and 45% efficiency is in blue [72]. Results from the XENON-100 detector are in cyan [108]. DAMA/LIBRA results are in shaded grey [12]. The projected sensitivity of the SuperCDMS experiment is in green [100], while, for the more distant future, the projected sensitivity of the XENON1T, a ton scale dark matter experiment, is in dark blue [16]. Figure was made using [35].

Chapter 3

Dark Matter Detection with DEAP-3600

DEAP (Dark matter Experiment using Argon Pulse-shape discrimination) is a direct dark matter search experiment, located two kilometres underground in the Vale Creighton Mine near Sudbury, Ontario at the particle physics laboratory SNOLAB, which is the deepest and cleanest lab of its kind. DEAP will make use of liquid argon as the target material, which scintillates as charged particles pass through. It is a single-phase detector, making use of scintillation timing differences to distinguish between nuclear and electron recoils. The final detector, called DEAP-3600, will be sensitive to spin-independent WIMPs with a WIMP-nucleon cross-section of 10^{-46} cm^2. This is an increase in sensitivity of a factor of 100 over current best published results of other dark matter experiments. DEAP-1, a prototype detector used for research and development into direct detection techniques with liquid argon, was in operation from 2007 to 2012. DEAP-1 demonstrated the feasibility of performing a

dark matter experiment with single phase liquid argon, and provided valuable information on background reduction techniques for DEAP-3600. This chapter will first discuss liquid argon dark matter detection, and will then provide an overview on the DEAP-1 and DEAP-3600 iterations of the DEAP experiment.

3.1 Liquid Argon as a Target Material in Dark Matter Detectors

All direct dark matter detection experiments work under the same general principle. A sensitive detector is constructed, based around a target material, and is usually placed deep underground for shielding against cosmic rays. As dark matter particles pass through the detector, they deposit kinetic energy into the detector material through elastic collisions, and it is this kinetic energy which is then measured and analyzed. In DEAP-3600, liquid argon is used as both an absorber and detection medium for WIMP interactions. These interactions are measured using scintillation light produced through the elastic scattering of liquid argon nuclei from collisions with dark matter particles (Figure 3.1.1). Unlike many other detectors which use liquid noble gases as the detector medium, DEAP-3600 has a single phase design, which means that it relies on scintillation light alone for particle detection and identification. This results in a higher light yield when compared to double phase detectors, and thus a better discrimination between particles.

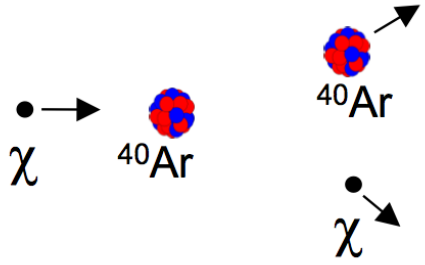

Figure 3.1.1: DEAP looks for elastic scattering between neutral dark matter particles and liquid argon nuclei.

Liquid argon is a particularly useful substance for dark matter detection for a number of reasons:

1. It has a competitive photon scintillation yield and particle interactions do not damage or change the detector medium.
2. It is relatively simple to purify of contaminants and light absorbers.
3. Liquid argon has well-separated singlet and triplet lifetimes which allow for discrimination between nuclear recoil and electronic recoil signals based on scintillation time information alone, and so allows for the use of single phase detectors (please refer to Table 3.1) [18], [19].
4. Liquid noble detectors are scalable to large target masses. Because single phase experiments can be performed, the implementation of these detectors is further simplified since there is no need to collect ionization electrons.
5. Liquid argon is relatively inexpensive.

Table 3.1 summarizes the relevant scintillation characteristics for liquid argon in comparison to the other liquid noble gases commonly used in high sensitivity experiments.

Parameter	LAr	LNe	LXe
light yield ($\times 10^4$ photons/MeV)	4.0	1.5	4.2
I_1/I_3 (electrons)	0.3		0.3
I_1/I_3 (nuclear recoils)	3		1.6
prompt time constant τ_1 (ns)	6.7	2.2	2.2
late time constant τ_2 (μs)	1.59	2.9	0.21
peak wavelength λ (nm)	128	77	174
Rayleigh scattering length (cm)	90	60	30

Table 3.1: Relevant parameters for liquid noble WIMP detection experiments ([18] and references therein). Note the ratio of prompt to late photos (I_1/I_3) for electrons and nuclear recoils - it is these values that provide the necessary background discrimination for liquid argon.

For a competitive WIMP search, an electron recoil contamination rejection factor (ERC) of 10^{-9} is required in liquid argon, due the presence of ^{39}Ar, which beta decays at an activity of approximately 1 Bq/kg. ERC is defined as the probability of misidentifying an electronic recoil as a nuclear recoil for a given nuclear recoil acceptance. In DEAP-1, the ERC was demonstrated to be less than 6×10^{-8}, while an ERC of 10^{-10} is expected for an energy threshold of 20 keV$_{ee}$ for a 1000 kg fiducial volume detector [88].

From this, we find that a 1 ton (fiducial) liquid argon detector should push the limit for a 100 GeV WIMP down to a 10^{-46} cm^2 cross section.

Of course, many liquid noble experiments choose to use xenon as the target material rather than argon (for example, XENON100 [109] and LUX [72]). This is due to the presence of a significant radioactive background in liquid argon: ^{39}Ar, which is a cosmogenically activated isotope present in natural argon. Liquid xenon is advantageous as a target material due to a high predicted event rate, high scintillation, and high ionization yield, which combined with efficient self-shielding allow for a low

threshold. Xenon-based experiments use a combination of ionization and scintillation for particle identification, which is where argon has the advantage. Due to the large difference in the ratios of prompt to late photons for electronic versus nuclear recoils in argon-based experiments (refer to Table 3.1), particle identification can be accomplished by simply comparing the detected scintillation light. This is known as Pulse Shape Discrimination (PSD), discussed in the following section.

3.1.1 Pulse Shape Discrimination

As already mentioned, DEAP 3600 will be a single-phase detector, so pulse shape discrimination is critical for operation. Ionizing radiation passing through liquid argon will ionize and excite liquid argon atoms, which then form excited diatomic molecular states, known as excimers. These excimers have two distinct states: singlet (short-lived) and triplet (long-lived) states [78], with different characteristic lifetimes ($\tau_1 = 6.7$ ns and $\tau_3 = 1600$ ns [53], respectively). The decay of these states produces scintillation light at a peak wavelength of $\lambda = 128$ nm [26]. This light is not energetic enough to re-excite another argon atom, which is why argon is transparent to its own scintillation.

The fraction of singlet (early light) versus triplet (late light) states produced in liquid argon is dependent on the type of penetrating particle. The more energy a particle dissipates per unit track length (i.e.: the higher the linear energy transfer LET), the more singlet excimers are produced. Nuclear recoil events then preferentially excite argon excimer singlet states, while electronic events from gammas and electrons produce more triplet states. This is because, due to their low LET, recombination is a slow process. The excimers produced therefore have more time to

transition to triplet states. The proportion of "early" and "late" scintillation light indicates the proportion of singlet or triplet states produced. Because of the large difference in decay times, the relative fraction of light produced early and late in the pulse allows us to estimate the fraction of singlet and triplet states formed. This in turn is representative of the LET of a particle, and therefore allows us to identify the event.

In DEAP-3600, we characterize the production of singlet vs. triplet states using a quantity known as the Prompt Fraction, or Fprompt. Fprompt is defined as the ratio between the amount of light collected in the prompt portion of an event (the first 150 ns) and the light collected over the entire pulse. Electronic recoil events have an Fprompt of about 0.3, while nuclear recoil interactions have an Fprompt around 0.7 [19]. The mean and spread of these Fprompt distributions have been determined using a tagged ^{22}Na source and an Am-Be neutron source (see Figure 3.1.2) in the DEAP-1 prototype detector [19].

3.1.2 Photon Yield

Because the energy gap between argon excimer states and the ground state are too large for non-radiative transitions to occur, one would naively expect to detect one photon for every excited dimer produced by incoming radiation. However, in practice argon scintillation light can be quenched in a variety of ways [39], [54]:

1. **Biexcitonic Quenching**: For particles with high linear energy transfer (LET), a large concentration of excimers are produced in a very small space, so there is a high probability that two will collide, producing an argon atom, argon ion, and an electron. The ion and electron will then recombine and emit a photon,

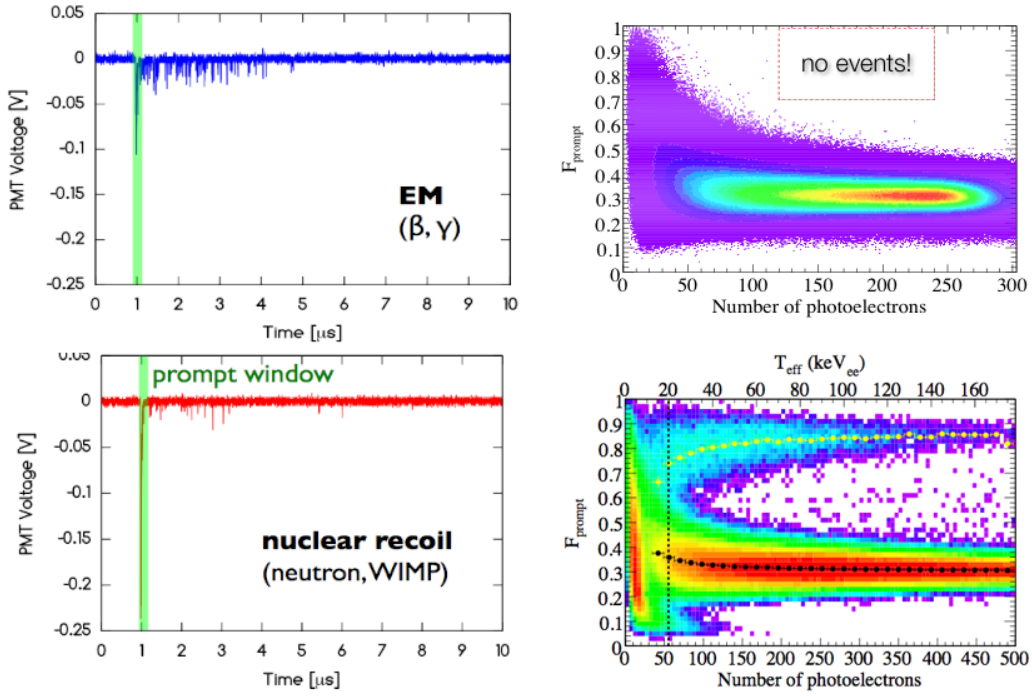

Figure 3.1.2: Upper Left: An example of a background beta or gamma event, where the prompt light window is shaded in green. **Lower Left:** An example of a nuclear recoil event. More light is emitted in the prompt window, while less light is emitted in the rest of the pulse when compared to the electronic recoil event. **Upper Right:** Triple-coincidence gamma ray events in DEAP-1 using a ^{22}Na source from the 2007 surface run [19]. The region between 120 and 240 photoelectrons (PE), where Fprompt>0.7, does not contain any events. **Lower Right:** Separation between neutron and gamma ray events from an Am-Be calibration source in DEAP-1, from the same run as the upper right plot [19]. The upper (dotted yellow) band is due to neutron-induced nuclear recoils, while the lower (dotted black, horizontal) band is from gamma-induced electronic recoils.

essentially producing one photon for two excimers.

2. **Escaping Electrons**: For low LET particles, only a few atoms are ionized and if the electrons become thermalized then they will not recombine in the acquisition window of the experiment and so no photon will be detected.

3. **Charge Carrier Trapping**: This effect is independent of LET, and is due to the presence of electronegative impurities present in the detector medium (e.g.: oxygen). After ionization, electrons are captured by electronegative impurities, preventing recombination.

4. **Electron energy transfer to impurity atoms or molecules**: The presence of impurities such as nitrogen or water, which relax non-radiatively, can cause considerable quenching. This happens when excitation energy is transferred from argon excimers to non-scintillating atoms or molecules.

The methods through which scintillation light is quenched have an effect on the implementation of experiments. In the case of DEAP-3600, this means that the liquid argon must be very pure to avoid items 3 and 4. Additionally, due to items 1 and 2, energy calibration for different types of radiation are not the same. Gamma sources are typically used for detector calibration, where the energy scale is quoted as "electron equivalent energy" (keVee). A quenching factor (0.5 for alphas [38] and 0.25 for nuclear recoils [50] in liquid argon) relates the energy calibration of gammas to the calibration of other types of particles. Where the energy quoted is calibrated for nuclear recoils, units of keVr are used.

3.2 DEAP-1

DEAP-1 was a prototype liquid argon experiment, operational at SNOLAB from 2007 to 2012, for the purpose of R&D for the larger DEAP-3600 experiment. DEAP-1 consisted of 7.6 kg of liquid argon contained in a $11'' \times 5.5''$, $1/4''$ thick acrylic sleeve. The inner surface was coated in 1-3 μm layer of wavelength shifter, 1,1,4,4-tetraphenyl-1,3-butadiene (TPB). This layer transformed the emitted liquid argon scintillation light from the UV to the visible spectrum for detection by two photomultiplier tubes (PMTs) located on either side of the detector. The acrylic chamber was kept inside a stainless steel vessel with two glass windows on either end. The PMTs were coupled to the windows using acrylic light guides, which provided both shielding and thermal insulation, allowing the PMTs to be operated at room temperature, where they have better efficiency. The detector was surrounded by water shielding to block background neutrons from entering the detector bulk. Please refer to Figure 3.2.1 for a schematic of the detector. DEAP-1 was used as a means of developing liquid argon detection techniques and background reduction methods, as well as studying mechanical and fabrication issues for DEAP-3600.

The DEAP-1 prototype detectors underwent several iterations as improvements were introduced due to increased understanding of background processes with the operation of these prototypes. The changes were as follows, paying special attention to issues which are relevant to the work described in this thesis [88]:

1. **Version 0**: The first DEAP-1 prototype took data on surface at Queen's University from November 2006 to October 2007. The acrylic sleeve was sanded by hand using P150-grit aluminum oxide paper inside a glove box under nitrogen

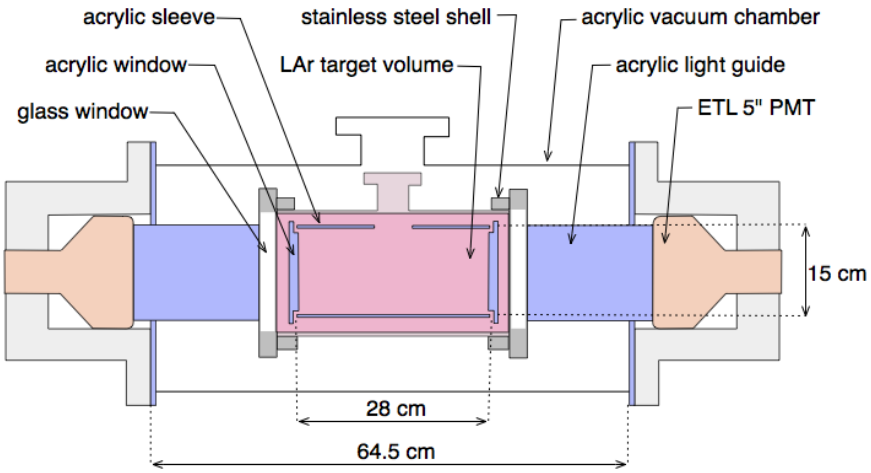

Figure 3.2.1: Schematic of the DEAP-1 detector.

atmosphere. TPB was evaporated onto the inner surface of the acrylic chamber, and the outside of the detector was painted with BC-630 (TiO_2) reflective paint. Two 5″ ETL 9390B flat-face PMTs observed the scintillation light, and data was read out using a LeCroy WavePro7100 digitizing oscilloscope.

2. **Version 1**: The detector was moved underground (6000 m.w.e) to SNOLAB and operated from December 2007 to December 2008. Before sanding, several different sandpaper options were assayed for radon and the cleanest was selected. Instead of reflective paint, which had a high radon content, a PTFE reflector was wrapped around the acrylic sleeve.

3. **Version 2**: This version of DEAP-1 took data from March to July 2009 and July to December 2009. An activated charcoal radon trap was installed and used to purify the argon before filling the detector due to the observation of an increase in alpha rate after each re-fill. This issue is also very important in DEAP 3600; emanation measurements of filtration materials are discussed in chapter 5. During the second data taking period, the waveforms were read out

using a CAEN V1720 digitizer and MIDAS data acquisition system, which will be used in DEAP-3600.

4. **Version 3**: The third iteration of the DEAP-1 prototype was in operation from March to September 2010. The acrylic sleeve was coated with a purified acrylic monomer (10 μm thick) to deal with backgrounds believed to originate from the inner surface of the acrylic chamber. The TPB was preheated before coating to evaporate contaminants. The identification of contaminants embedded in either the TPB coating or the inner acrylic surface is also a focus of this thesis, and is discussed in chapter 4. The photomultiplier tubes which will be used by DEAP-3600 were installed (Hamamatsu R5912 8$''$ high quantum efficiency (HQE) PMTs). The light guides were also replaced to make room for the new PMTs.

5. **Version 4**: This version took data November 2010 to February 2011. Because no reduction in backgrounds was seen in Version 3, it was thought that background events occurred in gaps between the acrylic chamber and the rest of the detector. New windows were machined to fit more snuggly in the acrylic sleeve, and a plug was made to fit inside the neck of the detector. The acrylic was sanded rather than coated in purified acrylic monomer since this procedure did not reduce backgrounds in the previous version of DEAP-1. Version 4 data demonstrated a very unstable light yield, thought to be due to trapped argon gas, so the windows were modified to a looser design.

6. **Version 5**: This version of DEAP-1 acquired data from June 2011 to April 2012 using new acrylic windows. No other significant changes to the detector design were introduced.

The work done on DEAP-1 has had a significant effect on the design and construction of the DEAP-3600 detector, discussed below.

3.3 DEAP-3600

DEAP-3600 is the second generation DEAP detector and will be made of 3600 kg of liquid argon contained inside an ultra-pure acrylic vessel (AV). After fiducial volume cut, there will be 1000 kg of liquid argon used for detection, with the remaining material serving as shielding. The inner AV has a radius of 85 cm, and will be coated with 1 μm of TPB to shift the scintillation UV wavelength to visible for detection. Acrylic light guides, 19 cm in diameter and 50 cm long, will collect and deliver the scintillation light to 255 Hamamatsu R5912 HQE photomultiplier tubes. The light guides are long enough to absorb most of the neutrons emitted by the PMT glass and will also serve as thermal insulation. High density layered polyethylene/insulation filler blocks will be placed in between the light guides to provide additional thermal insulation and neutron shielding. All this will be contained inside a stainless steel shell, which will provide support for the acrylic vessel. The experiment will be placed inside an 8 m diameter water tank. The water tank will be instrumented with 48 PMTs to serve as an active muon veto (through the detection of Cherenkov light), and will also shield the detector from residual neutrons and reduce the flux of external photons. The neck provides access to the acrylic vessel for tasks such as detector cleaning, TPB deposition, and calibration, as well as providing an inlet and outlet for the circulation of argon. It consists of 50 cm of acrylic bonded to the AV, while the rest is made of stainless steel. A glove box allows for the introduction of equipment into the detector without contaminating the detector volume with air. A schematic

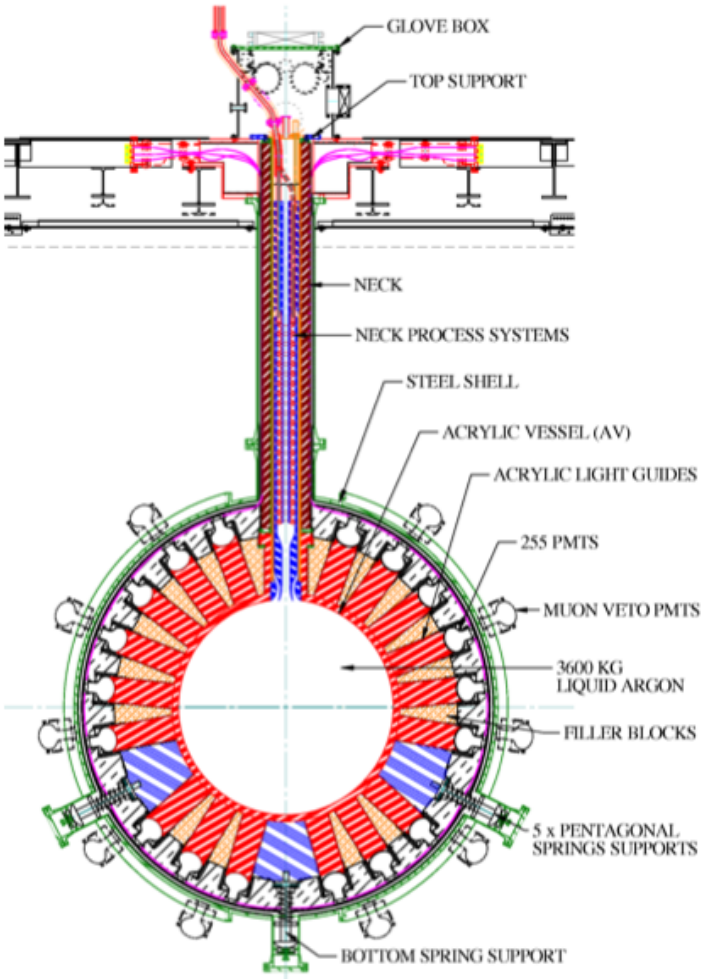

Figure 3.3.1: Schematic of the DEAP-3600 detector.

of the DEAP-3600 experiment is included (Figure 3.3.1).

DEAP-3600 is currently under construction, with all major components either completed or in progress, and it is expected to be operational in 2014.

3.3.1 Backgrounds in DEAP-3600

As with any dark matter detection program, understanding and characterization of the backgrounds is crucial to the success of the detector. Considerable effort is placed on both eliminating and characterizing background events. Recall, the target sensitivity of DEAP-3600 to a spin-independent 100GeV WIMP is 10^{-46} cm^2. This is achievable with a background-free exposure of 1,000,000 kg-days in the energy region of interest (ROI) [21]. Table 3.2 lists the background budget for DEAP-3600 for a three year run.

Background	Raw Number of Events in Energy ROI	Fiducial Number of Events in Energy ROI
Neutrons	30	< 0.2
Surface Events	150	< 0.2
^{39}Ar Beta Events	1.6×10^9	< 0.2

Table 3.2: Background budget for a DEAP-3600 three year run [21].

Surface events are largely due to radon daughters which deposit themselves onto the inner surface of the acrylic vessel and the TPB coating. Of course, trace amounts of uranium and thorium also produce surface events, requiring careful purification and selection of materials. The activity of surface contaminants presents a serious background for DEAP-3600, specifically in cases of partial energy deposition in the argon bulk. Figure 3.3.2 display the relevant decay chains for troublesome alpha surface events. Alpha emitters are situated inside the TPB or acrylic vessel (AV) due a variety of causes, and Table 3.3 lists the expected leakages from such contaminants. The corresponding target limits are also listed in both μBq/kg and ppt (parts per

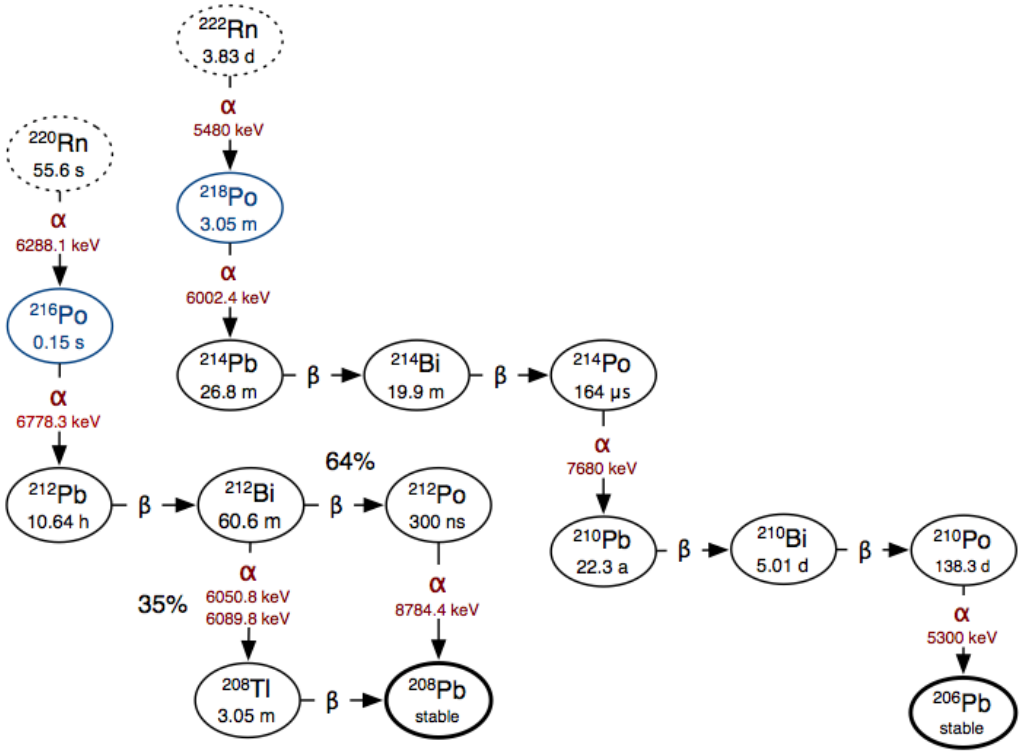

Figure 3.3.2: Decay chains of ^{220}Rn and ^{222}Rn from ^{232}Th and ^{238}U respectively. The relevant alpha decays are in red. These decays all have energies greater than 5 MeV, well outside the region of interest for dark matter detection experiments. However, should these alphas only deposit a fraction of that energy into the detector, they could imitate WIMP interactions [90]. The most critical background is the alpha decay from ^{210}Po. This is because ^{210}Pb has a half life of 22.3 years. This contamination, in the context of DEAP-3600, lasts forever. The introduction of ^{222}Rn inside the detector is therefore a much larger problem than the introduction of ^{220}Rn.

trillion).

Alpha decays which impart their full energy into the bulk argon are easily tagged due to the energetic nature of these events (several MeV), which is outside the energy ROI of the experiment. However, partial energy deposition is a much more serious issue. Figure 3.3.3 demonstrates different energy deposition possibilities from these

Location	Decay Chain	Prob. of Leakage (%)	Limit (μBq/kg)	Limit (ppt)
Inside AV	^{238}U	$0.28^{-0.02}_{+0.01}$	3.9	0.3
	^{232}Th	$0.27^{-0.03}_{+0.02}$	5.2	1.3
	^{210}Pb	$0.27^{-0.01}_{+0.02}$	31.2	1.1×10^{-8}
Inside TPB	^{238}U	$12.4^{+1.5}_{-2.2}$	2.3	0.2
	^{232}Th	$11.6^{+1.7}_{-2.2}$	3.2	0.8
	^{210}Pb	$14.7^{+1.3}_{-3.0}$	15.8	5.6×10^{-9}
On AV Surface	^{210}Pb/Po	0	NA	NA
On TPB Surface	^{210}Pb/Po	$0.2^{-0.2}_{+11.2}$	0.1 μBq/m^2	

Table 3.3: Summary of background leakage from decay chains ^{238}U, ^{232}Th, and ^{210}Pb. Estimations assume secular equilibrium. Uncertainties in column 3 are from variations in the TPB light yield by +20% (upper uncertainty) and -20% (lower uncertainty) [21].

surface events. Careful control of the exposure of the inner surface of the acrylic and TPB coating to air will help to mitigate these backgrounds. Additionally, before TPB deposition, 1 mm of acrylic will be sanded away using an automatic resurfacer to remove any radon daughter activity close to the inner surface of the acrylic vessel. Position reconstruction of events can also help to eliminate possible backgrounds. There is also the possibility of identifying alpha excitation in the TPB by looking at long time constants of the scintillation light. To this end, the characteristics of alpha-induced TPB scintillation are explored in depth in this thesis.

Contamination of the argon bulk can occur from radon emanation of process system components and the argon dewar. This is especially problematic as radon will lead to alpha decays in the argon bulk, where the radon daughters can then enter the TPB surface and lead to surface events. The purity and cleanliness of any components that will come into contact with the argon is extremely important. Hence, prior to

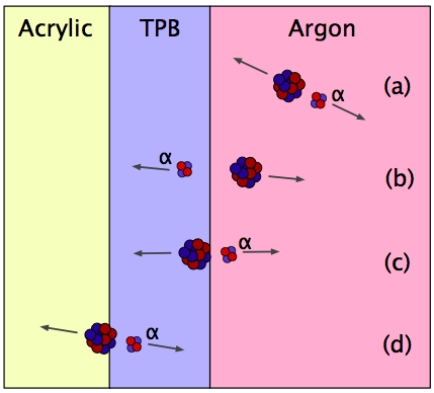

Figure 3.3.3: A schematic of different background events from acrylic and TPB contamination. (a) Decays in the argon bulk are tagged by the energy deposition from the α particle, and do not present a significant background. (b) Decays which eject a recoiling nucleus into the argon and an α particle in the TPB layer are seen as single events, and can contaminate the experimental signal. (c) Decays which eject an α particle into the argon and a recoiling nucleus into the TPB allow the α particle to impart its full energy into the liquid argon. These events are therefore expected to be outside the ROI of the experiment. (d) Decays at the TPB or acrylic region can produce a small signal from either the α energy deposited in the TPB or in the liquid argon. This can be a significant problem if not removed prior to operation [21].

filling the detector, the argon will be filtered through a "radon trap". Filtration of the argon will be accomplished using activated carbon. Of course, the carbon itself may also emanate radon. Radon emanated inside the carbon itself has a much larger probability of escaping the radon trap, and so a carbon with a very low emanation rate must be selected. The overall limit on contamination of the liquid argon through the purification system by radon emanation is 5.4 mBq, for an assumed maximum exposure time of month [21]. Therefore the target emanation rate for the radon trap carbon must be < 5 mBq.

Neutrons are a particularly problematic background for dark matter experiments, as they interact with the detector in the same way as dark matter particles are expected to. Sources of neutrons include (α,n) interactions in the acrylic, PMT

glass, steel shell, or from the laboratory surroundings (rock wall, infrastructure, etc.). Neutron radiation will be mitigated through careful control of acrylic contamination and by the use of long light guides and filler blocks to shield the inner portions of the detector. Additionally, the entire detector will be surrounded by a water tank for shielding. Neutrons can also reach the detector due to cosmic rays; spallation events from muons produce showers of neutrons. The detector is therefore placed 2 km underground, providing a 6000 m.w.e shielding against cosmic rays. There will also be an active muon veto for background identification.

The largest source of backgrounds in DEAP-3600 will be the decay of ^{39}Ar, a β-emitter with a mean lifetime of 388 years [27]. The ratio of ^{39}Ar in natural argon is $8.1 \pm 0.3 \times 10^{-16}$ [71]. Beta particles from ^{39}Ar and other electronic recoil background events will be identified using pulse shape discrimination, as discussed above.

This thesis focuses on background signals from surface events and argon contamination, specifically background events from alpha emitters passing through the TPB layer, and contaminants which enter the liquid argon from radon emanation of the carbon in the radon trap.

Chapter 4

Apha-Induced Scintillation Properties of Tetraphenyl Butadiene

The organic wavelength shifter, [1,1,4,4]-tetraphenyl-[1,3]-butadiene (TPB), is employed in the DEAP experiment to shift the liquid argon scintillation light into the visible regime for detection, and is used for similar purposes in other high-sensitivity liquid noble experiments. In spite of this, the scintillation properties of this compound have not been studied at liquid noble temperatures. In particular, alpha emitters embedded in the detector walls and within the TPB itself can imitate recoil signals. Understanding the alpha scintillation of TPB at liquid argon temperatures is crucial for understanding the background signals of the detector. Here we investigate the properties of TPB scintillation due to alpha particles at temperatures ranging from 300 K to 3.4 K. We first discuss the general properties of organic scintillation, and then summarize the experimental procedure. We provide measurements of the light

yield relative to room temperature, and measure the decay constants of the scintillation light. The results are discussed within the context of the DEAP experiment and other liquid noble detectors.

4.1 Overview of Organic Scintillation Theory

Materials are luminescent if, under excitation, they produce light. Scintillation light is caused by the excitation of a material by an ionizing particle or absorption of a photon, where the excitation energy is converted to electromagnetic radiation (usually in the ultraviolet, visible, and infrared ranges). The organic scintillation process, in simplest terms, involves the excitation of atoms or molecules, which thermally relax into the lowest excited state, and then, with the emission of light, they return to the ground state. The light produced from scintillation typically falls into two categories: fluorescence and phosphorescence. Fluorescence is the name given to the prompt light produced in the first few nanoseconds after excitation, while phosphorescence describes the scintillation light emitted after a significant time lag from the moment of absorption. Sometimes emission can occur as late as several hours later, but typically phosphorescence has a decay constant of milliseconds to seconds. Fluorescence results from the spontaneous decay of singlet excited states, while phosphorescence is the result of transfers to forbidden triplet energy states.

All organic scintillators produce luminescence through the excitation and relaxation of molecules which possess delocalized π-electron wave functions. Specifically, these scintillators employ aromatic molecules. In the case of TPB, its scintillation characteristics are determined by the chemistry and physics of its four phenyl groups (refer to Figure 4.1.1 for the molecular structure of TPB).

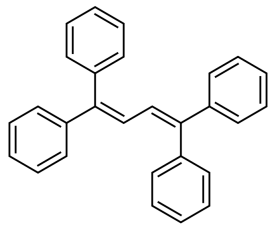

Figure 4.1.1: Molecular structure of 1,1,4,4-Tetraphenyl-1,3-Butadiene ($C_{28}H_{22}$). This organic scintillator has four phenyl (C_6H_5) groups.

Recall that σ bonds are the bonds which form in single bonds, while double bonds contain both a σ and π bond.

Aromatic molecules are unique in that the bonds holding their atoms together are neither single- nor double-bonded, but instead are bonded in some intermediate way. In the simple example of benzene (C_6H_6), the carbon atoms arrange themselves in a planar, circular structure, where each carbon-carbon bond is of equal length (implying that each bond has the same strength). Three of each carbon's outer electrons enter sp^2 hybridized states, and form σ bonds with its two neighbouring carbons and a hydrogen atom. This leaves an electron in the p_z orbital for each carbon; these p_z orbitals are perpendicular to the plane of the molecule. Rather than forming three separate π-bonds (and thus three separate double bonds) within the molecule, these p_z electrons are free to cycle about the circular arrangements of carbon atoms; the electrons are shared by all six atoms in the benzene ring. This is known as *delocalization*, and the electrons form delocalized π-bonds. Refer to, for instance, [52], for a discussion of aromatic molecules.

It is the excitation and de-excitation of these delocalized pi-electrons that cause scintillation in organic molecules. The processes in organic scintillators which result in the conversion of kinetic energy into electronic excitation energy, and subsequently

into scintillation light, are quite complicated and not completely understood. However, there are three general processes which impact the characteristics (timing and intensity) of the resultant scintillation light [15]:

1. Radiative excitation (absorption).
2. Radiative relaxation (luminescence).
3. Non-radiative relaxation.

Figure 4.1.2 depicts electronic energy level transitions which can occur in aromatic molecules. We will discuss these transitions in the context of the three processes listed above.

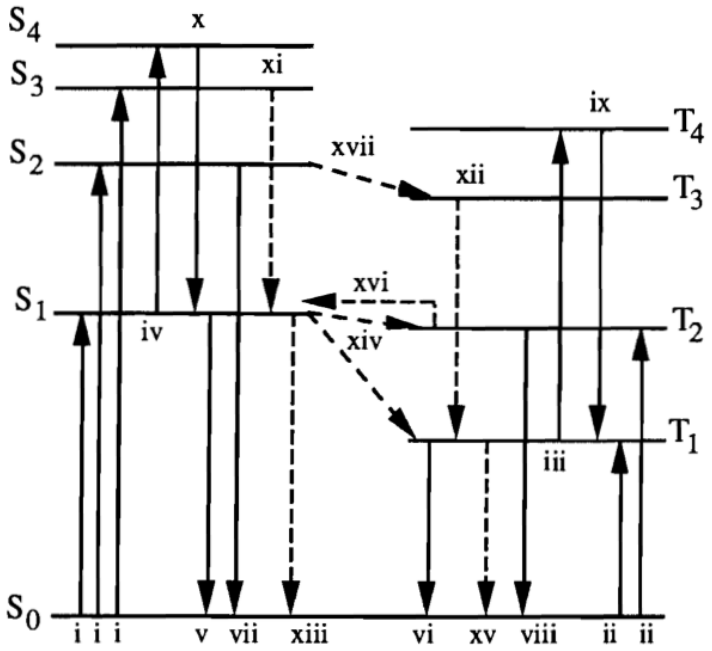

Figure 4.1.2: Energy levels and transitions which can occur in aromatic molecules. Solid lines indicate radiative transitions, while dashed lines indicate non-radiative transitions [15, 55].

4.1.1 Radiative Excitation

Excitation transitions, which correspond to the radiative excitation process, are caused by the absorption of an incident photon or the transfer of kinetic energy from ionizing radiation. These transitions include S_0 to S_1 and S_0 to $S_{p(p>1)}$(labelled (i) in Figure 4.1.2), S_1 to $S_{p(p>1)}$ (iv), T_1 to $T_{q(q>1)}$ (iii), S_0 to T_1 and S_0 to $T_{q(q>1)}$ (ii). The S_i to S_j and T_i to T_j transitions are spin-allowed. Transitions labelled (i) dominate and are responsible for the main characteristics of absorption spectra. Transitions (ii) are spin-forbidden, and are therefore very rare; they are more likely to occur due ionizing radiation rather than photon excitation.

4.1.2 Radiative Relaxation

Transitions which cause luminescence (the radiative relaxation process) are divided into two categories: fluorescence and phosphorescence. Flourescence transitions are spin-allowed and include S_1 to S_0 (v), S_p to S_0 (vii), S_p to S_1 (x), and T_q to T_1 (ix). Transitions to the ground state from energy states $S_{p(p>1)}$ are quite rare, and so fluorescence is dominated by the (v) transition. Phosphorescence occurs due to spin-forbidden transitions, and includes the T_1 to S_0 (vi) and T_q to S_0 (viii) transitions. The (vi) transition is most common, while (viii) transitions are extremely improbable.

4.1.3 Non-Radiative Relaxation

Non-radiative transition processes fall under two broad categories: internal conversion and intersystem crossing, where internal conversion describes transitions where the molecule's spin state remains the same, while intersystem crossing involves a change in the spin state. In internal conversion, the energy of electronic excited states is

expanded through vibrational modes of the molecule. The S_2 to S_1 and S_p to $S_{p\text{-}1}$ (xi), T_2 to T_1 and T_q to $T_{q\text{-}1}$ (xii), and S_1 to S_0 (xiii) transitions are internal conversions. The (xiii) transition is rare in comparison to (xi) transitions due to the larger energy gap between the ground state and first excited state. Internal conversions between the higher S energy states, however, have extremely fast time constants (on the order of picoseconds) and so are extremely efficient. Additionally, should radiative de-excitation occur between the excited S states, the light produced is easily re-absorbed by surrounding excited molecules. This is why fluorescence is dominated by the S_1 to S_0 (v) radiative transition. Conversely, non-radiative transitions which involve a change in spin (intersystem crossing) are due to spin-orbit coupling, which is an interaction between an electron's spin and its motion, causing its spin state to flip. Intersystem crossing transitions include S_1 to T_1 (xiv), T_1 to S_0 (vi), S_1 to T_q (xiv), S_p to T_q (xvii), and $T_{1,2}$ to S_1 (xvi).

In general, the triplet states must be thermally activated in order for these transitions to occur [15, 105]. Vibronic energy levels of S_1 can overlap with higher levels of triplet states, which can then directly spin-orbit couple to S_1. Therefore, intersystem crossing can occur with an activation energy equal to the energy difference between the S_1 and $T_{m\ (m>1)}$ states. For moderately-sized molecules, T_m can be only slightly higher than S_1, so S_1's vibronic states easily overlap with the triplet states at room temperature, producing a significant fraction of late light in organic scintillation signals.

Impurities (which cause quenching) and vibrational energy levels can change this simplistic picture of energy transitions.

Vibrational states are key in organic scintillation as they cause the molecules to

be transparent to their scintillation light. Electronic excitations within molecules can be accompanied by molecular vibrations. Electronic excitations occur extremely quickly (in the case of absorption of a photon, within femtoseconds), leaving the much heavier nuclei motionless during this sudden transition. Afterwards, the nuclei within the molecule reorganize themselves according to the new electronic configuration; this causes vibrations. This extra thermal energy is quickly dissipated through collisions with other molecules, and the lowest vibrational levels (S_{i0} or T_{i0}) become occupied within picoseconds. As discussed above, electrons in the higher excited states also quickly drop to the lowest excited state S_{10} through internal conversion. It is this combination of loss of vibrational energy and internal conversion to the lowest excited state that leads to the necessary red shift of the emission spectrum with respect to the absorption spectrum (the "Stoke's shift") [98].

In summary, upon excitation, the excited energy levels of individual molecules (including the vibrational levels) become populated. Almost immediately (picoseconds), the excited states vibrationally relax to the lowest excited state (S_{10}). After fluorescence (the emission of a photon), the molecule returns to its ground state (nanoseconds). The ground state in most organic scintillators is a singlet S_0 state, while S_1 states are populated upon excitation. The excited S_1 state can sometimes transition to a forbidden triplet T_1 state through spin-orbit coupling. After relaxing down to a zero-vibrational excited state, a photon is then emitted as the excited singlet or triplet states transition down to vibrational levels of the ground state. Refer to Table 4.1 for additional information on different transitions and their timescales.

Several other relaxation pathways compete with fluorescence and phosphorescence. Excited states can fall to the ground state through non-radiative decay by the

Transition	Process	Timescale (s)
S(0) to S(1) or S(n)	Absorption (Excitation)	10^{-15}
S(n) to S(1)	Internal Conversion	$10^{-14} - 10^{-10}$
S(1) to S(1)	Vibrational Relaxation	$10^{-12} - 10^{-10}$
S(1) to S(0)	Fluorescence	$10^{-9} - 10^{-7}$
S(1) to T(1)	Intersystem Crossing	$10^{-10} - 10^{-8}$
S(1) to S(0)	Non-Radiative Relaxation/Quenching	$10^{-7} - 10^{-5}$
T(1) to S(0)	Phosphorescence	$10^{-3} - 100$
T(1) to S(0)	Non-Radiative Relaxation/Quenching	$10^{-3} - 100$

Table 4.1: Summary of processes which impact organic scintillation and their respective timescales [33].

dissipation of heat, as discussed above, while collisions with surrounding molecules can transfer energy and cause quenching [33]. As detailed in Chapter 3 with regards to Argon scintillation, contaminants can absorb excitation energy and thus further quench the expected signal.

Whereas the time constants associated with individual molecular transitions are not temperature dependent, the relative intensities of the scintillation from these transitions will be influenced by temperature. This behaviour is of great interest for high sensitivity experiments which make use of the wavelength shifter tetraphenyl butadiene, and will be studied in the following sections.

4.2 The Tetraphenyl Butadiene Wavelength Shifter

TPB is an organic compound that will be used in the DEAP-3600 liquid argon experiment as a wavelength shifter. TPB is commonly used as a wavelength shifter in many different applications, including low background measurements in physics. In DEAP-3600, the acrylic shell which holds the liquid argon will be coated in a thin, 1 μm layer of TPB. Its purpose is to convert UV scintillation light from liquid argon

to a peak wavelength of 420 nm for detection using conventional PMTs (also because acrylic is not transparent to UV light). However, previous studies [89], have demonstrated that TPB does scintillate under alpha excitation, thus introducing a possible source of background due to alpha emitters (from uranium and thorium decay chains) embedded in the acrylic or the TPB itself.

Alphas in the TPB layer itself, and in the acrylic from as far as 80 μm away from the TPB coating, could enter the TPB and produce a scintillation signal [88]. The amount of energy they deposit depends on how far away their source was, at what angle they pass through the coating, and on the original energy of the emitted particle. A fraction of these events may appear in the signal region for DEAP. If they also have a similar Fprompt ratio, they could be a very dangerous source of background [88].

An extensive study of alpha-induced TPB scintillation has already been completed at room temperature [89]. Alpha-induced scintillation in TPB was found to have an Fprompt value of 0.67 $\pm$ 0.03. This TPB Fprompt is very close to the measured Fprompt of 0.8 for neutron events in DEAP-1. TPB scintillation is therefore a concern for DEAP. However, the long time constants for these events were shown to be very different, where alpha-induced scintillation of TPB produced a 275 $\pm$ 10 ns time constant for the long portion of the pulse vs. a long time constant of 1600 ns for liquid argon (see Figure 4.2.1). This provides a promising avenue for the development of a sophisticated pulse-shape discrimination technique based on the long time constants of the pulse shapes, provided this behaviour persists at the operational temperature of TPB at liquid argon temperature.

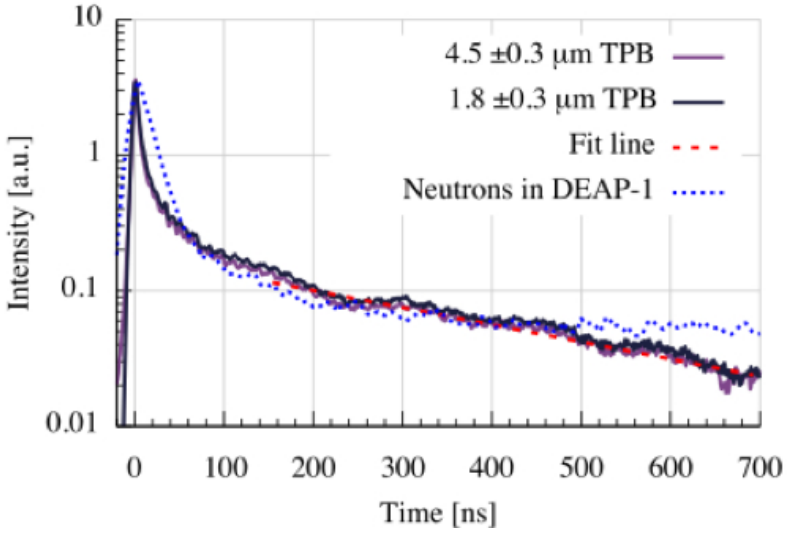

Figure 4.2.1: Neutron pulse shape from DEAP-1 compared to alpha-induced TPB scintillation pulse shapes at room temperature. Fprompt values are similar, but the long time constants are quite different (1600 ns vs. 275 ± 10 ns) [89]. The short time constants also appear quite different, however, the error on the short time constant in this measurement is quite large. Note that TPB thickness does not affect the shape of the curve.

However, scintillation properties can change dramatically with temperature (for instance [7]), and to our knowledge no studies have been conducted on TPB alpha-excitation response below room temperature. Therefore, an investigation of alpha-induced TPB scintillation was conducted at temperatures ranging from 300 K to 3.4 K, with special attention given to liquid noble gas temperatures.

4.3 The TPB Sample

A TPB sample was prepared using the evaporation technique from [89] (discussed in detail in [88]). We briefly review the process here.

Prior to evaporation, the substrate was carefully cleaned using a six step process. First, the substrate was washed with tap water and soap, then wiped with

isopropanol, and then wiped again with a 20% ethanol and 80% ultra pure water mixture. Afterwards, the quartz face was wiped with aluminum foil, rinsed with ultra pure water, and blown dry with a noble gas. These steps helped to ensure a smooth, even coating by eliminating accumulated surface charge and drying marks.

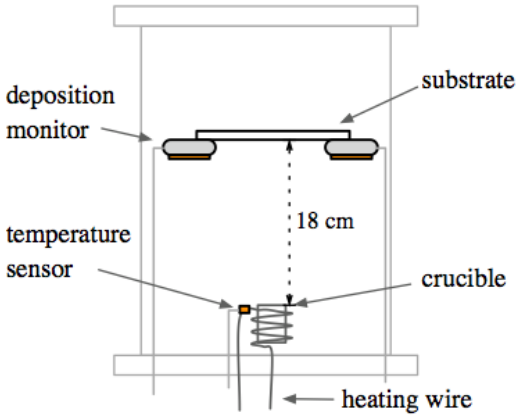

Figure 4.3.1: Schematic of the TPB evaporation system [89].

The evaporation procedure itself was developed specifically for producing evenly-coated TPB samples of known thickness (refer to Figure 4.3.1). TPB powder of crystalline scintillation quality, from American Chemicals LTD, was placed inside a quartz glass crucible (1 cm height $\times$ 1 cm diameter) located at the bottom of a cylindrical vacuum chamber. The crucible was wrapped in a heating wire, which heats the TPB to a target temperature of approximately 200° C. The temperature of the crucible was monitored by an OMEGA resistance temperature sensor clipped to the heating wire near the crucible. The thermometer readout was coupled to the heating power supply in order to maintain a constant temperature. The substrate was held on a rack, centred above the crucible so that the TPB could coat the substrate as it

evaporated. Two quartz crystal deposition monitors were placed on either side of the substrate to monitor the thickness of the TPB film.

The sample used for this experiment was a quartz (99.995% silicon dioxide from McMaster-Carr) substrate with a size of 7x10 mm^2 and a thickness of 1/16″. The substrate was covered by a 10 μm coating of TPB on one 7x10 mm^2 side (see Figure 4.3.2).

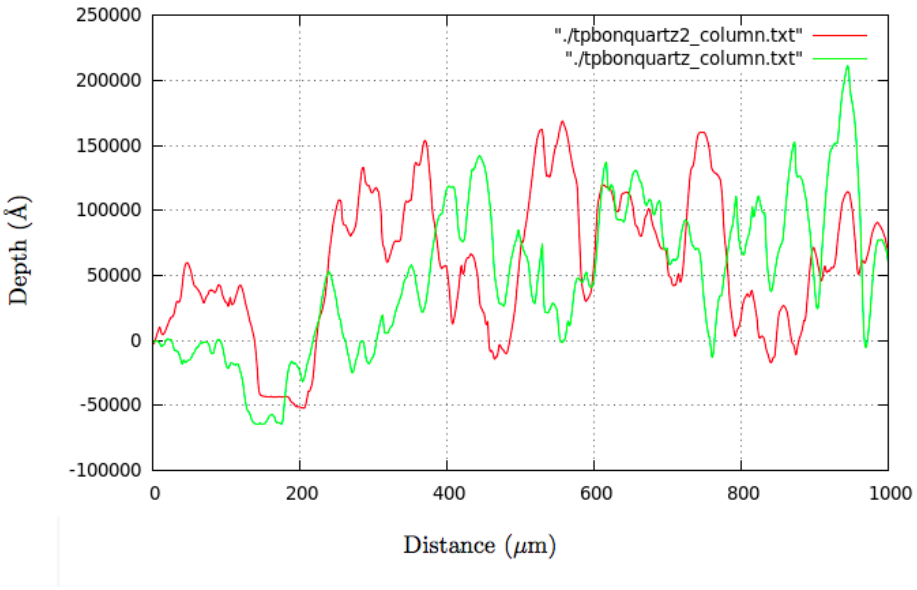

Figure 4.3.2: Measurement of TPB thickness using a Dektak 8M Stylus profile meter. The dip between 150 μm and 200 μm is a scratch, done on purpose to the TPB coating to provide a baseline. The two data sets are from separate scans conducted at different locations on the TPB sample. We can see that the TPB coating is unusually rough, however on average it is 10 μm thick ($\pm$5 μm). Coatings made with the process described here typically showed a variation in thickness of 1 μm, rather than the variation of $\approx 10\mu$m we see here.

4.4 Experimental Method

We made use of an optical cryostat with compact geometry at Queen's University [110, 37]. The sample was centred between two PMTs (Hamamatsu R6095P), which were kept at room temperature outside the cryostat (attached to Suprasil windows). We used an Am^{241} alpha source, collimated down to about 3 Hz of effective event rate with a copper aperture. Please see Figures 4.4.1 and 4.4.2.

The signal from the PMTs was fed, through a Fan In/Out unit, to a PXI digitizer module from National Instruments and registered when in coincidence. Both channels were split at the Fan In/Out unit and half the signal was sent to a discriminator (with 10 mV threshold). Logical signals from the discriminator were used to generate the coincidence tag (if within the 30 ns long coincidence window). The full length of the signal acquisition window was 200 μs (including a 20 μs pre-trigger window), with a 1 ns sampling rate.

A LabVIEW online analysis program was used for initial data reduction, which included: assigning unique IDs to all events, threshold based identification of individual photons (or inseparable groups of photons) within an event and calculating their charge integrals (above the baseline). Then, finally, a list of events with IDs, total charge, and an array of individual photon arrival times and charges were recorded to an ASCII file to be used for further offline analysis.

Several runs were undertaken with this setup. Firstly, measurements of the quartz coated in TPB sample were irradiated with the AmBe source at different temperatures between 300 K and 3.4 K. After a full temperature sweep, an additional measurement was done at room temperature to verify that no changes occurred with the sample. Finally, a measurement using an identical quartz window with no TPB coating was

done to ensure that the substrate itself was not affecting our data. Please see Appendix A for relevant plots.

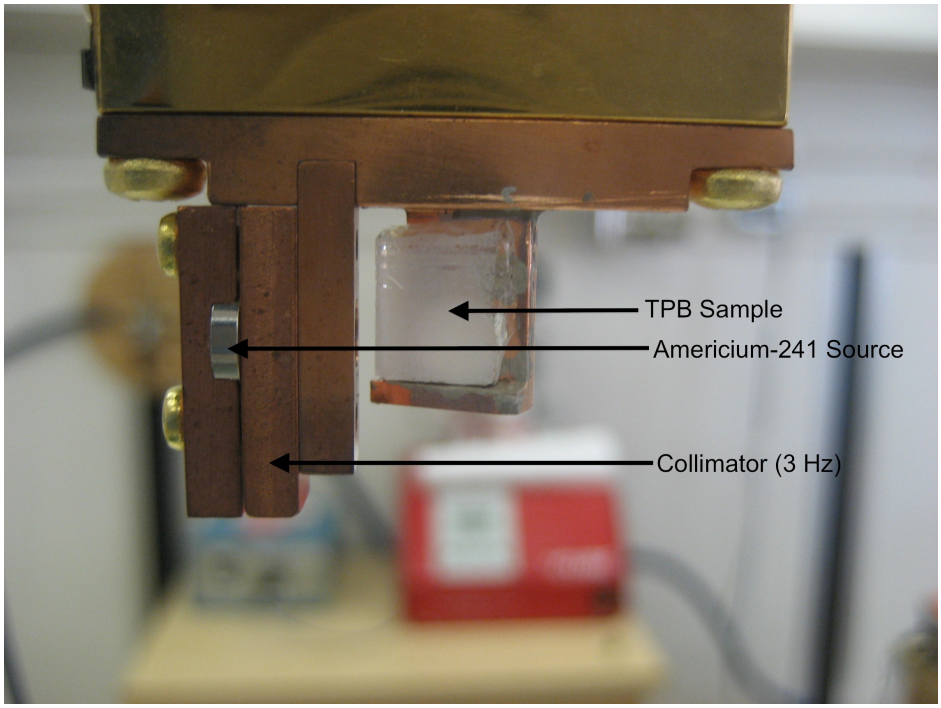

Figure 4.4.1: Mounted sample with Americium source and 3 Hz collimator installed. Sample is set such that the alphas will hit the smoothest portion of the TPB coating. Edges are ragged due to the size requirements of the mount - the quartz sample had to be cut from 1 inch in diameter to a 7x10 mm^2 rectangle.

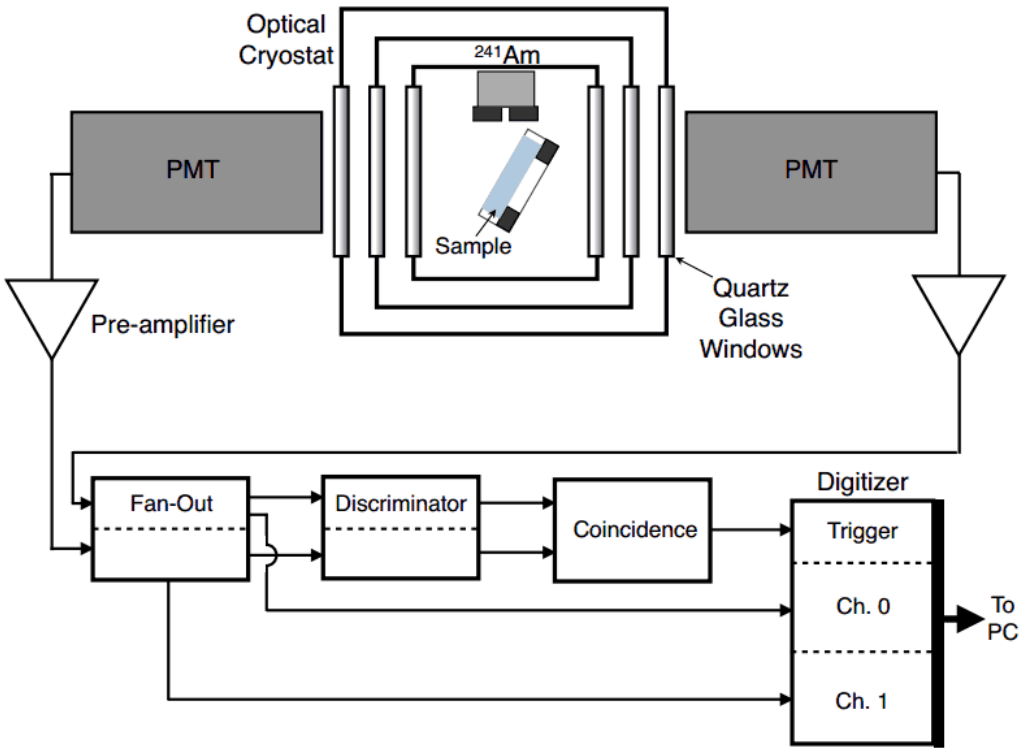

Figure 4.4.2: A schematic of the experimental set up [79]. The sample is placed between two PMTs, which face each other and are 1.5 cm away from the sample. The outer windows on the vacuum can are separated by around 3.0 cm. In this figure, the left PMT (PMT0) faces the coated side of the sample, while the right PMT faces the blank side. The angle of incidence of the alphas from the collimated ^{241}Am source is 30 degrees. Events are triggered if both PMTs see a signal within a 30 ns coincidence window.

4.5 Analysis and Results

4.5.1 Data Reduction

This discussion references [66] extensively.

The Multiple Photon Counting Coincidence technique (MPCC) is used to simultaneously measure the light yield and decay time constants of a scintillator. The

process involves the recording of a sequence of pulses caused by a scintillation event using photomultiplier tubes. Photons reaching the photocathode of the PMTs, liberate photoelectrons, which then pass through an amplification stage to convert the electron signal into a measurable charge. Each PMT pulse corresponds to an individual photon (or groups of photos) reaching the PMT photocathode, thus the distribution of photon arrival times provides information on the decay characteristics of the scintillator, while the total charge per event is proportional to the light yield (photoelectrons per unit of deposited energy). By recording a large number of events, the MPCC technique allows for the determination of the decay constants and relative light yield of a scintillator simultaneously.

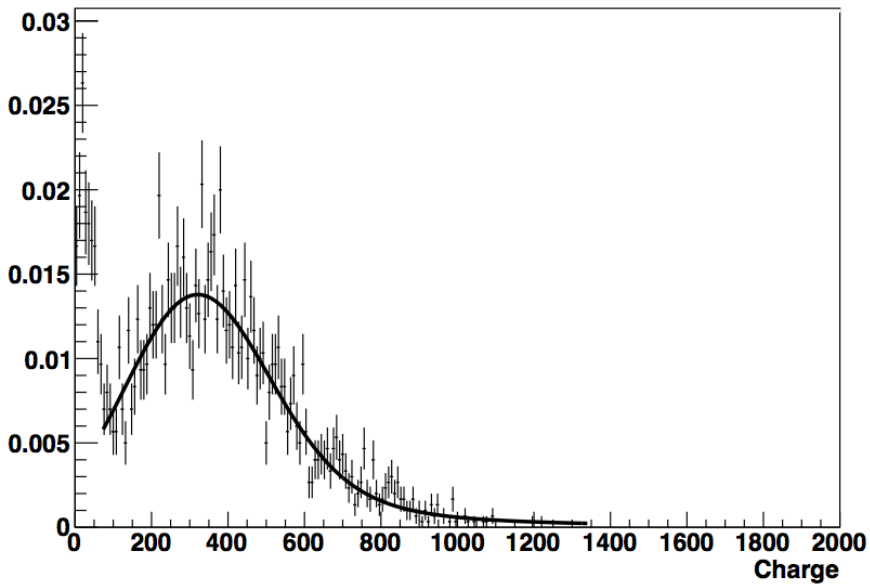

Figure 4.5.1: Detected light distribution at 87 K (for one PMT) prior to the implementation of data-cleaning cuts.

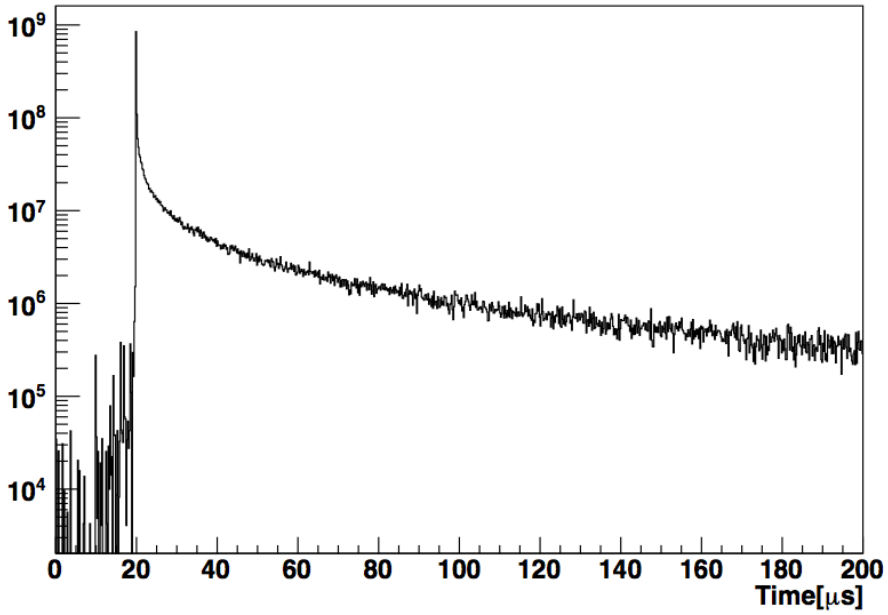

Figure 4.5.2: Pulse Shape at 87 K prior to the implementation of data-cleaning cuts.

Because this measurement technique records multiple events, pile-up (when several events are recorded as a single event), and the leaking of event tails into subsequent measurements, must be removed from the data (refer to Figures 4.5.1 and 4.5.2 to view data prior to the performance of cuts). For instance, if pulses with anomalous early times (occurring in the pre-trigger, and often due to photon pulses from previous scintillation events) are not identified, they will introduce noticeable errors in the decay constants since the constants are determined with respect to the first photon arrival time. Events with an early first photon cause an overestimation of decay time constants.

Figure 4.5.3 depicts a typical first photon arrival time distribution (in this particular case, the data are at 87 K). Notice the majority of first photon arrival times are between 19.95 μs and 20.00 μs, while some pulses have leaked into the pre-trigger

window (especially for the stronger PMT at channel 0). The time interval during which the majority of events begin is defined by the hardware trigger, while earlier events are due to remaining pulses of previous events being recorded with the actual event that produced the current trigger. These are eliminated by rejecting events that have a first photon arrival time not within the dominant section of the distribution. Specifically, events which do not fall between 19.978 μs and 19.985 μs (as recorded by PMT1, the trigger PMT) are rejected.

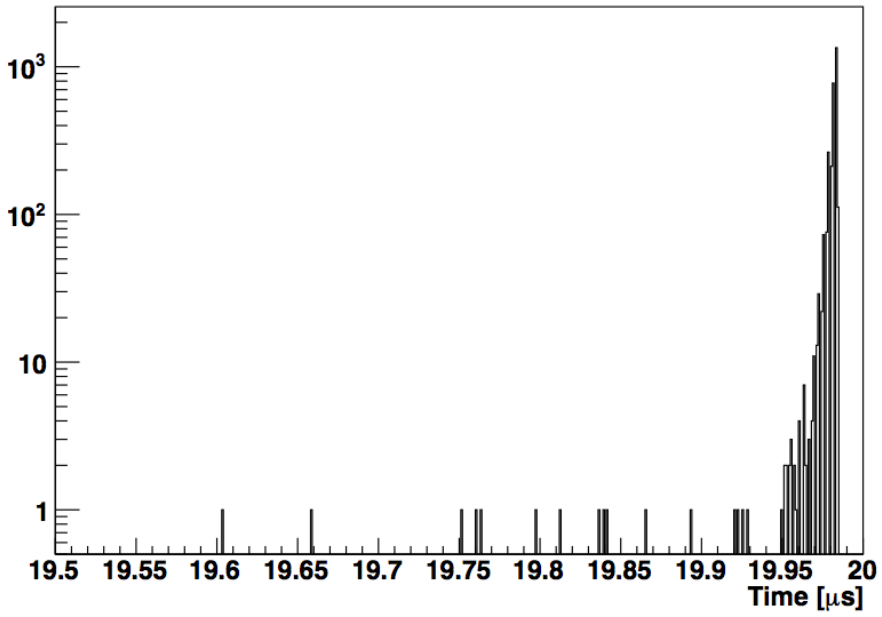

Figure 4.5.3: The first photon arrival time distributions at 87 K.

In addition to cutting on the first photon arrival time of PMT1, the difference in the first photon arrival times between both channels was investigated (Figure 4.5.4).

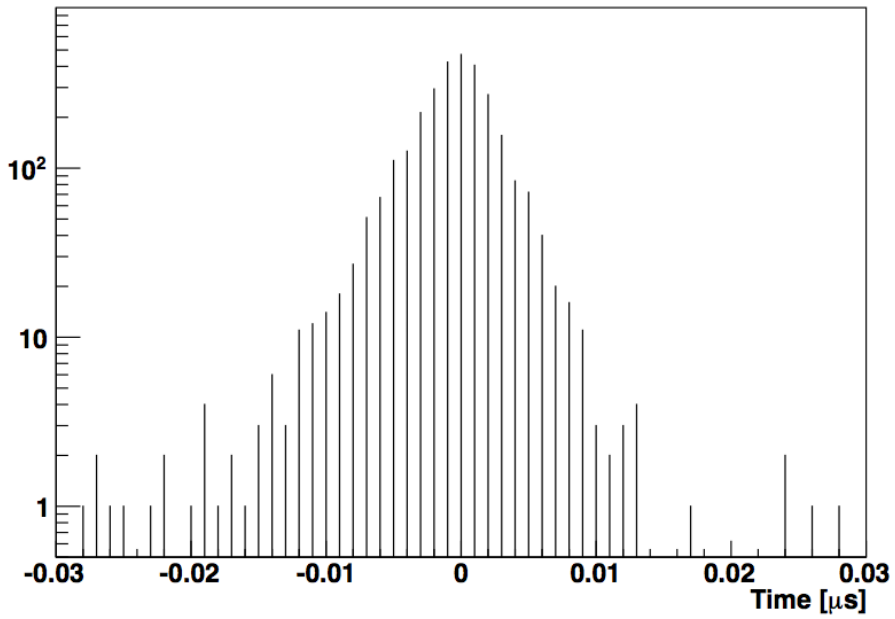

Figure 4.5.4: Difference in first photon arrival times between the two PMTs at 87 K.

The coincidence time was 30 ns, however the timing was set such that the signals from each PMT should arrive at the same time. Events which fall close to $|t_{0,\mathrm{Ch0}} - t_{0,\mathrm{Ch1}}| = 30$ ns have some chance of being false triggers. To that end, all events with a difference in the first photon arrival times greater than 5 ns were rejected.

One last data cleaning cut was applied in the offline analysis, which involved the mean event arrival time (charge-weighted, averaged over all photons) for PMT0 (refer to Figure 4.5.5. The basic idea is that events which contain pile-up are likely to have a different average time, especially when weighted by charge, in comparison to events which are clean, due to the interjection of anomalous pulses into the event. The mean event arrival time for PMT0 was kept, on average, between 30 μs and 50 μs. These limits were, of course, adjusted according to specific characteristics of the mean arrival time distributions for various temperatures.

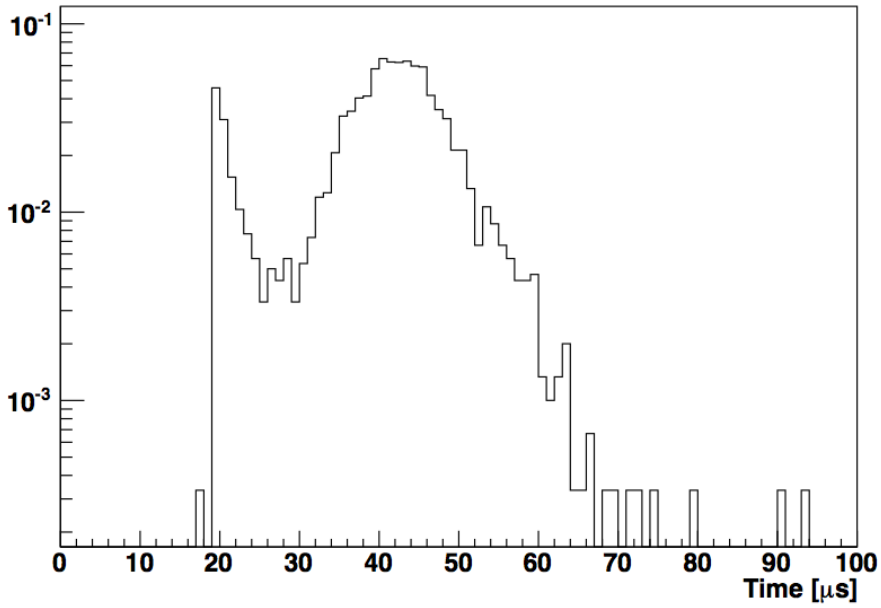

Figure 4.5.5: The charged weighted mean event arrival time for channel 0, averaged over all photons at 87 K.

Figures 4.5.6 and 4.5.7 depict the resulting light yield and pulse shape distributions after the cuts were applied. Clearly, spurious events (seen as a peak near zero in Figure 4.5.1, and as events in the pre-trigger for Figure 4.5.2) have been successfully removed.

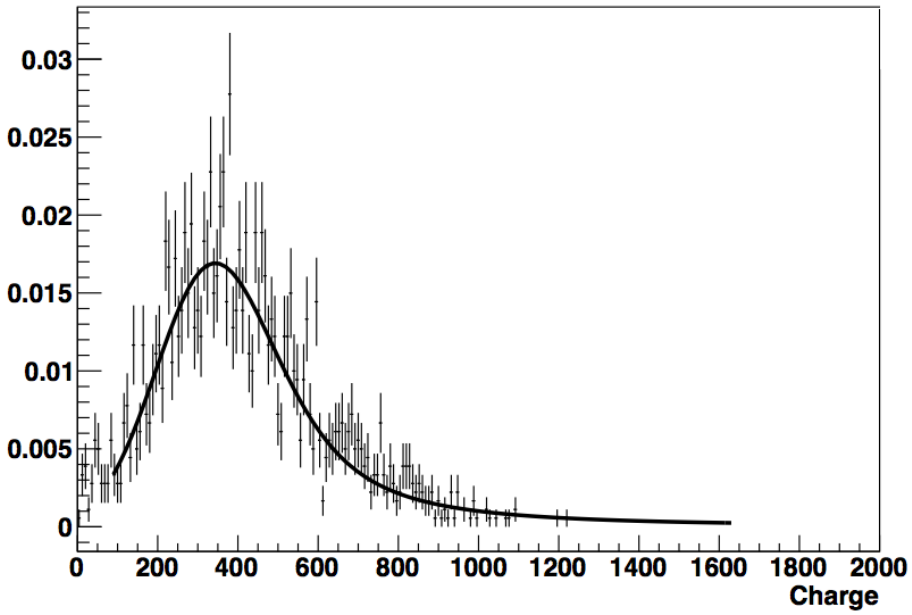

Figure 4.5.6: Detected light distribution for 87 K, after pile-up events were removed.

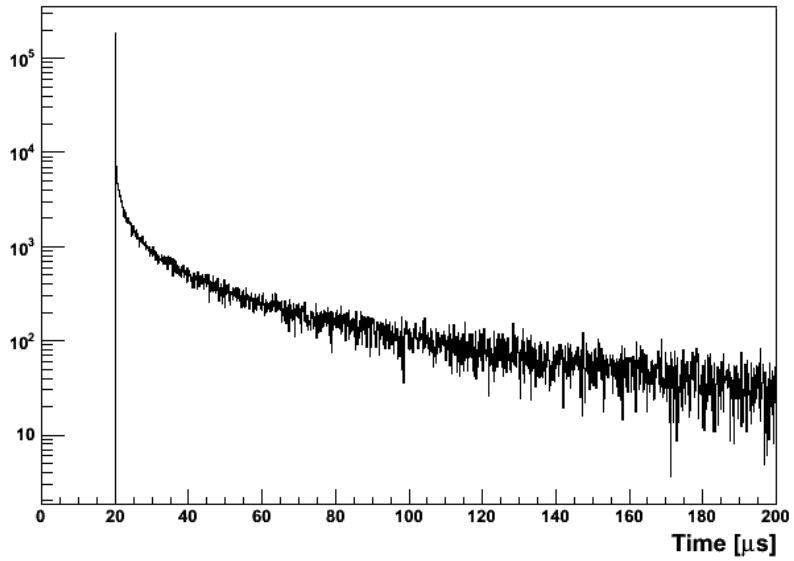

Figure 4.5.7: Pulse shape at 87 K, after pile-up events were removed.

To summarize, three basic data cleaning cuts were applied in the offline analysis in order to remove pathological events (mostly pile-up) [66]. These cuts involved:

- The difference in the first photon arrival times between both channels: $\delta t < 5$ ns.
- The first photon arrival time for PMT1: 19.978 μs $< t_0 <$ 19.985 μs.
- The mean event arrival time for PMT0 (charge weighted, averaged over all photons): typically 30 μs $< t_{av} <$ 50 μs (see also [37]).

This procedure removed up to 80% of events, though for most temperatures, typically 2/3 of the events were removed.

4.5.2 Single Photoelectron Charge

The purpose of investigating the single photoelectron charge in our data was twofold. First, because the time histograms are weighted by the integrated charge per pulse above threshold, we divided the pulse shape histograms by the typical charge value associated with a single photoelectron. This was done to express the histogram bins in terms of photoelectron counts, in order to verify that we had a sufficient number of photoelectrons for the statistical analysis and proposed bin sizes. Secondly, we expect the tail of the pulse shapes to contain only single photons. If the threshold is such that many of these single photons are below the threshold, the tail will be distorted and the fit results will be a consequence of threshold effects rather than scintillation characteristics.

Figure 4.5.8 is a histogram of integral charge detected at times later than 170 μs for temperatures 300 K to 150 K. The expectation is that after the initial burst of photons in a scintillation event, the light reaching the PMTs is so faint that a significant fraction of the detected pulses should be due to single photons arriving

at the PMT. In this distribution, we find three basic populations: (i) a distinct population of very low charge events, (ii) a peak between 3 and 4 V, and (iii) an extended tail beyond 4 V. The low charge events (i) were particularly troubling, as their interpretation was not straightforward. In Figure 4.5.9, we can see that this low charge population exists throughout all 200 μs of pulse shapes, and fades in a similar way to the rest of the scintillation light (see also Appendix A), and thus does not allow us to immediately discard these events as noise. Further investigation into the nature of these populations found that they are distributed according to pulse width, where width was measured in units of 1 ns (which was fixed by the digitization rate), where the low charge events are made entirely of width-1 pulses (Figure 4.5.10). This distribution was found to remain constant according to both time and temperature, while no evidence of baseline effects or ringing was found (refer to Appendix A for relevant plots).

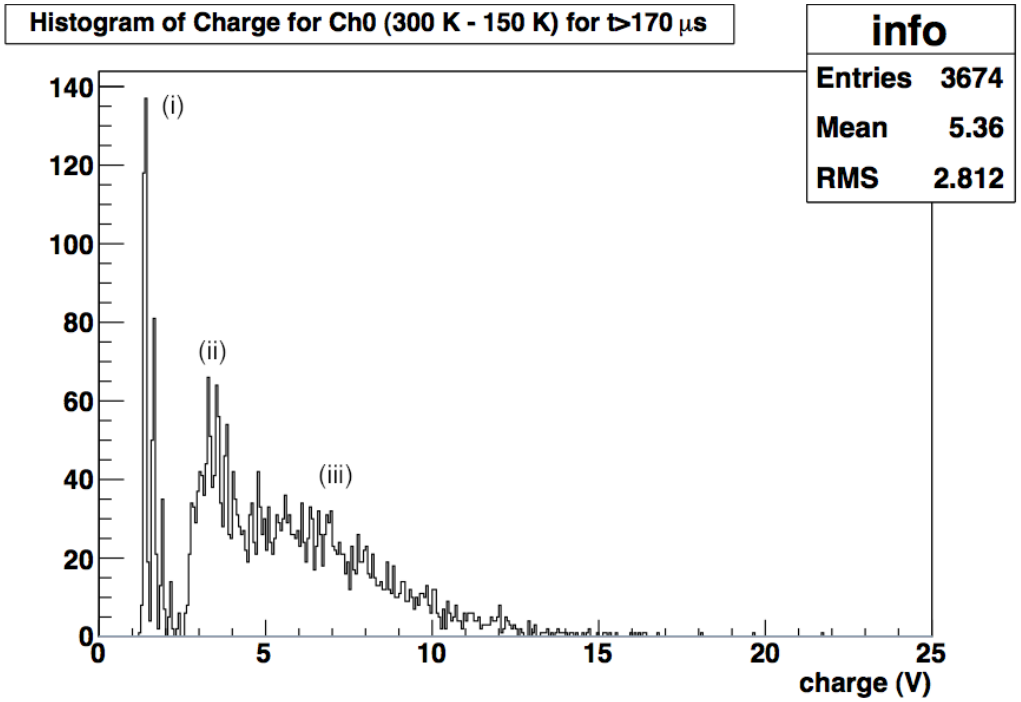

Figure 4.5.8: Histogram of late integral charge (arbitrary units) of pulses with arrival times later than 170 μs. The temperatures range is 300 to 150 K. There are three distinct populations: (i) low charge events below approximately 2 V, (ii) medium-charge events below 5 V, and (iii) an extended tail.

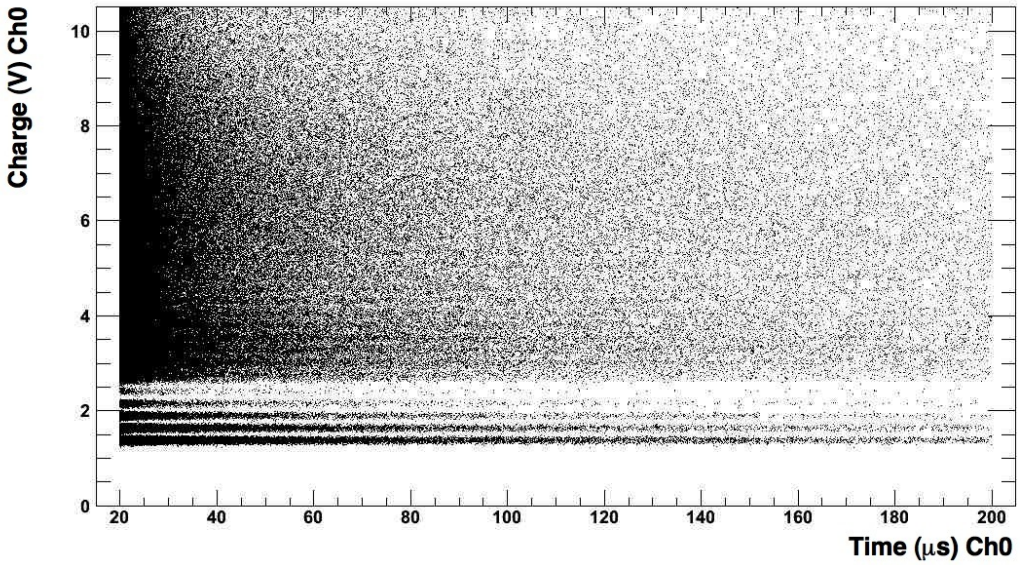

Figure 4.5.9: Scatter plot of the charge (arbitrary units) of individual detected pulses plotted against their time of arrival, for a temperature range of 300 K to 150 K (zoomed in to allow the structure to be more visible). Here we can see the presence of a persistent low-charge signal (below about 2.5 V) which fades with time as the pulse fades.

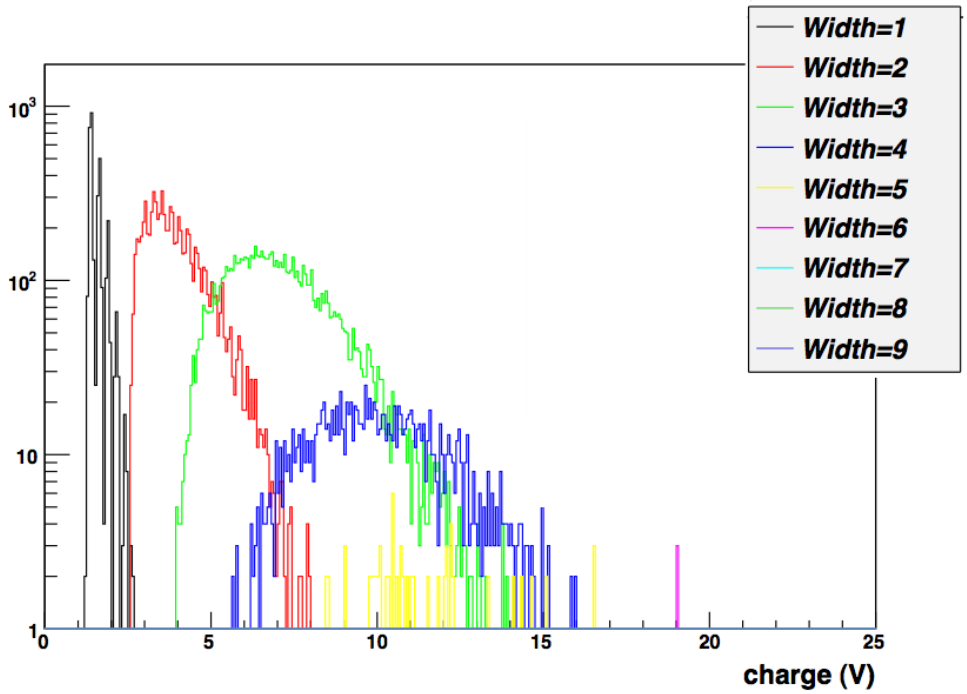

Figure 4.5.10: Histogram of late integral charge (arbitrary units) of pulses with arrival times later than 100 μs (an earlier time was chosen here to ensure the visibility of the higher-width populations). The temperatures range is 300 to 150 K. The data is histogramed according to measured pulse width, where the widths are assigned integer values (multiples of the 1 ns sampling rate) by the data reduction routine. Obviously, pulses with the same width are distributed in distinct charge populations, as expected. Population (i) from Figure 4.5.8 is made entirely of width 1 pulses.

A parallel investigation on the single photoelectron charge by the optical cryostat group at Queen's shed more light on the cause of the charge distribution seen in Figure 4.5.8. Their goal was to measure the single photoelectron charge of a particular photomultiplier tube using a Cherenkov source and maximum distance set-up. When they raised the threshold of their system, both manually and artificially, they found that the singlePE distribution became degraded and was split into three populations, similar to the singlePE distribution from our TPB data (for example, Figure 4.5.11).

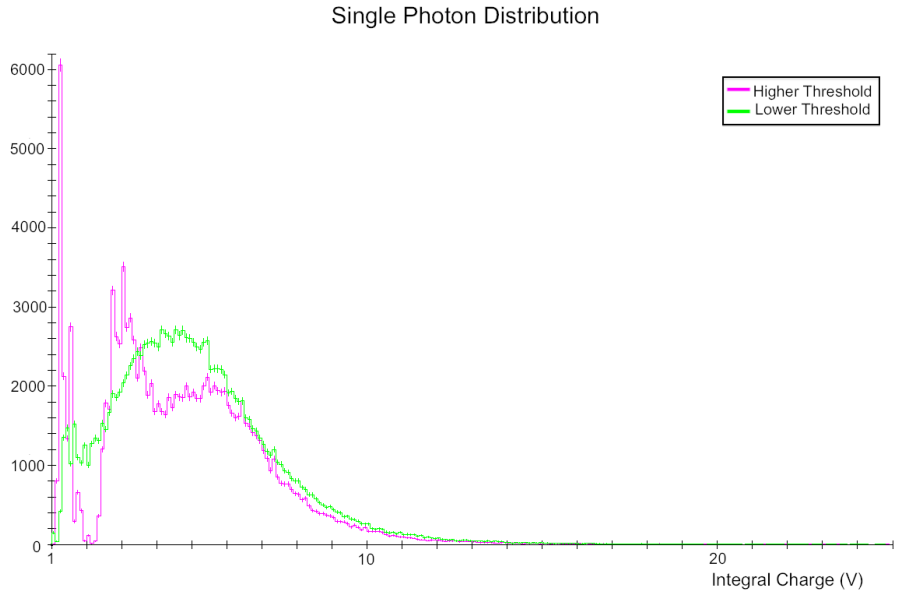

Figure 4.5.11: Single photon distribution from [28]. Two datasets with similar conditions but different online thresholds are superimposed. The higher threshold is clearly distorted, with a distribution very similar to our singlePE distribution from the TPB data.

These plots suggest that the (i) population of pulses from Figure 4.5.8 are true events that have been pushed into the width 1 pulse region due to an imposed threshold that was too high. By comparing the width $w = 1$ populations with the width $w > 1$ populations (refer to Figure 4.5.12) at two different thresholds (one that is very low, and another that is very high) this picture is confirmed. This assures us that these low charge events are in fact true events.

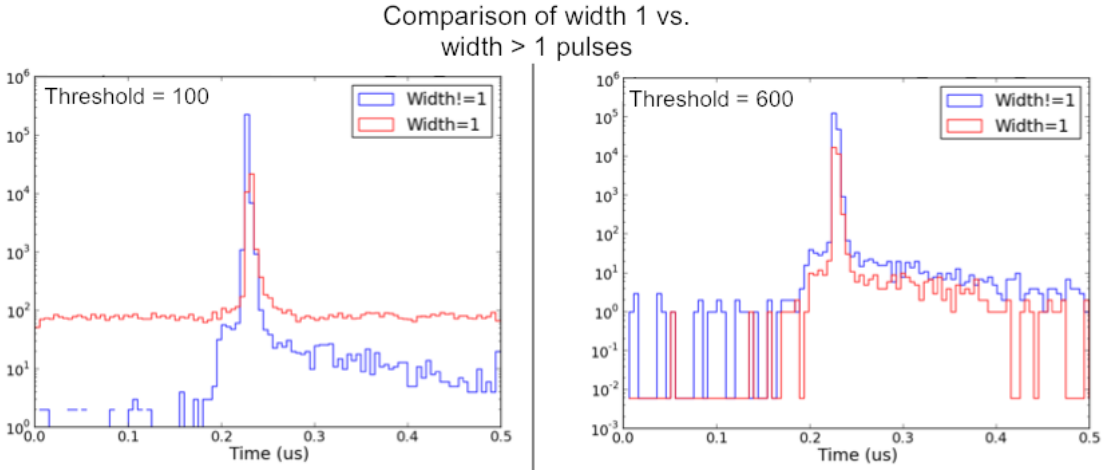

Figure 4.5.12: Pulse shapes from [28]. **Left**: In the low threshold case, the pulses with width 1 contain a flat background throughout the acquisition window. This indicates that the $w = 1$ population in the low threshold case has a large contribution from electronic noise. **Right**: However, if the threshold is higher (in this case, the same threshold as used in the TPB measurement) the $w = 1$ pulses follow the same pulse shape as all other pulses ($w > 1$). This indicates that they originate from the same signal as the rest of the pulses (i.e.: they are due to the incident photons).

However, due to this threshold effect, how to interpret the single photoelectron spectrum of the TPB data (Figure 4.5.8) is not clear. From these investigations, we now had a good understanding of how to set the threshold optimally. To this end, the optical cryostat group performed the single photoelectron charge measurement once more with the photomultiplier tubes used in the TPB measurement, this time with an appropriate threshold choice. This allowed us to extract a value for the single photoelectron charge with confidence, and to then express the histograms in the appropriate units. The resultant measured single photoelectron charge is 5 ± 2 a.u. (Figure 4.5.13) [28].

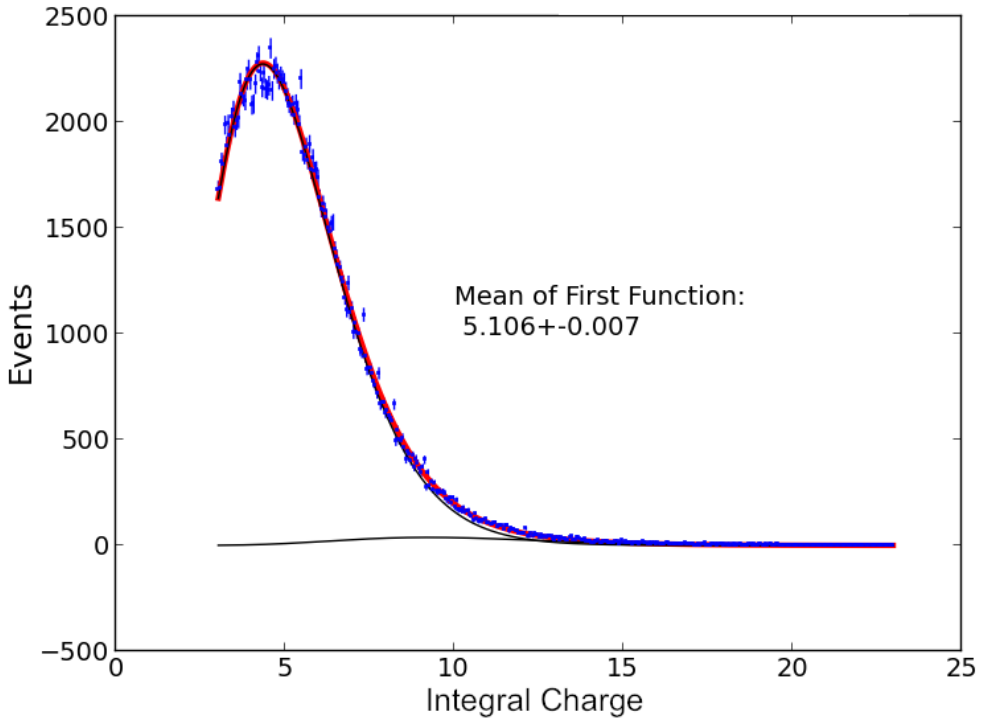

Figure 4.5.13: Single photoelectron spectrum from [28].

Since the threshold used to collect the data was a bit larger than optimal, the efficiency of the PMT's to single photons at the threshold used in the TPB measurement had to be verified. We found that in spite of the chosen threshold, we had a single photon efficiency of 85%, also measured separately [86]. The effect of losing approximately 15% of the single photons is taken into account by the systematic uncertainties quoted in the following sections.

To summarize, we demonstrated that the distorted single photoelectron histogram was a consequence of the chosen threshold, but that in spite of this threshold, we are still efficient to 85% of single photons. Additionally, the single photoelectron charge was determined in a follow up experiment. By dividing the charge-weighted pulse

shape histograms by this charge, we demonstrated that we have sufficient photoelectron statistics for the following analysis (refer to Figure 4.5.14).

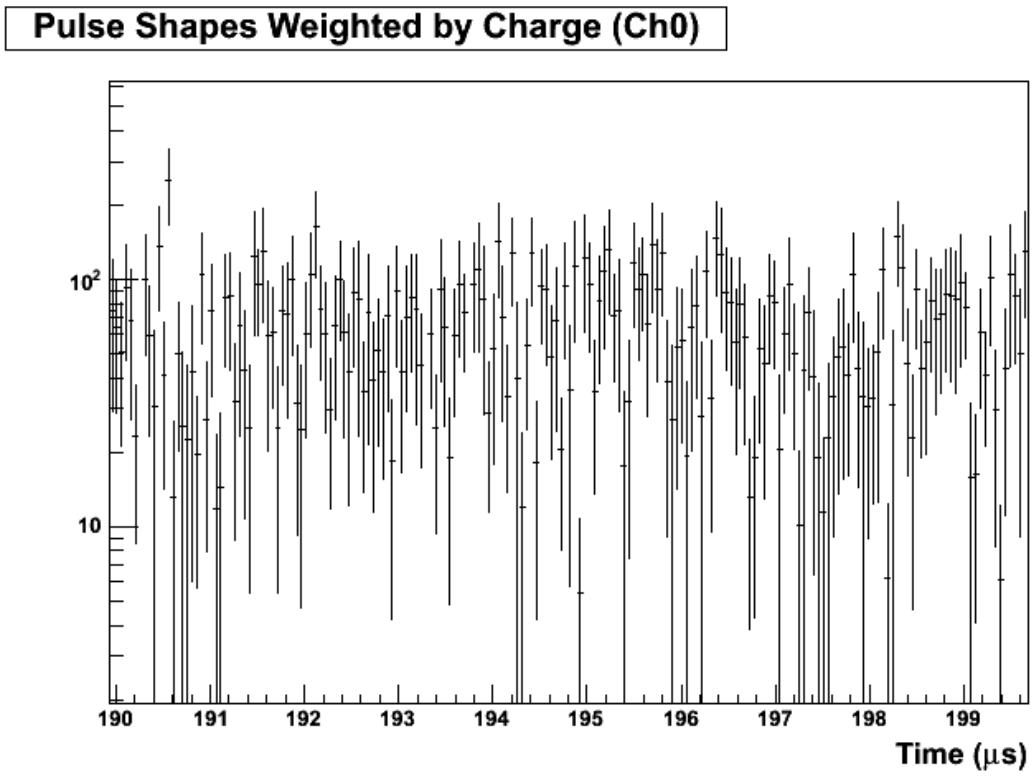

Figure 4.5.14: The late tail of the pulse shape at 87 K in units of counts. We can see that at very late times, the bins have an average of approximately 40-50 counts.

4.5.3 Detected Light and Light Yield

Figure 4.5.15 displays a typical histogram of detected light for alpha-induced TPB scintillation at 87 K (for detected light distributions at other temperatures, refer to Appendix A). A convolved Landau and Gaussian fitting function was used to find the location of the peaks of the distributions.

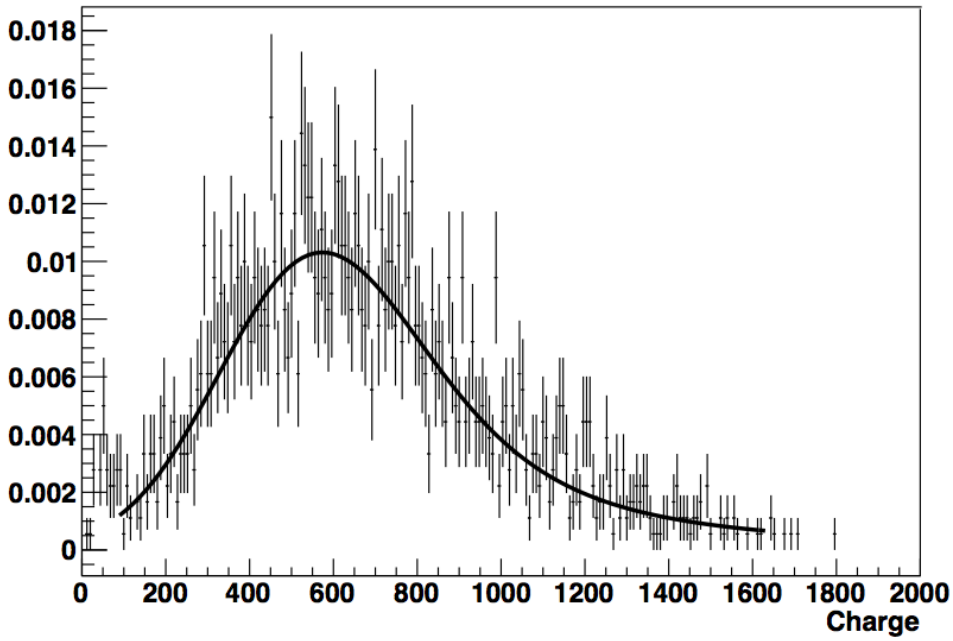

Figure 4.5.15: Detected light distribution at 87 K as measured by both PMTs (0&1).

The fitting function makes use of the built-in Root functions for Landau and Gaussian curves [85]. A convolved Landau and Gaussian fit has been used in other applications, specifically to characterize the energy loss of charged particles through thin layers of silicon [76]. The original thought was to use a pure Landau fit, however the fit was found to be inadequate at finding the peaks at various temperatures. Most likely this is because the surface roughness of the TPB coating (as can be seen in Figure 4.3.2) had an additional broadening effect on the distribution.

Table 4.2 lists the most probable values (MPVs) from the Landau/Gaussian fits of distributions at four sample temperatures. Figure 4.5.16 is a plot of detected light versus temperature (equivalently called light yield here, as we are simply comparing temperatures), where the values used are the MPVs from the fits of the detected

light distributions at each temperature. We can clearly see a reduction in light at temperatures below about 50 K in both PMTs. This indicates a reduction in overall light yield of TPB at low temperatures. At 27 K, we find a light yield that is only 38±2% of the light yield at room temperature, while at 4 K it is only 24±2%. Most notably, the light yield does not degrade from room temperature to 87 K, which is extremely important for the DEAP detector; however, this may be an issue for detectors employing TPB at liquid Neon temperatures. We discuss this in more detail later.

PMT	298 K	87 K	27 K	4 K
0	296±8	298±8	131±5	74±3
1	187±7	194±12	71±2	41±4
0&1	507±22	497±10	208±6	123±6

Table 4.2: Most probable values (MPVs) for the light yield distribution at four sample temperatures. Note that the 0&1 histograms were fit separately, which explains why the light yield in the third row is not quite the sum of the first two rows. Errors shown are statistical as output by Root.

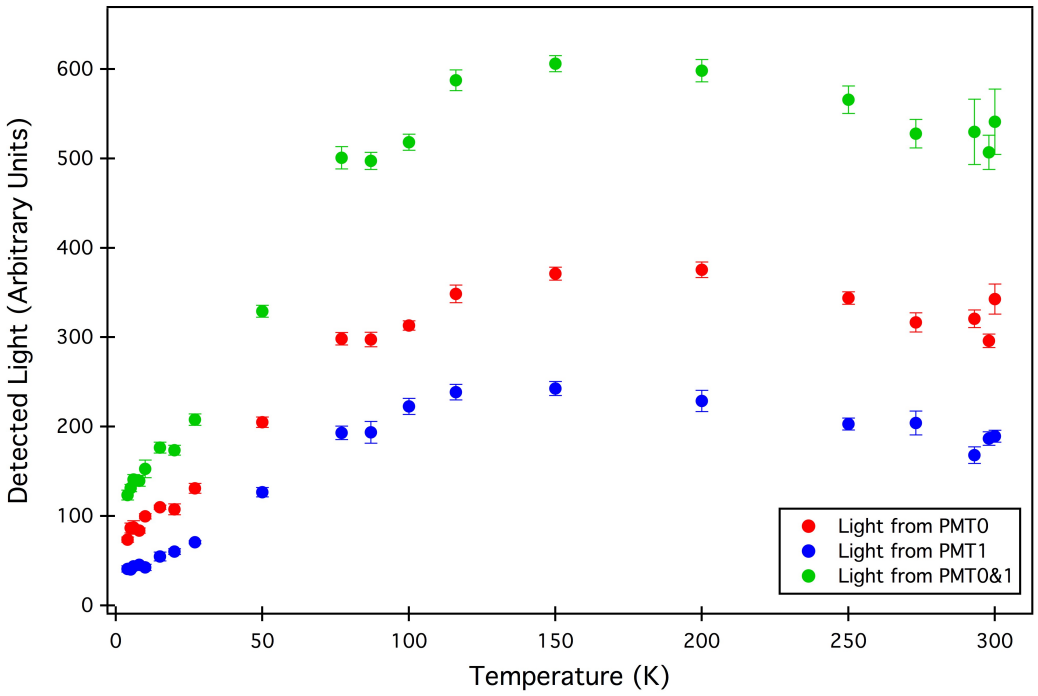

Figure 4.5.16: Detected light vs. temperature for data between 4 K and 300 K.

4.5.4 Pulse Shapes

The pulse shapes were fit using a convolution of a multi-exponential function with the time resolution function ($R(t)$) of the measuring system [74]:

$$F(t) = (\sum_i \frac{N_i}{\tau_i} e^{-(t-t_0)/\tau_i}) * R(t) \tag{4.1}$$

where the time resolution function is approximated as a Gaussian, $R(t) = e^{-t^2/2\sigma^2}$, where σ was determined to be 2 ± 0.5 ns (see below). Four terms were required to satisfactorily fit the data, similar to fits from [92] for alpha-induced scintillation in binary organic scintillators. After convolution, $F(t)$ can be written as:

$$F(t) = (\sum_i \frac{N_i}{\tau_i} e^{[\frac{\sigma^2}{2\tau_i^2} - (\frac{t-t_0}{\tau_i})]})[1 - \mathrm{erf}(\frac{\sigma^2 - \tau_i t}{\sqrt{2}\sigma\tau_i})] + c_0 \tag{4.2}$$

where τ_i are the time constants, σ is the standard deviation of the resolution function, t_0 is the start time of the pulse shape, c_0 is the additive constant, and the N_i are the respective weights of the time constants τ_i. The pulse shape fitting procedures implemented here are based on [92], [74] and [82]. After fitting, the N_i values are normalized by integrating each component separately, and then dividing by the total integral of the pulse shape; the resulting values are called A_i.

The first decay constant, τ_1, has a straightforward relationship to the physics of organic scintillation, as it very close to the actual value of the lifetime of the lower energy singlet excited state [92]. The additional lifetime components arise from a myriad of molecular processes (including phosphorescence processes) and do not have straightforward interpretations [74].

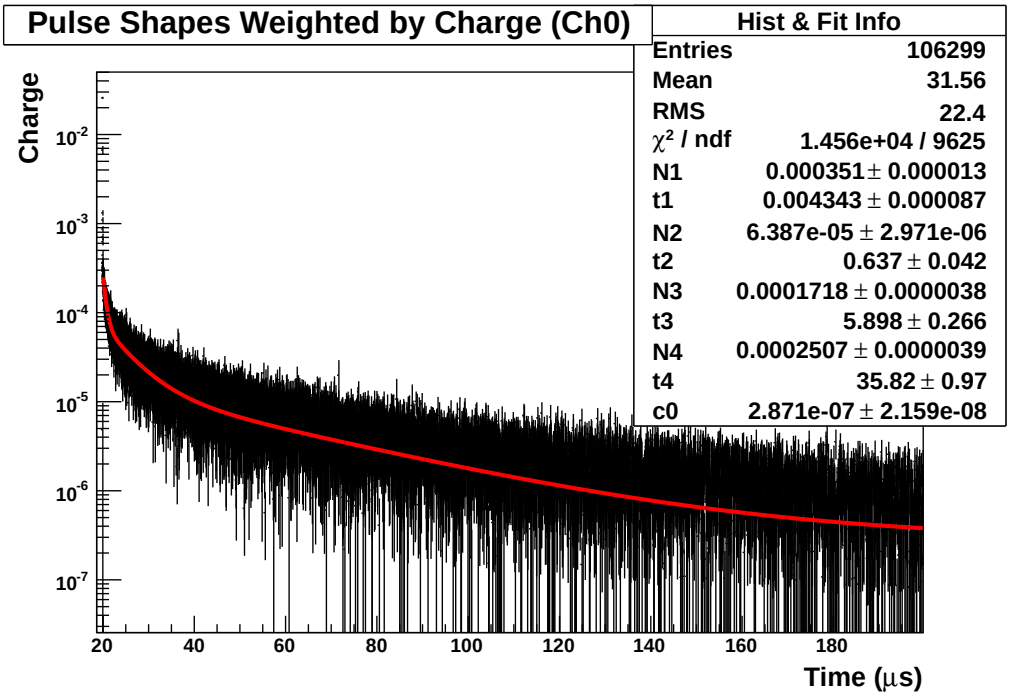

Figure 4.5.17: Sample pulse shape fit at 87 K.

The timing resolution, σ, has a lower limit of 1 ns, which is the sampling rate of the experiment. The resolution is also affected by additional sources of timing uncertainty. The single photoelectron timing jitter of the PMT (due to photons being produced at different positions on the cathode), the error in the determination of the start time of the pulse, and the time jitter of the electronic readout chain all influence the achievable resolution of an experiment [74]. Because of these factors, we expect the resolution to be slightly worse than the sampling rate.

In order to achieve a measurement of the resolution, we first kept σ constant in the fit for several different values between $\sigma = 1 - 2$ ns at a variety of temperatures. This demonstrated that σ only had a significant effect on the values of N_1 and τ_1. We then took the temperature runs with the highest statistics and performed an initial fit

of the entire pulse shape with no fixed parameters. After the first fit, all parameters were kept fixed except for N_1, τ_1, and σ, using the results of step 1. The resulting resolution values were between $\sigma = 1.5 - 2.5$ ns, which is why a value of $\sigma = 2$ was chosen for the final fits of the entire temperature sweep.

The pulse shapes themselves are histograms of the arrival times of the measured photons (or groups of photons), weighted by their integral charge. Because of this weighting, the histograms were divided by the single photoelectron charge, in order to ensure that the counting statistics were well known. The data was then normalized, and fit [94]. Figure 4.5.17 is the pulse shape and resulting fit at 87 K. Refer to Appendix A for pulse shapes at other temperatures, and for a discussion of systematic errors.

Time Constant	298 K	87 K	27 K	10 K
1 ($\pm$0.01)	0.0032$\pm$0.0002	0.0043$\pm$0.0001	0.0028$\pm$0.0002	0.0052$\pm$0.0002
2 ($\pm$0.1)	0.39 $\pm$0.02	0.64$\pm$0.05	0.076$\pm$0.013	0.13$\pm$0.02
3 ($\pm$0.5)	4.4$\pm$0.2	5.9$\pm$0.3	2.1$\pm$0.2	2.5$\pm$0.4
4 ($\pm$1.5)	26.5$\pm$2.8	35.8$\pm$1.2	24.8$\pm$2.1	16.5$\pm$5.4

Table 4.3: Time constants τ_1 to τ_4 at four sample temperatures, in μs. The errors shown are statistical as output by the fitting procedure, while the systematic errors are listed in brackets (in μs) in the first column (see Appendix A).

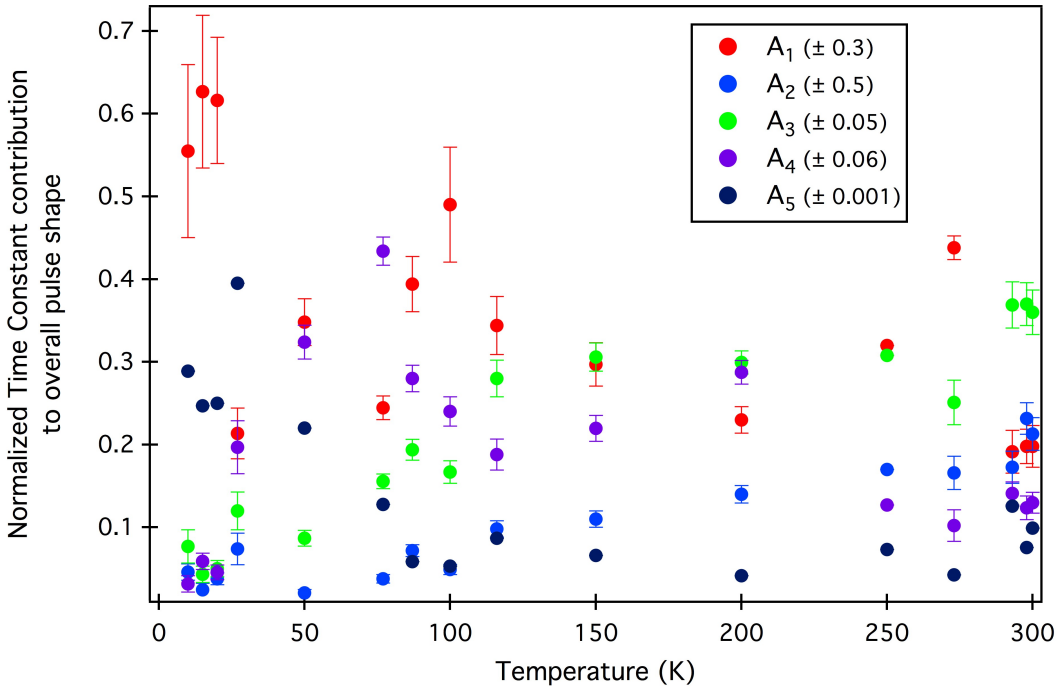

Figure 4.5.18: The contribution of all four time constants (A_1 to A_4), as well as the additive constant (A_5), with respect to temperature, normalized for comparison. Systematic errors, as determined in Appendix A, are listed in the legend, while statistical errors are shown on the plot.

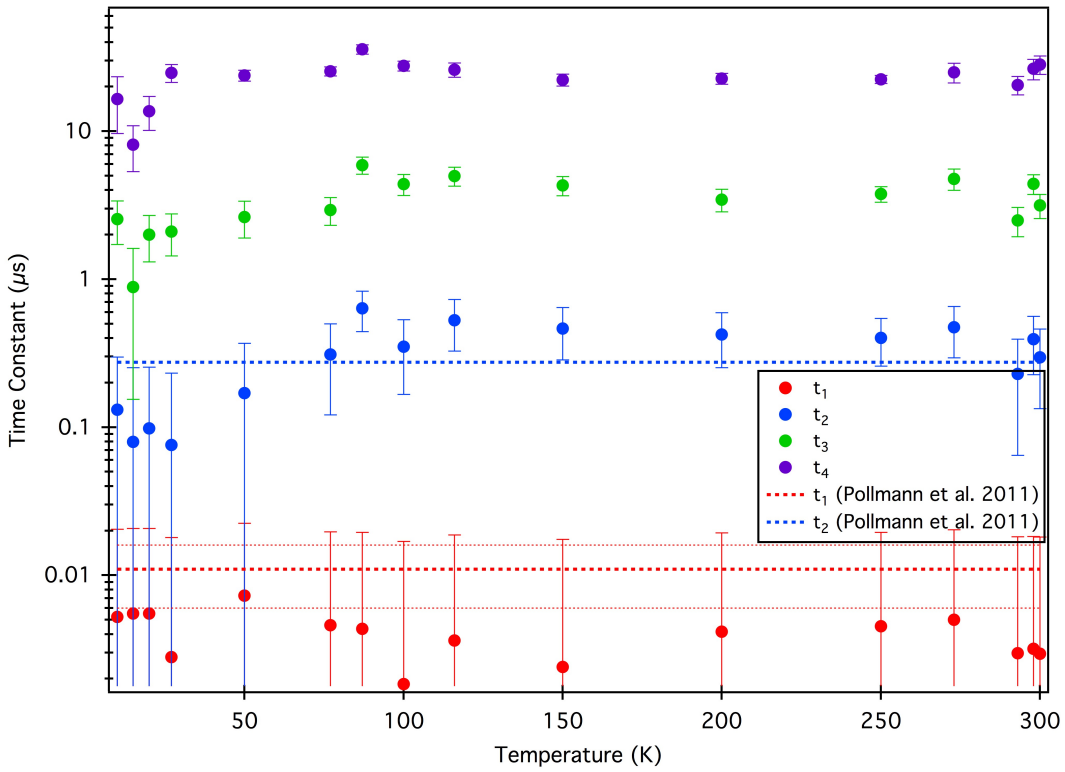

Figure 4.5.19: Time constants with respect to temperature (300 K - 10 K). Errors include both statistical and systematic uncertainties. The dashed lines are the room temperature (RT) measurements from [89]. The dotted lines in red are the τ_1 errors from [89], while the τ_2 errors from [89] are too small to appear on the plot. Note that the room temperature time constants were fit separately in [89], and their associated errors were determined by varying the time windows of each fit.

In Figure 4.5.18, we can see that at very low temperatures, N_1 is significantly larger than the rest of the contributions, indicating that most of the scintillation light occurs at the prompt portion of the pulse. This means that the singlet scintillation channel dominates over the triplet channel at temperatures below about 30 K. Figure 4.5.19 demonstrates that the time constants τ_1 (or t_1 as labelled on the plot) to τ_4 do not change drastically as the TPB sample was cooled from room temperature. The room temperature measurements from [89] are included in this plot, where the second

time constant is consistent with the previous measurement. The first (prompt) time constants are consistently shorter (though always within systematic uncertainty) than the value found by [89], but this is not surprising because in [89] the effect of the finite time resolution of the measurement was ignored.

4.5.5 Prompt Fraction

The discrimination variable for the DEAP experiment was also investigated using the TPB alpha-induced scintillation measurements. The prompt fraction, or "Fprompt" value is a measure of the amount of light in the early versus late portions of the pulse shape (refer to Chapter 3, Section 3.1.1), where

$$\text{Fprompt} = \frac{\text{PromptPE}}{(\text{PromptPE} + \text{LatePE})} \tag{4.3}$$

The calculation of Fprompt was done using the standard DEAP1 time windows. PromptPE refers to the pulse shape integral from $t_A - 50$ ns to $t_A + 150$ ns, where t_A is the leading edge of the pulse. LatePE is the integral between $t_A + 150$ ns and 10 μs. The results, with respect to temperature, are shown in Figure 4.5.20.

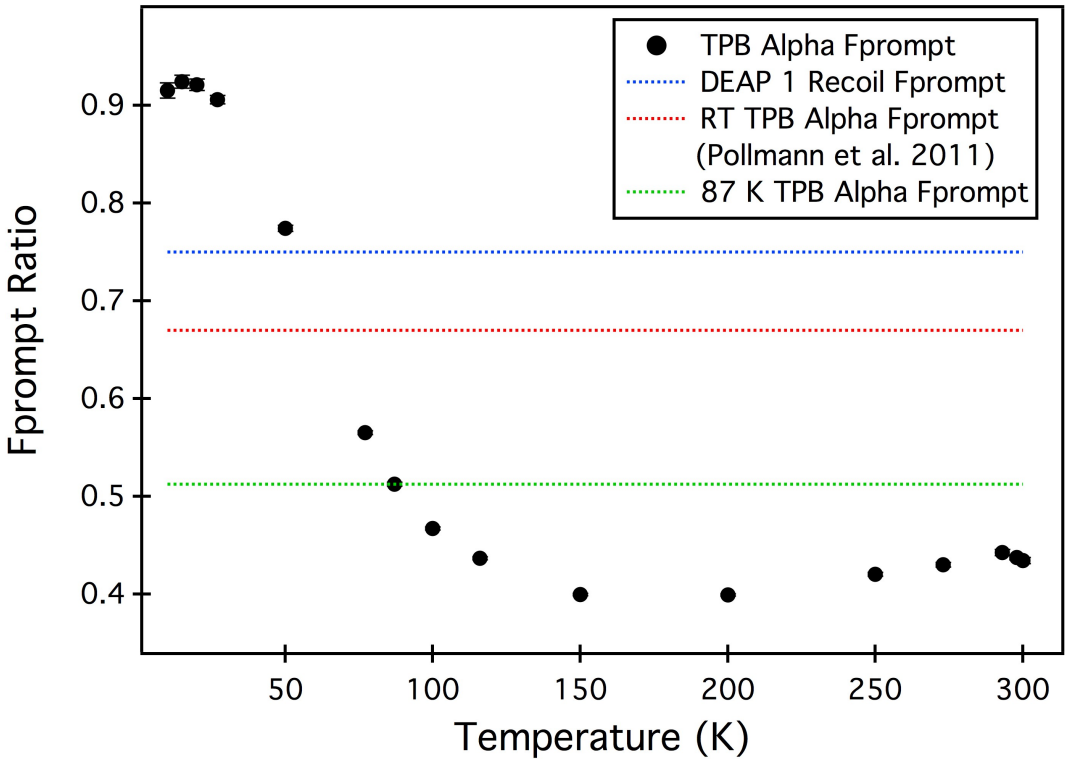

Figure 4.5.20: Fprompt vs. temperature. The red dashed line is the room temperature (RT) measurement of 0.67 from [89] of alphas in TPB, while the blue dashed line is the DEAP-1 nuclear recoil Fprompt value of 0.75 in liquid argon. The green dashed line is the Fprompt measurement at liquid argon temperature of alphas in TPB from the cryostat data (0.512 ± 0.002).

There is a rather large discrepancy between the Fprompt measured at room temperature by [89] for alpha-induced TPB scintillation in comparison to our room temperature results. This has to do with the integration time windows used by [89]. In their room temperature measurement, a total integration time window of 1 μs was used, due to a significant level of noise in the late pulse [91]. However, by using a more sensitive set up, we found that TPB scintillation has a much longer tail than expected at room temperature (lasting well into the 200 μs region), and so using the

DEAP-1 Fprompt time windows reduces the Fprompt values. At very low temperatures, the Fprompt for the [89] time windows is on average 0.97 ± 0.01, compared to an Fprompt of 0.922 ± 0.007 using the DEAP-1 time windows. Evidently, at very low temperatures, the amount of late light is significantly suppressed.

In comparison, if we use the time windows from [89], then our Fprompt value is 0.663 ± 0.005, which is equivalent to the room temperature Fprompt measurement in [89] of 0.67.

4.6 Consequences and Impact on DEAP-3600

4.6.1 Consequences of Light Yield Temperature Dependence

One conclusion from Figure 4.5.16 is that the light yield at room temperature and at 87 K are approximately consistent, which confirms that the use of the light yield measured in [89] for simulations and analysis of liquid argon data as in [88] was appropriate. This measurement also now allows for more accurate values to be entered into the simulations for future work as the analysis for DEAP-3600 is optimized. However, we see a significant decrease in light yield at temperatures below the liquid argon temperature, which is perhaps the most surprising outcome of this measurement. This decrease in light yield has some interesting consequences. In particular, it turns out that the absolute scintillation yield of liquid neon has so far only been measured in the presence of the TPB wavelength shifter (relative to liquid helium) [77]. This indicates that the interpretation of previous neon data should be revised if the temperature dependence of UV scintillation follows the temperature profile that we measure here. One should measure the UV onversion as a function of temperature to see if this interpretation would need to be revised.

An investigation of UV (128 nm) induced TPB scintillation has also been performed down to liquid argon temperatures [22], and to 12 K [23]. They see a reduction in light yield of about a factor of 3 from room temperature down to 12 K, which is consistent with our observations.

One possible effect which would contribute to the decrease in the amount of light detected by our PMTs is a shift in the peak wavelength of TPB scintillation with temperature. A shift in scintillation wavelength outside the peak PMT response could partially account for our observations here. Also worth noting is the red-shifting of UV-induced scintillation light with thicker TPB coatings, as measured by [22], which could be another source of error in our comparison with [89], which used thicknesses of 1 and 4.5 μm vs. the 10 μm thick coating we use here.

4.6.2 Consequences of Time Constant and Fprompt Temperature Dependence

The most obvious conclusion from Figure 4.5.19 is that the time constants of all four components do not evolve with temperature. Because the measured time constants should reflect the decay times of various excited states of the TPB molecule, this is not unexpected. What does change is the amount that each component contributes to the overall pulse shape. This change can be easily seen by the evolution of Fprompt with decreasing temperature (Figure 4.5.20). In fact, at very low temperatures, most of the light from the longer time constants has been lost; about 90% of the light is emitted within the first 150 ns of the pulse. This is likely because intersystem crossing is suppressed at lower temperatures. As discussed in Section 1.1.3, triplet states must be thermally activated in general, since the overlap of vibronic energy

levels of S_1 and higher order triplet excited states allow intersystem crossing to occur. Kinetic energy, in the form of heat, provides the necessary activation energy for this transition to occur. Evidently, below about 100 K, intersystem crossing becomes less likely, with triplet decays becoming quite rare at very low temperatures. This effect is reflected in the observed decrease in light yield, discussed above. It is also evident from Figure 4.5.18 of the normalized time constant amplitudes, that a significant fraction of the total light can be attributed to de-excitations of the longer time constants (i.e.: τ_3 and τ_4). At lower temperatures, these contributions become negligible.

In addition, we have confirmed the presence of a 275 ± 10 ns component to the scintillation pulse shape as measured by [89], where we measure an average value $\tau_2 = 300 \pm 30$ (stat.) $\pm$ 100 (sys.) ns.

Furthermore, we have shown the presence of additional time constant components due to the presence of an unexpectedly long tail in the pulse shape, especially at temperatures above 27 K. These long time constants are 3400 ± 200 (stat.) $\pm$ 500 ns, and 23100 ± 1600 (stat.) $\pm$ 1500 (sys.) ns. We also measure a short time constant of 4 ± 0.1 (stat.) $\pm$ 10 (sys.) ns.

Our measured Fprompt values improve on the measurement done by [89]. The Fprompt of alpha-induced TPB scintillation at liquid argon temperatures is 0.512 ± 0.002, whereas the Fprompt of DEAP1 recoils in the liquid argon itself is 0.75. These are not quite as close in value as originally thought, and this could provide some discrimination between these two sources of light, however, an investigation of long time constants (300 ns or 3400 ns for alphas in TPB versus 1600 ns for DEAP1 recoils in liquid argon) could still be a more viable option in terms of pulse shape discrimination for DEAP-3600. The differences between τ_2 and τ_3 in comparison

to the long liquid argon recoil time constant are 1284 ns and 1820 ns, respectively, providing a promising avenue of background identification in the case of alpha emitters embedded in the TPB coating or inner surface of the acrylic vessel in DEAP-3600. The success of such a PSD technique will be possible to explore once the full detector is operational, now that the relevant time constants and the performance of TPB at the DEAP operational temperature has been determined.

Chapter 5

Construction and Testing of the DEAP-3600 Radon Trap

As discussed in Chapter 3, radon and its progenies are a serious source of background for rare event search experiments. Of particular concern is the alpha decay of radon daughter ^{210}Po, which has a half life of 22.3 years. In the context of the DEAP experiment, any contamination from this isotope will introduce a permanent background signal. One way to introduce this background into the experiment is through the contamination of the argon itself from exposure to the process systems and argon dewar, which likely contain trace amounts of radium. This was proven to be a concern in the DEAP-1 prototype, where spikes in the background rate were seen immediately following the introduction of new argon into the detector.

The best way to mitigate this background source is to remove the radon contamination prior to filling the detector volume. This is accomplished using a dedicated radon trap for the removal of trace amounts of radon from the argon. Radon traps

use activated charcoal as the filtration medium, which have been shown to be sufficiently clean for this purpose. However, should the charcoal itself emanate more radon than expected, there is the possibility that some radon atoms could escape into the detector bulk. To that end, the radon emanation rate of the activated charcoal chosen for DEAP-3600 was measured. We first provide a brief discussion of radon backgrounds in DEAP-1, and then discuss radon filtration and the dedicated radon trap developed for the DEAP-3600 experiment. Finally, testing of the DEAP-3600 radon trap charcoal is discussed, and the results are discussed in terms of their impact on the experiment.

5.1 Radon as a background in DEAP 1

In 2008, large spikes in the nuclear recoil rate were seen in DEAP-1, in spite of the use of ultra-pure liquid argon. As time went on, this rate fell with the lifetime of ^{222}Rn, indicating that radon had somehow entered the argon prior to or during the filling of the detector (see Figure 5.1.1). Leakage through relief valves was ruled out [81], so it is thought that the radon entered the ultra-pure argon through contamination from the storage containers. The containers used to store the ultra-pure argon likely contained trace amounts of radium in secular equilibrium with ^{238}U, thus generating a source of of ^{222}Rn inside the detector material.

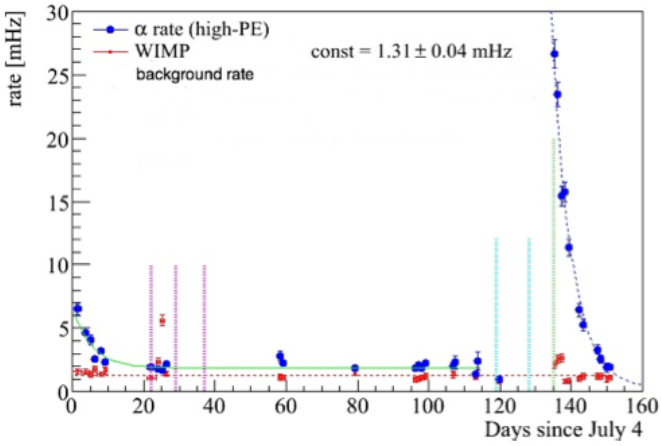

Figure 5.1.1: Alpha (blue) and WIMP-like (red) event rates in DEAP-1 since July 4, 2008 [68]. The initial spike at 0 days since July 4 (day 0) corresponds to when the detector was filled, while the second spike, at day 135 where the dashed green line is marked, corresponds to a top-up of liquid argon after argon levels became low [68]. The other vertical dashed lines indicate specific events affecting the detector, we are only concerned with the initial and second spike. The alpha rates from the initial fill and the subsequent top-up both decay with the lifetime of ^{222}Rn. This suggests that the radon entered the detector with the argon.

The set of data taken just after the light green dashed line (see Figure 5.1.1) is known as the radon spike data. The alpha rates from both the intial fill and the radon spike data decay with a lifetime consistent with that of ^{222}Rn, suggesting that radon was entering the detector with the argon

Due to the radon daughter ^{210}Pb, which has a twenty-two year half-life, contamination from radon lasts "forever" in terms of the lifetime of the detector. Hence, the radon has to be removed prior to filling the acrylic vessel. However, accomplishing this goal chemically was not practical because argon and radon are both noble gases. Instead, the argon was passed through a filter which arrested the flow of radon while allowing argon to pass through. This was accomplished using activated carbon, which

absorbed radon atoms at low temperatures. A dedicated radon trap, filled with 10 g of activated carbon (Carboxen®) was placed after the storage containers and before the argon liquifying column [90]. As a result, on subsequent fills, no increased recoil rate was observed, indicating that the source of radon had been identified and appropriately mitigated. A similar purification process will be used for the DEAP 3600 detector, the design of which is based on the experience of operating DEAP-1, and on much of the Master's work done by Eoin O'Dywer [81].

5.2 Radon Filtration

Charcoal carbon filters exploit the absorption phenomenon, which occurs when fluid particles experience a drop in potential energy due to interactions with a solid surface. In the case of radon absorption, only weak interactions are involved since radon is a noble gas. Because of this, a non-polar material must be selected for the filtration medium, and the trap functions through Van der Waals forces. This process is known as *physical adsorption* and is analogous to the condensation of gas onto cold surfaces. The strength of the forces between the radon atoms and filtration surface, as well as the number of interaction sites, are the crucial factors which contribute to the efficiency of a filter. Activated charcoal is an ideal filtration material because it has an extremely large surface area to mass ratio (of order 1000 m^2/g), allowing for many opportunities of interactions between radon atoms and the carbon surface [87]. Carbon is able to select for radon because radon is a much larger atom when compared to lighter carrier gases such as argon or nitrogen. Because it is larger, it has a higher polarizability and is thus more likely to bind to another surface through Van der Waals forces. However, radon does not remain inside the trap indefinitely; eventually

it desorbs from the charcoal surface. Radon decays with a half life of 3.8235 days, so the longer the radon is retained inside the trap, the less radon remains to eventually be released into the experiment. Heavy metal daughters from radon decays are readily absorbed and retained by the charcoal. Heavy metal adsorption by activated carbon has been studied extensively [24].

Both efficiency and retention time are dramatically increased with decreasing temperature [81]. Because of this, a delicate balance must be achieved in keeping the carbon trap as cold as possible, but not so cold so as to force argon to become a liquid. Cold radon is more likely to encounter and stick to the carbon surface, however, once the argon gas becomes liquid the efficiency drastically decreases. This is because, in a gas, atoms can essentially be considered to be alone in space, and so the radon has a good chance of encountering a charcoal surface. As a liquid, the radon is dissolved in the argon, which causes the difference in binding energy between radon-carbon and radon-argon to be much smaller. This inhibits the ability of radon to stick to the charcoal.

5.3 The DEAP-3600 Carbon Trap Radon Filter

Figures 5.3.1-5.3.3 display drawings of the final design of the DEAP-3600 radon trap system. Table 5.1 lists the trap's specifications.

Nominal Argon Flow Rate	4.9 g/s
Minimum Argon Flow Rate	0 g/s
Inlet Temperature	350 K (max); 300 K (min)
Outlet Temperature	117 K (max); 95 K (min)
Operating Pressure	0-15 psig
Argon Process LIne	0.5" stainless steel, 0.35 wall nominal
Column Flow	vertical with downward argon flow
Cooling	Liquid Nitrogen
Process Connections	VCR
Insulation	Vacuum jacketed can

Table 5.1: DEAP-3600 radon trap specifications.

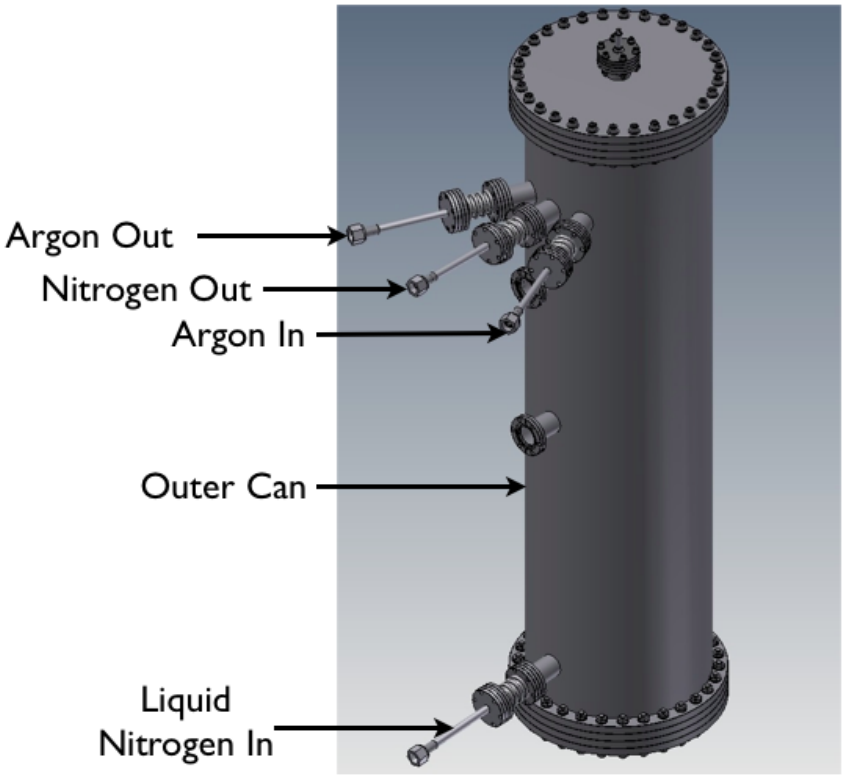

Figure 5.3.1: Drawing of the outer can of the radon trap.

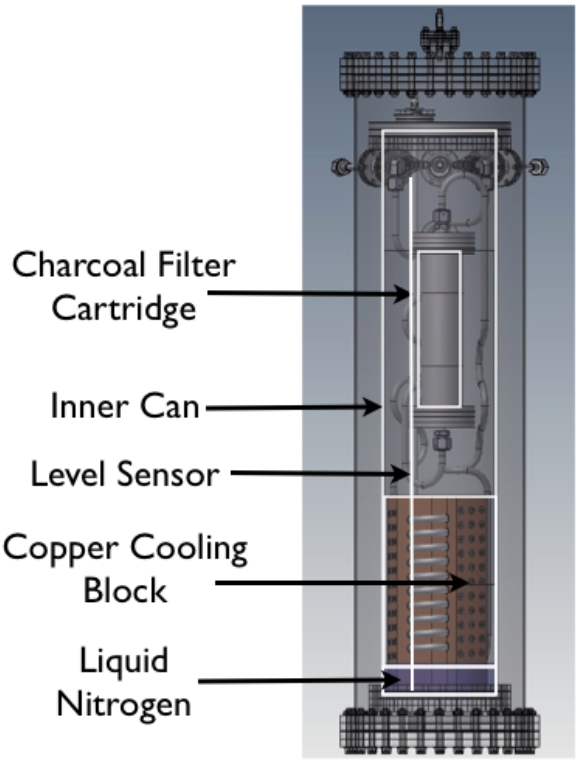

Figure 5.3.2: Drawing of the inner can of the radon trap, and other components.

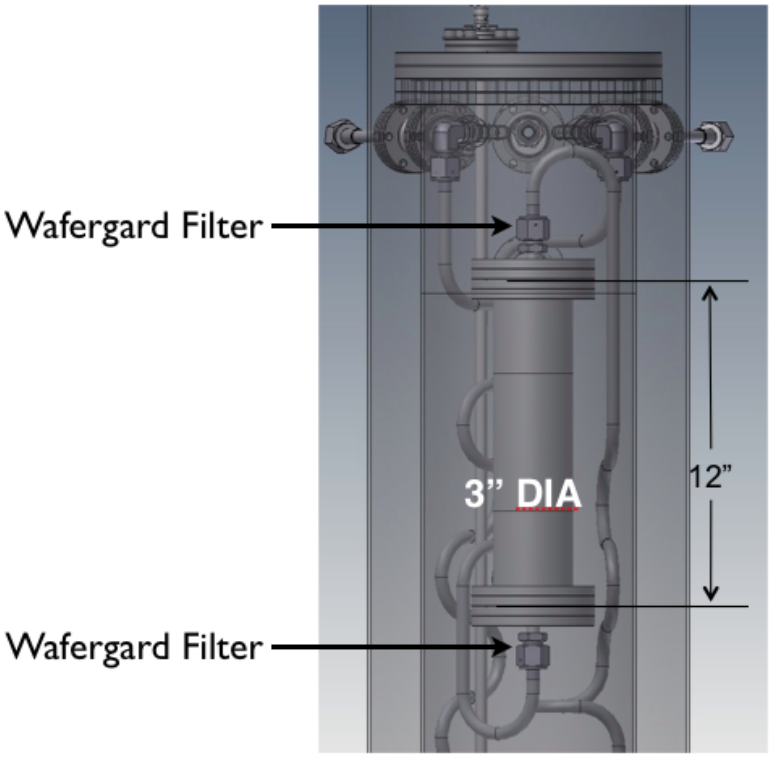

Figure 5.3.3: The charcoal cartridge, protected at either end by a Wafergard filter to retain the charcoal and charcoal dust within the trap.

From now on, the filter itself will be referred to as "the filter" or "charcoal cartridge", while the entire apparatus will be referred to as the radon trap. The cartridge itself is contained inside two vacuum jacketed cans, an "inner can" and an "outer can". The outer can is 12 " diameter and 48" tall, and houses the inner can, which contains the filter cartridge and other necessary parts.

The liquid argon is first cooled by a liquid nitrogen cooling bath, contained within the inner can, and then travels downwards through the filter. A level sensor is submerged in the liquid nitrogen cooling bath in order to monitor the amount of liquid nitrogen in the trap. The nitrogen cools three copper cooling blocks, which themselves

cool the stainless steel argon process line as the argon travels through the system. For contingency purposes, three heaters are imbedded inside the cooling blocks in order to quickly raise the temperature of the system should the argon become too cold, or to trim the temperature to the ideal setting for optimal operation. The heaters are coils (nichrome wire) potted inside steel tubes with ceramic. Temperature sensors have also been placed at key locations within the trap.

The charcoal cartridge itself, with a height of 12″ and diameter of 3″, is filled with 600 g of Saratech® activated charcoal from Blücher Technologies. Saratech® has a surface area of 1342 m^2/g, on the higher end of what is possible in terms of surface area to mass ratios for activated carbon. The filter itself has a "maximum diameter" design. This means that its diameter to height ratio (in this case, 1:4) is larger than usual (radon traps are usually very long and thin). This is to minimize the pressure drop, which will be 4 psi, because a higher pressure is problematic for the DEAP fill system. Two Wafergard filters are installed on either side of the filter to keep dust inside, with an additional filter farther down the line to ensure no dust escapes the trap.

The heat load has been determined through simulation. The argon gas inlet will be at 330 K, while the bottom face will be held at 90 K. It is very important that the argon does not become liquid - both because the efficiency of the trap will decrease, but also because there is a small temperature window where argon will remain liquid and there would be a danger of accidentally freezing the argon, which would completely stop the flow.

Because the charcoal is used as a filter for the radon, it is extremely important to know what the radon emanation rate of this product is. Radon emanated near the

inlet of the cartridge will have a very high probability of remaining trapped by the charcoal, but there is a chance that radon emanating near the outlet could escape the trap with the argon. If the radon emanation rate is, for some reason, quite high, a build up of radon in the filter would decrease the efficiency of the trap. Because of this, the radon emanation rate in the charcoal to be used in DEAP-3600 was measured prior to implementation using the SNO radon emanation system. Although a complete test will only be possible once the full system is built, a sanity check on a small quantity of charcoal was done to ensure the charcoal is reasonably clean. The apparatus, procedure, and results are discussed below.

5.4 Emanation of Saratech® Charcoal at Queen's University

5.4.1 The Emanation Apparatus

Refer to [69] for a detailed discussion of the emanation apparatus at Queens. A brief description is included here.

The Queen's emanation apparatus consists of a vacuum roughing pump, radon board, Lucas cell and a PMT dark box. The purpose of the board is to extract radon from a mixture of other trace gases, such as O_2 or N_2 and to collect the radon from the volume into a Lucas cell. Radon has a higher freezing point, so it can be easily captured and transferred to a Lucas cell.

The main components of the radon board include a large and small trap, which are used to capture the emanated radon, and are made of stainless steel coils filled with brass wool. The brass wool increases the trapping efficiency. Stainless steel Swagelok connectors join the coils to the inlet and outlets of the board, where the outlets provide connections to the Lucas cells. Lucas cells, ZnS-lined scintillator cells,

developed specifically for low counting rates are used for measuring the signal once radon is collected. They work by observing the scintillation light produced by radon and radon-daughter decays. The light is detected by a PMT coupled to the Lucas cell.

The carbon trap, which consisted of a 6″ stainless steel 1/2″ threaded pipe connected to the apparatus using two stainless steal 1/4″-Swagelok to 1/2″-female-NPT connectors, was cleaned prior to emanation by submerging it in an ultra sonic cleaner filled with ultra-pure water for 30 minutes. The loaded trap held 11.2 ± 0.2 g of carbon, with 1/2″ of glass wool and two 1/2″ thick aluminum disks on either end to hold the carbon in place. Two filters were installed at either end of the carbon trap to ensure the charcoal would not escape into the rest of the apparatus. The trap connections were sealed using teflon tape and the entire system was leak tested prior to use.

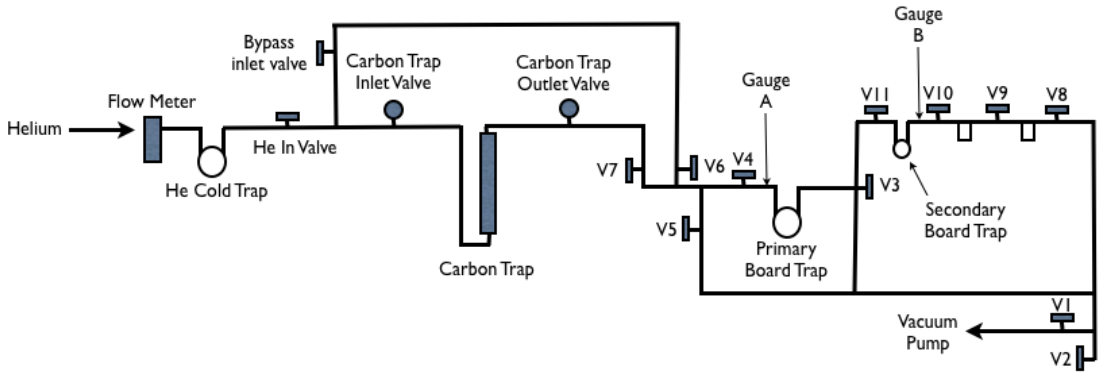

Figure 5.4.1: Schematic of the emanation set-up for the carbon trap.

Because of the unique nature of activated charcoal, it was decided that a carrier

gas would be necessary to remove the emanated radon from the trap. In this case, helium was a natural choice since it would allow for the use of liquid nitrogen for cooling purposes. At liquid nitrogen temperatures, helium remains a gas but radon is very likely to condense inside the large and small radon board traps, allowing for the collection of the radon which emanated from the carbon trap. The helium is always passed through it's own cooled filter (the "helium cold trap") prior to use in order to ensure that no contaminants from the helium tank or flow meter enter the apparatus.

A bypass line was installed (see Figure 5.4.1) to allow for the establishment of helium flow rates (measured using a flow meter) prior to extraction without introducing helium into the carbon trap. A flow meter was placed before the helium cold trap to avoid contaminating the filtered helium. Trap inlet and outlet valves allowed for the careful introduction of carrier gas, while a direct line from the carbon trap to the large (primary) and small (secondary) board traps allowed for the establishment of a helium flow from the carbon trap directly through the collection lines of the radon board for extraction purposes. The emanation and extraction procedures are described in detail in the next section.

Two gauges next to the large and small radon board traps were used to monitor the pressure inside the traps, and a pressure gauge placed by the vacuum pump allowed for the determination of the pressure in all lines open to the pump. A vent valve (V2) beside the vacuum pump was used to vent the helium during emanation preparations and extraction. The Lucas cell used for radon collection was connected beside the small trap at V10.

5.4.2 Emanation and Extraction Procedures

The emanation procedure is straightforward, but because of the nature of the carbon, it is necessary to ensure that the trap is as clean as possible prior to the beginning of the emanation. This involves baking the trap for at least thirty minutes (at 100° C) while flowing clean helium through the trap to remove radon. It has been shown this is a crucial step in [81]; it was found that even at room temperature, much of the radon already captured by the charcoal from previous filtering procedures remained inside, but would escape once a flow rate was established across the trap. After purging, the trap is pumped down to vacuum overnight. Once the trap is deemed clean, it is closed off under vacuum and left to emanate for at least five days. During this period, any ^{226}Ra will produce ^{222}Rn, which will collect as a gas in the trap for subsequent extraction and measurement. At the end of the 5 day collection period, the radon atoms are extracted from the trap and transferred to a Lucas cell for measurement.

The extraction procedure for the emanated charcoal also needed adjustment due to the nature of the material. This is because the carbon is designed to trap and retain radon atoms and other contaminants. An extraction procedure, originally developed by [81], was updated specifically for this radon trap set up. The procedure is as follows:

1. First, pull vacuum on the radon board to remove gas from the extraction system. The helium cold trap is baked to remove radon from the trap. This procedure is repeated on the radon board traps.
2. Helium is cleaned by cooling the helium cold trap using liquid nitrogen. This removes any contaminants in the helium gas prior to introducing helium to the radon trap and radon board system. Liquid nitrogen levels are maintained

throughout the procedure.

3. The radon board is filled with clean helium, and then pumped down to vacuum. This step is repeated twice. The introduction of clean helium flushes out the radon board. This step was designed to minimize the amount of helium passing through the helium cold trap, in order to maintain trap efficiency during the actual radon extraction.

4. Both radon board traps are cooled using liquid nitrogen to prepare for extraction. while the carbon trap is heated to 100° C using heat tape. This lowers the efficiency of the charcoal to retain radon, so that the emanated radon can be swept up by the helium carrier gas once the extraction begins.

5. A helium flow rate of 0.5 SCFH (standard cubic feet per meter) is established through the radon board, bypassing the carbon trap.

6. Once the bypass line is closed off, the flow rate drops to zero and the carbon trap inlet valve is *slowly* opened to introduce a "puff" of helium into the trap. The flow meter should rise as the valve opens, and subsequently begin to drop down again. As the flowmeter returns to zero, the carbon trap outlet valve is opened. Prior to introducing the radon and helium gas to the radon board, the pressure at Gauge A is verified to be positive to ensure the helium will flow into the cold traps and that there will not be any back streaming of air into the system. Once we are sure that no air contamination can occur, the helium is allowed to flow through the board traps. The helium, which does not condense at liquid nitrogen temperatures, continues to flow out of the system, while the cold traps capture the radon atoms. The run start time is recorded as soon as the radon is introduced to the board trap, and a flow of 0.5 SCFH is maintained

for 30 minutes. At this time, the radon should be transferred into the first trap on the radon board.

7. At the end of the run, the valves are closed in reverse order (from right to left on Figure 5.4.1) to ensure that air from the outside does not enter the board traps through valve V2. The helium source is closed off immediately after all valves are closed. The vacuum pump is then used to slowly return the radon board to vacuum. This must be done carefully to ensure that the condensed radon in the board traps does not escape through a sudden change in pressure.

8. After the pressure in the radon board is low enough, the radon from the large trap is allowed to travel to the smaller trap. The regular procedure involves transferring the radon from the primary trap to the concentrator (secondary) trap, and then from the concentrator trap to the Lucas cell. This is accomplished by allowing the radon to diffuse between the system components by heating up first the primary trap and opening the cold concentrator trap. The concentrator trap is then heated, and opened to the Lucas cell. The radon is transferred to the Lucas cell through volume sharing.

9. Once the radon has been collected into the Lucas cell, the cell is removed from the system and attached to a PMT in a dark box for counting. The counting time must be at least the length of a radon half life in order to allow a sufficient number of radon atoms to decay, since it is the alphas emitted during radioactive decay which produce the detected signal.

Five emanations of the Saratech® were done at Queen's University. The third and fourth emanations had to be discarded due, respectively, to mistakes in the procedure and unusually high levels of electronic background coming from elsewhere

in the building. The remaining successful emanations are described below.

5.5 Emanation Results

Prior to emanation, the Lucas cell is first counted in order to determine its background rate. The count rate from the carbon trap is therefore the measured count rate subtracted by the Lucas cell background count, normalized for time:

$$n_{Trap} = n_{Counts} - n_{Lucas} \tag{5.1}$$

where the background rate of the Lucas cell was earlier measured to be 6 $\pm$ 1 counts/day. In order to determine the actual number of radon atoms which decayed, the following equation is used:

$$n_{Rn} = \frac{n_{Trap}}{3 \times E_{single-alpha} \times E_{small-cell} \times E_{large-small} \times E_{trap-large}}. \tag{5.2}$$

On average, each radon atom should produce three alpha decays from ^{222}Rn and its daughters ^{218}Po and ^{214}Po, which explains why the measured count is divided by three. The E values represent the efficiencies of the single-alpha detection of the Lucas cell (0.74 $\pm$ 0.04), the small coil to Lucas cell transfer (0.64 $\pm$ 0.03), the large coil to small coil transfer (0.75 $\pm$ 0.04), and the trap to large coil transfer ($1.00\ ^{+0}_{-0.05}$), respectively [81].

The number of radon atoms present at the beginning of the counting period can

Emanation	Emanation Time (Days)	Counting Time (Days)	Counts	Emanation Rate (Atoms/Day)
0	5.72	5.94	48 ± 10	4 ± 4
1	5.69	6.8	84 ± 14	11 ± 5
2	6.71	7.26	72 ± 13	4 ± 4
3	8.04	5.00	42 ± 10	0 ± 4

Table 5.2: Emanation results of radon emanation of the Saratech® activated charcoal for use in DEAP-3600. Emanation 0 is the emanation of the empty apparatus without the charcoal, while Emanations 1-3 are the results from the loaded trap.

be calculated using the exponential decay equation:

$$\begin{aligned} n_{Rn} &= N_0 - N(t) \\ n_{Rn} &= N_0(1 - e^{-\lambda t}) \\ N_0 &= \frac{n_{Rn}}{1 - e^{-\lambda t}} \end{aligned} \tag{5.3}$$

where λ is the decay constant of ^{222}Rn and t is the counting time t_c. The number of radon atoms in the trap when counting started is

$$N = \frac{n_{Rn}}{1 - e^{-\lambda t_c}}. \tag{5.4}$$

The emanation rate is therefore

$$R = \frac{N \times \lambda}{1 - e^{-\lambda t_e}}. \tag{5.5}$$

where t_e is the time the system was allowed to emanate.

The results of the emanation measurements are given in Table 5.2.

Emanation 0 was the background emanation run, which was performed to determine the combined emanation rate of the empty trap and radon board. Emanations 1 through 3 were performed using the filled trap, and the emanation rates listed in Table 5.2 are the background-subtracted numbers. We can see that the first emanation measurement is larger than the last two. This is not unexpected. Because the carbon had been stored a considerable amount of time open to air, the charcoal likely had a large number of radon atoms retained within it.

Prior to the first emanation, the carbon trap was heated and pumped down for several hours to remove residual gas and contaminants, and then was kept under vacuum overnight. The next day, the pressure in the carbon trap was still quite low, indicating that much of the residual gas had been removed. The emanation procedure was then performed (purging the trap, pulling vacuum, etc).

The last two runs are averaged to provide an effective emanation rate of 2 ± 3 atoms/day. Dividing by the total mass of the carbon, this corresponds to 180 ± 240 atoms/day/kg or 2 ± 3 mBq/kg. This corresponds to an upper limit on the emanation rate of 5.8 mBq/kg at 90% confidence level.

As discussed in Chapter 3, the radon emanation limit for the radon trap is <5 mBq. An upper limit of 5.8 mBq/kg is reasonably close to the desired limit, and, in the last two cases, the measured emanation rates are consistent with zero. This gives us confidence to fill the DEAP-3600 trap and proceed with construction. A more accurate measurement of the built assembly will be possible once the DEAP-3600 apparatus is complete.

5.6 Expected ^{222}Rn Contamination

Assuming the predominant ^{222}Rn contamination comes from radon emanation of the charcoal, approximately 110 $\pm$ 140 atoms/day should be produced inside a radon trap filled with 600 g of Saratech®. These radon atoms will travel through the trap at an average speed of $v = L/\tau$, while the argon gas is flowing, where L is equal to the length of the trap and τ is the break through time of the charcoal. Break through times have been measured previously ([81]) for the activated carbon brand Carbo-Act F2/F3. Because radon absorption characteristics for the Saratech® brand have not been explicitly measured at the temperatures we are interested in, we use the breakthrough time for Carbo-Act F2/F3 for our estimates here. The break through time (the length of time for radon to "break through" a filter) has a temperature dependence [81]:

$$\tau = \kappa e^{\Lambda/T} \tag{5.6}$$

where κ (minutes) and Λ (K) are constants that depend on the carbon in use, and T is the temperature of the trap. For the Carbo-Act carbon, $\kappa = (0.5 \pm 0.2) \times 10^{-4}$ minutes, and $\Lambda = 3615 \pm 106$ T [81]. For a maximum temperature of 117 K (from Table 5.1), the break through time is around 2500 years, well above the longest amount of time DEAP would need to filter the argon. Here we assume a more conservative break through time of $100 \times t_{run}$, as in [81], where t_{run} is the time taken to filter the argon (taken to be a maximum of one month, as in [21]), which gives us a speed v of 3.67 cm/year.

If radon has emanated a distance that is farther from the exit than $d = v \times t_{run}$,

then it will not escape the trap (where $d \leqslant L$). The total number of atoms that passes into the trap, N, is therefore given by [81]:

$$N = \int_0^{t_{run}} \frac{t_{run} - t}{\tau} R_e m \, dt = \frac{R_e m}{2\tau} t_{run}^2 \tag{5.7}$$

where R_e is the emanation rate (atoms per unit mass per unit time) of the charcoal, and m is the mass of the charcoal inside the trap. With an emanation rate upper limit of 490 atoms/kg/day, and a total charcoal mass of 600 g for the DEAP-3600 trap, we can expect that a maximum of approximately 40 radon atoms will escape from the trap during filling.

Considering the large uncertainties in this estimate, a maximum of 40 radon atoms is an acceptable upper limit. Even in the worst case scenario, since the majority of the decays from these atoms should occur in the bulk of the liquid argon, due to their high energy deposition, they will be easily identifiable once the detector is operational. Of course, there is the small possibility that some of these radon atoms, or their daughters, could avoid the TPB and absorb into the acrylic, and thus possibly produce recoil-like signals in the detector. However, we expect that other surface contaminates should dominate this signal. Furthermore, thanks to the work in Chapter 4, it is possible that these events will be identifiable with the development of a PSD technique based on the characteristics of alpha-induced TPB scintillation.

Chapter 6

Summary and Conclusions

One of the most important issues in high sensitivity experiments is the reduction, characterization, and identification of background events which can mask the desired signal. This thesis focuses on two such sources of background for the DEAP-3600 direct dark matter search experiment. The DEAP-3600 detector will consist of 3600 kg of liquid argon encased inside an ultra-pure acrylic vessel. The inner layer of the acrylic vessel will be coated in 1 μm of the wavelength shifter tetraphenyl butadiene (TPB), which will shift the argon scintillation signal from the UV to visible regime for subsequent detection. Of particular concern are surface events, which are the result of alpha emitters embedded inside the detector inner surface, or the TPB layer itself. Additionally, contamination of the liquid argon target material, due to trace amounts of radium in the argon storage containers and process systems, also generate a source of background events inside the detector material (mostly due to the decays of ^{222}Rn and its daughters). This issue was a concern in DEAP-1, which found a marked increase in backgrounds immediately prior to filling the detector, and was solved by building a dedicated radon trap for argon purification. In this thesis, we

discuss two methods for background reduction which pertain to the issues mentioned above: identification, and removal.

In the case of TPB scintillation, because there is always the possibility of surface contamination, the development of a pulse shape discrimination technique for the identification of alpha emitters in TPB is of great importance. However, in order to properly identify these backgrounds, the scintillation characteristics of TPB at DEAP-3600 operational temperatures must be known. To accomplish this, we performed an investigation on alpha-induced TPB scintillation at temperatures ranging from 300 K to 3.4 K, with particular attention paid to liquid noble temperatures. Of particular interest to DEAP, we found that the light yield of alpha-induced TPB scintillation at room temperature and 87 K is consistent. This justifies the use of previous light yield measurements (performed at room temperatures) in the simulation and analysis of liquid argon data, as well as providing more accurate values to be used in future work. The most surprising result is the reduction of light yield at liquid neon temperatures (an efficiency of 38$\pm$2% relative to room temperature).

In addition to the light yield results, we also confirm the presence of a slow component in alpha-induced TPB scintillation. We find a total of three late time constants. These time constants are τ_2 = 300 $\pm$ 30 (stat.) $\pm$ 100 (sys) ns, τ_3 = 3400 $\pm$ 200 (stat.) $\pm$ 500 ns (sys.), and τ_4, 23100 $\pm$ 1600 (stat.) $\pm$ 1500 (sys.) ns. We also measure a short time constant of τ_1 = 4 $\pm$ 0.14 (stat.) $\pm$ 20 (sys.) ns. This short time constant is consistent with the short time constant of UV-induced scintillation, indicating that the same excited state is likely activated in alpha scintillation. The long time constants, particularly τ_2 and τ_3 which differ significantly from the long time constant of a recoil nucleus measured in DEAP-1, are of great interest for the

DEAP experiment, as they provide a promising avenue for the development of a PSD technique based on these differences.

For example, we measure the Fprompt value of alpha scintillation in TPB, and investigated the corresponding contributions of each time constant relative to temperature. We measured an Fprompt value of 0.512 ± 0.002, which will allow discrimination of events in TPB from events in argon, where the Fprompt was measured to be 0.75. This is excellent news for DEAP-3600, especially since previous measurements seemed to indicate that the Fprompts of these events were more similar. Another interesting consequence of this measurement is the significant reduction in late light at temperatures below about 100 K. At liquid neon temperatures, about 90% of the light is emitted within the first 150 ns of the pulse. This is the result of the suppression of forbidden triplet states at lower temperatures, which are no longer accessible. This effect can also be seen in the contributions of the late time constants, which become negligible at low temperatures.

Of course, in addition to identifying any contaminants within the detector, the presence itself of radon and radon daughters must be mitigated as much as possible. In particular, we focus on the filtration of the argon detector material prior to the filling of the detector, using a dedicated radon trap. Of significant concern is the emanation rate of activated charcoal, the filtration medium. This material is an extremely efficient filter, however, should an unexpectedly high amount of radon emanate near the outlet of the filter cartridge, it is possible for some radon to escape inside the detector. In order to confirm the cleanliness of the chosen charcoal to be used in the DEAP-3600 radon trap, which must emanate at a rate below 5 mBq, a small amount of the chosen charcoal was emanated using the SNO radon emanation

system at Queen's University. We find the result is consistent with zero, but report a conservative upper limit on the emanation rate of 5.8 mBq/kg, at 90% confidence. This corresponds to an estimated maximum of 40 radon atoms escaping into the detector. Considering the large uncertainties on this measurement, due to both the low statistics and the small sample, this is an acceptable upper limit, and allows us to proceed with confidence in our choice of charcoal. Testing of the DEAP-3600 radon trap itself will provide a more accurate measurement once the apparatus is complete.

In conclusion, we characterize the scintillation properties of alpha events inside TPB, which will be of great use in the future development of DEAP-3600 simulations and analysis techniques. We also confirm that the chosen charcoal is of sufficient cleanliness for use in the DEAP-3600 radon trap.

Bibliography

[1] Aalseth, C.E. (CoGeNT). *Results from a Search for Light-Mass Dark Matter with a P-type Point Contact Germanium Detector*, Phys. Rev. Lett. 106, 13 (2010).

[2] Adams, J.S. et al. *Scintillation and Quantum Evaporation Generated by Single Monoenergetic Electrons Stopped in Superfluid Helium*, Journal of Low Temperature Physics, 113, 1121 (1998).

[3] Ahlen, S., et al. *The Case for a Directional Dark Matter Detector and the Status of Current Experimental Efforts*, Int. J. Mod. Phys. A 25, 1 (2010).

[4] Akerib, D. *Direct Detection of WIMP Dark Matter: Part 1 - a primer*, presentation for the SLAC Summer Institute, (2007).

[5] Angloher, G., Bauer, M., Bavykina, I., Bento, A., Bucci, C., Ciemniak, C., Deuter, G. & von Feilitzsch, F. et al. (CRESST) *Results from 730 kg days of the CRESST-II Dark Matter search*, Eur. Phys. J. C 72:1971 (2012).

[6] Agnese, R. et al. (CDMS). *Dark Matter Search Results Using the Silicon Detectors of CDMS II*, accepted for publication in Phys. Rev. Lett. arXiv:1304.4279v2 (2013).

[7] Baker, J.H., Galunov, N.Z., & Tarasenko, O.A. *Variation of Scintillation Light Yield of Organic Crystalline Solids for Different Temperatures*, IEEE Transactions

on Nuclear Science Vol. 55, No. 5 (2008).

[8] Baltz, E. A. *Dark Matter Candidates*, SLAC Summer Institute on Particle Physics, Aug. 2-13 (2004).

[9] Begeman, K. G., Broeils, A. H., & Sanders, R. H. *Extended rotation curves of spiral galaxies: dark haloes and modified dynamics* MNRAS, 249, 523 (1991).

[10] Bennett, C. L. et al. *Nine-Year Wilkinson Microwave Anisotropy Probe (WMAP) Observations: Final Maps and Results*, arXiv:1212.5225v2 [astro-ph.CO] January 30, 2013.

[11] Bergström. *Antimatter and Gamma Rays from Dark Matter Annihilation*, 10th Int.Conf. on Topics in Astroparticle and Underground Physics (TAUP2007). Journal of Physics: Conference Series 120:042005 (2008).

[12] Bernabei, R. et al. (DAMA) *First results from DAMA/LIBRA and the combined results with DAMA/NaI*, Eur. Phy. J. C 56: 333-355 (2008).

[13] Bernabei, R. et al. (DAMA) *Dark Matter investigation by DAMA at Gran Sasso*, Int. J. Mod. Phys. A 28, 1330022 (2013).

[14] Bertone, G., Hooper, D., & Silk, J. *Particle Dark Matter: Evidence, Candidates and Constraints*, Physics Reports, 405, 279390 (2005).

[15] Birks, J. B. *Photophysics of Aromatic Molecules*, Wiley-Interscience: London (1970).

[16] Brown, A. private communication on behalf of the XENON collaboration (2013), retrieved from DMTools Sept. 2013.

[17] Bond, J.R. and Szalay, A.S. *The collisionless damping of density fluctuations in an expanding universe*, Astrophys. J. 274, 443 (1983).

[18] Boulay, M.G. & Hime, A. *Direct WIMP Detection Using Scintillation Time Discrimination in Liquid Argon*, arXiv:astro-ph/0411358v1, (2004).

[19] Boulay, M.G. et al. *Measurement of the scintillation time spectra and pulse-shape discrimination of low-energy β and nuclear recoils in liquid argon with DEAP-1*, arXiv:0904.2930v1 [astro-ph.IM], (2009).

[20] Burle Industries, Inc. *Photomultiplier Handbook*, Burle Technologies, Inc, (1980).

[21] Cai, B. et al. *Surface background control in DEAP-3600*, DEAP Internal Report STR-2010-011v6 (2010).

[22] Cavanna, F. et al. *VUV-Vis optical characterization of Tetraphenyl-butadiene films on glass and specular reflector substrates from room to liquid Argon temperatures*, arXiv:1304.6117 [physics.ins-det] (2013).

[23] Cavanna, F. et al. VUV-VIS optical characterization of Tetraphenyl-butadiene files on glass and specular reflector substrates from room to liquid Argon temperature, Light Detection in Noble Elements, Fermilab, Batvia, IL USA, May 29-31 (2013).

[24] Chen, J. P. & Lin, M. *Surface charge and metal ion adsorption on an H=type activated carbon: experimental observation and modeling simulation by the surface complex formation approach*, Carbon, 39, 10, 1491-1504 (2001).

[25] H.-C. Cheng, J. L. Feng, & K. T. Matchev. *Kaluza-Klein Dark Matter*, Phys. Rev. Lett. 89, 211301 (2002).

[26] Cheshnovsky, O. *Emission Spectra of Deep Impurity States in Solid and Liquid Rare Gas Alloys*, The Journal of Chemical Physics, 57(11):4628, (1972).

[27] Chu, S.Y.F., Ekstrom, L.P., & Firestone, R.B. WWW Table of Radioactive Isotopes, Version 2.0, February 1999, LBNL, Berkeley, USA.

[28] Clark, M., private communication, May 2013.

[29] Clowe, D. et al. *On Dark Peaks and Missing Mass: A Weak-Lensing Mass Reconstruction of the Merging Cluster System A520*, The Astrophysical Journal, 758:128 (2012), and references therein.

[30] Clowe, D., Gonzalez, A., & Markevitch, M. L. *Weak lensing mass reconstruction of the interacting cluster 1E0657-558: Direct evidence for the existence of dark matter*, Astrophys. J., 604(astro-ph/0312273):596603. 8 p, (2003).

[31] Clowe, D., Randall, S. W., & Markevitch, M. L. *Catching a bullet: direct evidence for the existence of dark matter*, Nucl.Phys.Proc.Suppl. 173, 28 (2007).

[32] Davies, G.J. et al. *UV quantum efficiencies of organic fluors*, Nuclear Instruments and Methods in Physics Research Section B, 117, 421-427 (1996).

[33] M.W. Davidson and Florida State University. *Fluorescence in Microscopy: Basic Concepts in Fluorescence*, Graphics & Web Programming Team in collaboration with Optical Microscopy at the National High Magnetic Field Laboratory. `http://micro.magnet.fsu.edu/primer/techniques/fluorescence/fluorescenceintro.html` Last modified April 8, 2009.

[34] Davis, M. et al. *The Evolution of Large-Scale Structure in a Universe Dominated by Cold Dark Matter*, The Astrophysical Journal, 292:371-394 (1985).

[35] Desai, A. & Moskowitz, A. *DMTools: Dark Matter Limit Plot Generator*, maintained by the Particle Astrophysics Group, Brown University, `http://dmtools.brown.edu:8080/session/new` (2013).

[36] Dienes, K. R., Dudas, E., & Gherghetta, T. *Grand Unification at Intermediate Mass Scales through Extra Dimensions*, Nucl. Phys. B 537, 47 (1999).

[37] Di Stefano, P. et al., *Counting photons at low temperature with a streaming time-to-digital converter*, Nucl. Instrum. Meth. A, 700, 1, 40-52 (2013).

[38] Doke, T., Crawford, H. J., Hitachi, A., et al. *LET dependence of scintillation yields in liquid argon*, Nuclear Instruments and Methods in Physics Research Section A, 269(1), (1988).

[39] Doke, T., Hitachi, A., Kikuchi, J., et al. *Absolute Scintillation Yields in Liquid Argon and Xenon for Various Particles*, Japanese Journal of Applied Physics, 41(Part 1, No. 3A):15381545, (2002).

[40] The Planck Collaboration. *Planck 2013 results. I. Overview of products and scientific results*, arXiv:1303.5062 [astro-ph.CO] (2013).

[41] Duffy, L. D. & van Bibber, K. *Axions as Dark Matter Particles*, New J. Phys. 11 105008 (2009).

[42] ESA and the Planck Collaboration. *Planck's power spectrum of temperature fluctuations in the cosmic microwave background*, retrieved from http://sci.esa.int/planck/51555-planck-s-power-spectrum-of-temperature-fluctuations-in-the-cosmic-microwave-background/ on July 27, 2013, released March 21, 2013.

[43] Falk, T., Olive, K. A., & Srednicki, M. *Heavy Sneutrinos as Dark Matter*, Phys. Lett. B 339, 248 (1994).

[44] Feng, J. L., Rajaraman, A., & Takayama, F. *Superweakly Interacting Massive Particles*, Phys. Rev. Lett. 91, 011302 (2003).

[45] Freese, K., Frieman, J., & Gould, A. *Signal modulation in cold-dark-matter detection* Phys. Rev. D37, 12, 3388 - 3405 (1988).

[46] Freese, K., Fields, B., & Graff, D. *Limits on Stellar Objects as the Dark Matter of our Halo: Nonbaronic Dark Matter Seems to be Required*, arXiv:astro-ph/9904401v1 (2000).

[47] Freese, K., Lisanti, M., & Savage, C. *Annual Modulation of Dark Matter: A Review*, arXiv:1209.3339v3 [astro-ph.CO] (2013).

[48] Formaggio, J. A. & Martoff, C. J. *Backgrounds to Sensitive Experiments Underground*, Annu. Rev. Nucl. Part. Sci. 54:361-412, (2004).

[49] Garrett, K., & Duda, G. *Dark Matter: A Primer*, Advances in Astronomy Volume 2011, Article ID 968283, 22 (2011).

[50] Gastler, D., et al. *Measurement of scintillation efficiency for nuclear recoils in liquid argon*, Phys. Rev. C 85, 065811 (2012).

[51] Gehman, V.M. et al., *Fluorescence efficiency and visible re-emission spectrum of tetraphenyl butadiene films at extreme ultraviolet wavelengths*, Nuclear Instruments and Methods in Physics Research Section A, 654, 116-121 (2011).

[52] Hepworth, J. D., Waring, D. R., & Waring, M. J. *Aromatic Chemistry*, The Royal Society of Chemistry, Cambridge (2002).

[53] Hitachi, A., Takahashi, T., Funayama, N., et al. *Effect of ionization density on the time dependence of luminescence from liquid argon and xenon*, Physical Review B (Condensed Matter), 27:5279, (1983).

[54] Hitachi, A., Doke, T., & Mozumder, A. *Luminescence quenching in liquid argon under charged-particle impact: Relative scintillation yield at different linear energy transfers*, Physical Review B, 46(18), (1992).

[55] Johnson, *Scintillator Purification and Study of Light Propagation in a Large Liquid Scintillator Detector*, PhD Thesis submitted to Princeton University (1998).

[56] Jungman, G., Kamionkowski, M., Griest, K. *Supersymmetric Dark Matter*, Physics Reports, 267 (1996) 195373 .

[57] Kahlhoefer, F. *Sensitivity of Liquid Xenon Detectors for Low Mass Dark Matter*, PhD Thesis submitted to the University of Heidelberg (2010).

[58] Kaluza, T., Sitzungsber. Preuss. Akad. Wiss. Berlin (Math. Phys.) K1, 966 (1921); O. Klein, Z. Phys. 37, 895 (1926) [Surveys High Energ. Phys. 5, 241 (1986)].

[59] Kanaya, N. (ATLAS) *Dark matter searches at LHC*, Detectors and Experiment Techniques, ATL-PHYS-SLIDE-2013-470, submitted to CERN Document server 05 August 2013.

[60] Kiefer, M. *Improving the Light Channel of the CRESST-II-Dark Matter Detectors*, PhD Thesis, Technische Universität München (2012).

[61] Knapp, G. & Kormendy, J. (eds) *Dark Matter in the Universe*, IAU Symposium No. 117, Reidel, Dordrecht (1987).

[62] Knopp, J., Schwetz, T. & Zupan, J. *Global interpretation of direct Dark Matter searches after CDMS-II results*, JCAP, Issue 02, id. 014 (2010).

[63] Koczon, P. et al. *Wavelength shifting materials for the use of RICH detectors - p terphenyl and tetraphenyl butadiene revisted*, PH-HEP-Tech-Note (2012).

[64] Kolb, E. W. & Turner, M. S.. *The Early Universe*, Redwood City, CA: Addison-Wesley, (1990).

[65] Kopp, J., Schwetz, T., & Zupan, J. *Clobal interpretation of direct Dark Matter searches after CDMS-II results*, JCAP 1002, 014, arXiv:0912.4264, (2010).

[66] Kraus, H., Mikhailik, V. B., & Wahl, D. *Multiple photon counting coincidence (MPCC) technique for scintillator characterization and its application to studies of $CaWO_4$ and $ZnWO_4$ scintillators*, Nuclear Instruments and Methods in Physics Research Section A 553, 522–534, (2005).

[67] Lewin, J. D. & Smith, P. F. *Review of mathematics, numerical factors, and corrections for dark matter experiments based on elastic nuclear recoil*, Astroparticle Physics 6, 87-112 (1996).

[68] Lippincott, W. H. *Direct detection of dark matter with liquid argon and neon*, PhD Thesis submitted to Yale University, (2010).

[69] Liu, M., Lee, H. W., McDonald, A. B. *^{222}Rn emanation into vacuum*, Nuclear Instruments and Methods in Physics Research A, 329, 291-298 (1993).

[70] Loer, M. *Towards a Depleted Argon Time Projection Chamber WIMP Search: DarkSide Prototype Analysis and Predicted Sensitivity*, PhD Thesis submitted to Princeton University (2011).

[71] Loosli, H. H. *Earth and Planetary Science Letters*, 63:51-62, 1983.

[72] LUX Collaboration, The Large Underground Xenon (LUX) Experiment, Nuclear Instruments and Methods in Physics Research Section A, Vol. 704, 111-126 (2013).

[73] Mann, R. *An Introduction to Particle Physics and the Standard Model*, CRC Press, Taylor & Francis Group (2010).

[74] Marradán Undagoitia, T., et al. *Fluorescence decay-time constants in organic liquid scintillators*, Rev. Sci. Instrum. **80**, 045501 (2009).

[75] Martin, S. P. *A Supersymmetry Primer*, arXiv:hep-ph/9709356v6 (2011).

[76] Meroli, S., Passeri, D., & Servoli, L. *Energy loss measurement for charged particles in very thin silicon layers*, JINST 6 P06013 (2011).

[77] Michniak, R.A. et al. *Alpha and beta particle induced scintillations in liquid and solid neon*, Nuclear Instruments and Methods in Physics Research A 482, 387-394 (2002).

[78] Mulliken, R.S. *Potential Curves of Diatomic Rare Gas Molecules and Their Ions, with Particular Reference to Xe*, The Journal of Chemical Physics, 52:5170, (1970).

[79] Drawing by Nadeau, P., private communication, Sept. 2013.

[80] NASA/CXC/SAO & references therein, *NASA Finds Direct Proof of Dark Matter*, CHANDRA X-Ray Observatory photo album image of 1E 0657-56 (2006).

[81] O'Dwyer, E. *Radon Background Reduction in DEAP-1 and DEAP-3600*, Masters Thesis submitted to Queen's University (2011).

[82] O'Keeffe, H.M., O'Sullivan, E., & Chen, M.C. *Scintillation decay time and pulse shape discrimination in oxygenated and deoxygenated solutions of linear alkylbenzene for the SNO+ experiment*, Nuclear INstruments and Methods in Physics Research A 640, 119-122 (2011).

[83] Partridge, R. B. *3K: The Cosmic Microwave Background Radiation*, Cambridge University Press, 1995.

[84] Peebles, P. J. E. *The Origin of Galaxies and Clusters of Galaxies* Science 224, 1385 (1984).

[85] Pernegger, H, & Fiedl, M. *Convoluted Landau and Gaussian Fitting Function*, based on Fortran code by R. Fruehwirth, `http://root.cern.ch/root/html/tutorials/fit/langaus.C.html` (last changed 2012-09-14).

[86] Piquemal, M., private communication, May 2013.

[87] Pocar, A. *Low Background Techniques and Experimental Challenges for Bornexio and its Nylon Vessels*, PhD Thesis submitted to Princeton University (2003).

[88] Pollmann, T. *Alpha backgrounds in the DEAP experiment*, PhD Thesis submitted to Queens University, 2012.

[89] Pollman, T, Boulay, M, & Kuzniak, M. *Scintillation of thin tetraphenyl butadiene films under alpha particle excitation* Nuclear Instruments and Methods in Physics Research A 635 127- 130. (2011).

[90] Pollmann, T. (DEAP). *Radon backgrounds in the DEAP-1 liquid argon based Dark Matter detector*, arXiv:1211.0909 [astro-ph.IM], (2012).

[91] Pollmann, T., private communication, Sept. 2013.

[92] Ranucci, G. et al. *Scintillation decay time and pulse shape discrimination of binary organic liquid scintillators for the Borexino detector*, Nuclear Instruments and Methods in Physics Research A 350, 338-350 (1994).

[93] Riess, A.G. et al. *Observational Evidence from Supernovae for an Accelerating Universe and a Cosmological Constant*. AJ, 517, 116, 1009 (1998).

[94] The Root Team. *ROOT User's Guide, ROOT: An Object-Oriented Data Analysis Framework*, <http://root.cern.ch/download/doc/ROOTUsersGuideA4.pdf>, May 2013.

[95] Rosenberg, L. J., & van Bibber, K. A. *Searches for invisible axions*, Phys. Rept. 325 , 1 (2000).

[96] Rubin, V. C., & Kent Jr. Ford, W. *Rotation of Andromeda nebula from a Spectroscopic Survey of Emission regions*. Astrophysical Journal, 159, 379 (1970).

[97] Saab, T. *An Introduction to Dark Matter Direct Detection Searches & Techniques*, WSPC Proceedings, arXiv:1203.2566 [physics.ins-det] (2012).

[98] Sauer, M., Hofkens, J., & Enderlein, J. *Basic Principles of Fluorescence Spectroscopy* in *Handbook of Fluorescence Spectroscopy and Imaging: From Single Molecules to Ensembles*, Wiley-VCH Verlag GmbH & Co. KGaA, Weinheim, Germany. doi: 10.1002/9783527633500.ch1 (2011).

[99] Savage, C., et al., Journal of Cosmology and Astroparticle Physics 2009, 036 (2009), URL http://stacks.iop.org/1475-7516/2009/i=09/a=036.

[100] Limit by Schnee, R. W. (2005), retrieved from DMTools Sept. 2013.

[101] Schnee, R. W. *Introduction to dark matter experiments*, arXiv.org, astro-ph.CO, (2011).

[102] Schumann, M. *Dark Matter Direct Detection Principles*, Class notes Astroparticlephysics, UZH, Physik-Institut, Universität Zürich (2013).

[103] M. von Sievers, private communication, 2012.

[104] Smith, M. C., et al., Monthly Notices of the Royal Astronomical Society 379, 755 (2007), ISSN 1365-2966, http://dx.doi.org/10.1111/j.1365-2966.2007.11964.x.

[105] Song, L. & Fayer, M.D. *Temperature dependent intersystem crossing and triplet-triplet absorption of rubrene in solid solution*, Journal of Luminescence 50, 75-81 (1991).

[106] Spooner, N. *Direct and Indirect Searches for WIMP Dark Matter*, presented at Snowmass (2001).

[107] Szelc, A. M. . *Dark Matter Experimental Overview*, arXiv:1010.3918v1 [astro-ph.IM] (2010).

[108] XENON100 Collaboration, *First Dark Matter Results from the XENON100 Experiment*, Phys. Rev. Lett.105.131302 (2011).

[109] XENON100 Collaboration, *Dark Matter Results from 255 Live Days of XENON100 Data*, Phys. Rev. Lett. 109, 181301 (2012).

[110] Verdier, M.-A., et al. *A 2.8 K cryogen-free cryostat with compact optical geometry for multiple photon counting* Rev. Sci. Instrum. 80, 046105 (2009).

[111] Zwicky, F. *Die Rotverschiebung von extragalaktischen Nebeln*, Helv. Phys. Acta, 6, 110 (1933).

[112] Zwicky, F. *On the masses of nebulae and of clusters of nebulae*, ApJ 86, 3 (1937).

Chapter Appendix

Appendix A

Additional Cryostat Runs and Data Analysis

A.1 Verification of TPB Sample Stability

After the initial temperature sweep down to 3.4 K, an additional run at room temperature (293 K) was completed to verify that no changes in light yield (due to, perhaps, the removal of some TPB coating) had occurred throughout the sweep. Refer to Figure A.1.1 for a comparison between the initial and final room temperature runs. An initial run as close in temperature to the final was chosen for comparison (296 K vs. 293 K for initial and final respectively).

A.2 Blank Quartz Sample

An additional temperature sweep was done with a sample identical to the quartz substrate from the TPB runs, except with no TPB coating. This was done in order

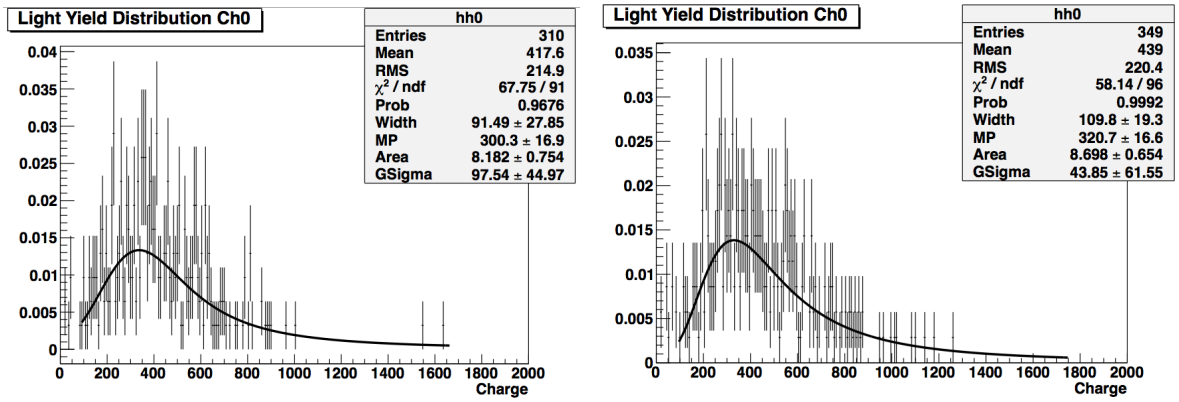

Figure A.1.1: Room temperature measurement (296 K) at the beginning of the temperature sweep (right). Room temperature measurement (293 K) at the end of the temperature sweep (left) for light detected by PMT0. At 296 K, we find a peak value (MPV) of 300.3 ± 16.9 in comparison to 320.7 ± 16.6 at 293 K.

to verify that the quartz substrate did not contribute to the scintillation light attributed to the TPB. A detected light distribution from the 87 K blank quartz run is shown in Figure A.2.1 as an example. It is obvious that the quartz substrate did not contribute to the scintillation light detected in the TPB temperature sweep. Events are clustered around zero charge, similar to the events which were removed from the light yield distribution shown in Figure 4.5.1. It is likely that these events are due to random coincidences between the PMTs.

A.3 Baseline Effects

The baseline is calculated as the mean of the first 1/32 of the pre-trigger in each event. It is determined on-the-fly before the pulse integrals are calculated, and is then subtracted from the pulse integrals. Because of this, there was a concern that the baseline was over-estimated in situations where the tail from the last event leaked into

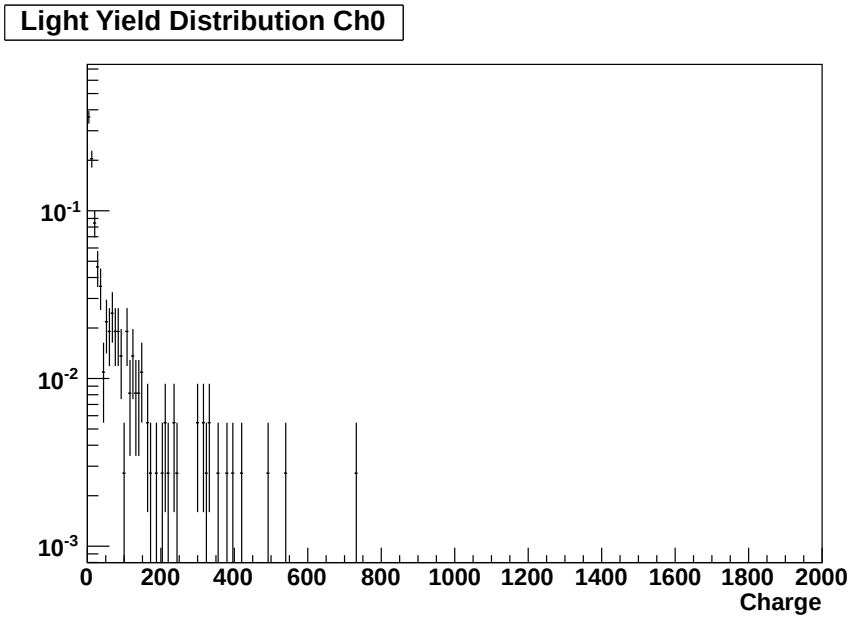

Figure A.2.1: Detected light from a blank quartz run at 87 K.

the current event, thus contributing to the measured baseline. In order to investigate these, one searches for a trend between the time from the previous event, and the current event's baseline. The closer together two events are, the more likely it is that the measured baseline is influenced by the previous events tail, and so a trend between these two variables should manifest itself.

We provide data from the 100 K measurement. Figure A.3.1 suggests that this is not a significant effect for our measurement as there is no visible trend between time from last event and measured baseline - instead, for all events, the baseline seems to centre around an approximate mean of 375 (arbitrary units).

To verify that there is no trend, we histogram the baseline according to slices of time. Figure A.3.2 displays histograms of the measured baseline between various time intervals. The mean values of these histograms are 372.2 V, 366.5 V, 371.4 V,

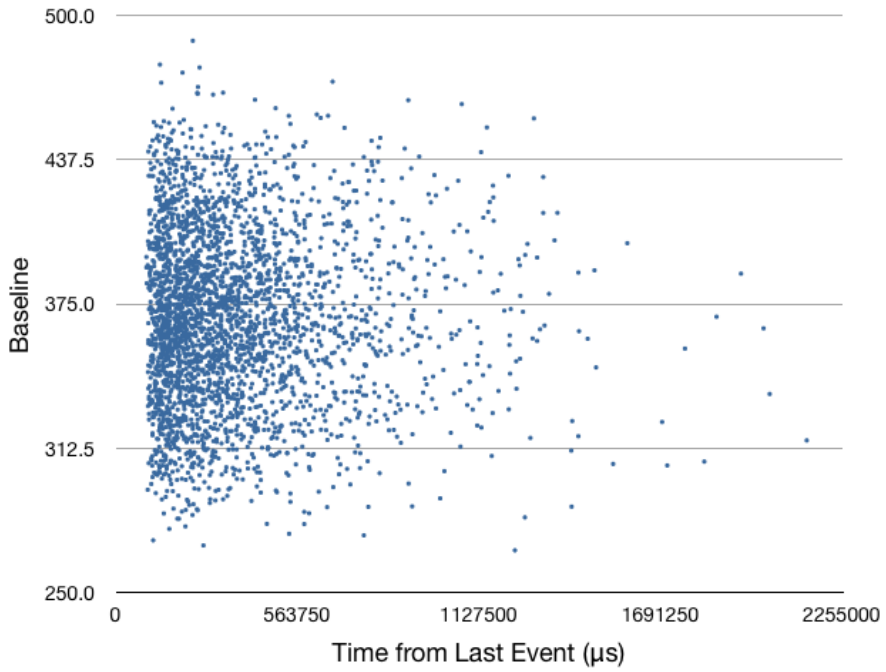

Figure A.3.1: Scatter plot of measured baseline with respect to time from last event.

368.6 V, and 365.8 V respectively. There is evidently no obvious affect on the measured baseline due to the time from last event.

A.4 Ringing

One possible explanation of the width-1 low charge pulses (refer to Chapter 4 Figure 4.5.8) was that they were caused by the so-called "ringing" effect. This was considered a possibility due to the decay of the low-charge pulses, which followed the decay of the rest of the signal as one would expect if ringing were to occur. Ringing is simply the reflection of signal due to, for example, incorrect inductance in connections of the anode and adjacent dynodes, or output signals which do not have

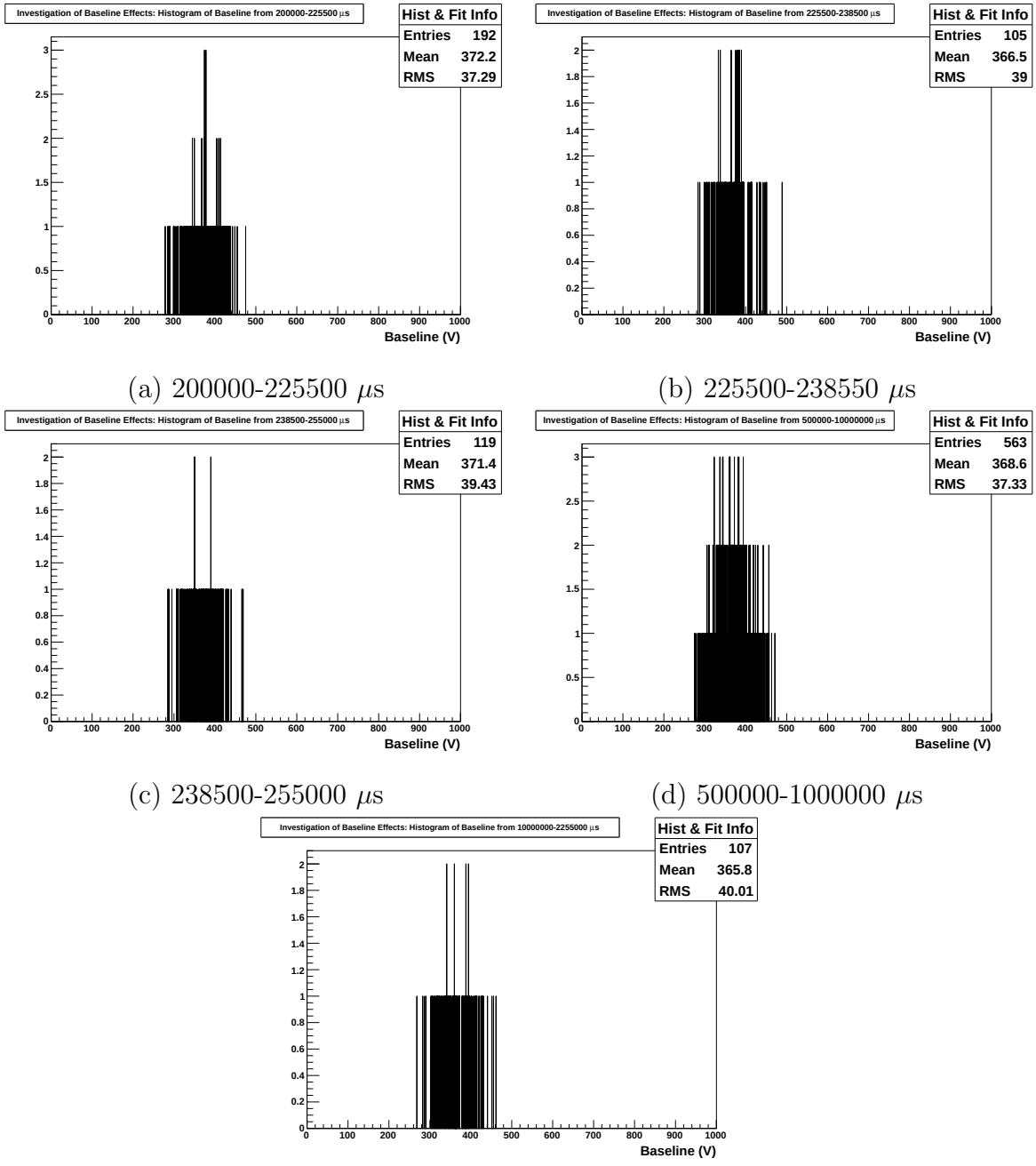

(a) 200000-225500 μs

(b) 225500-238550 μs

(c) 238500-255000 μs

(d) 500000-1000000 μs

(e) 10000000-2255000 μs

Figure A.3.2: Histogram of measured baseline for various time intervals, listed directly below the histograms shown here. The time intervals represent the time since previous event (i.e.: the time values on the x-axis of Figure A.3.1).

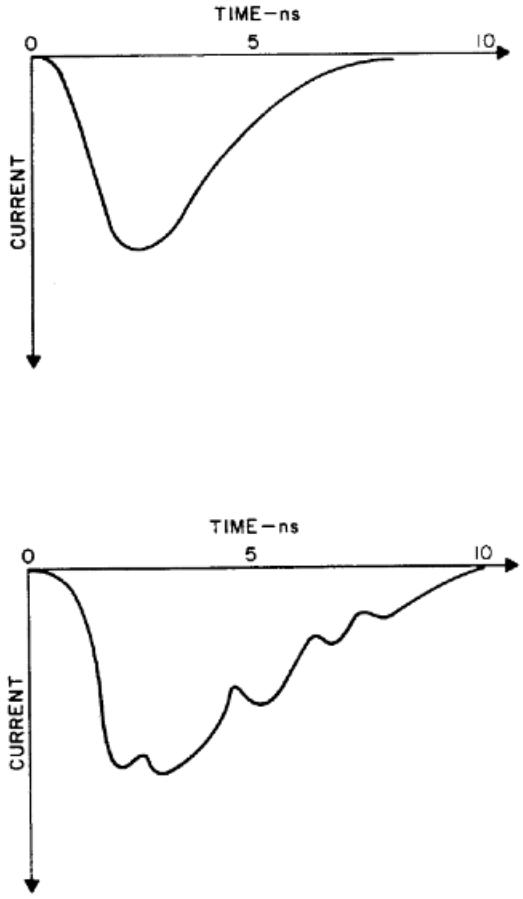

Figure A.4.1: Upper: Correct pulse. **Lower**: "Ringing" due to resonances in the connections for the anode and dynodes [20]

a controlled output impedance to match the coaxial cable which carries the signal. Such imperfections cause resonances in the signal, leading to the multiple detections of individual pulses [20]. Figure A.4.1 demonstrates a correct pulse in comparison to one affected by such resonances.

If the low-charge events were indeed caused by ringing, one would expect to see an overabundance of specific time differences (i.e.: $t_i - t_j$), leading to peaks in a

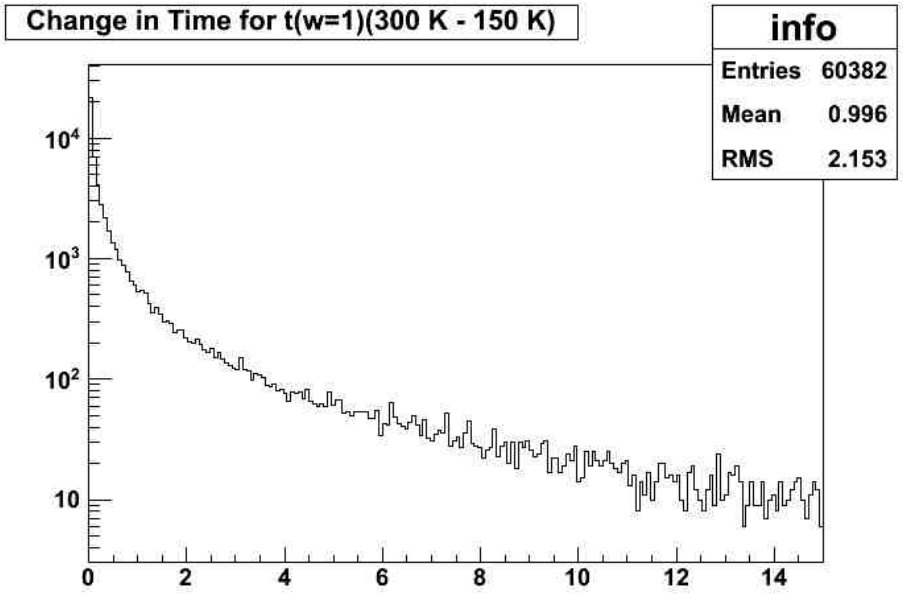

Figure A.4.2: Histogram of time differences (in μs) from width-1 low charge pulses, and the pulses immediately preceding them.

histogram distribution of either time from last pulse, or time differences between all pulses within events. Figures A.4.2 and A.4.3 demonstrate that no evidence of ringing can be found in the data.

A.5 A Deeper Look into Pulse Width

A.5.1 Temperature

The late charge distributions do not show different characteristics at different temperatures, as expected since the PMT's are kept at room temperature (see Figure A.5.1).

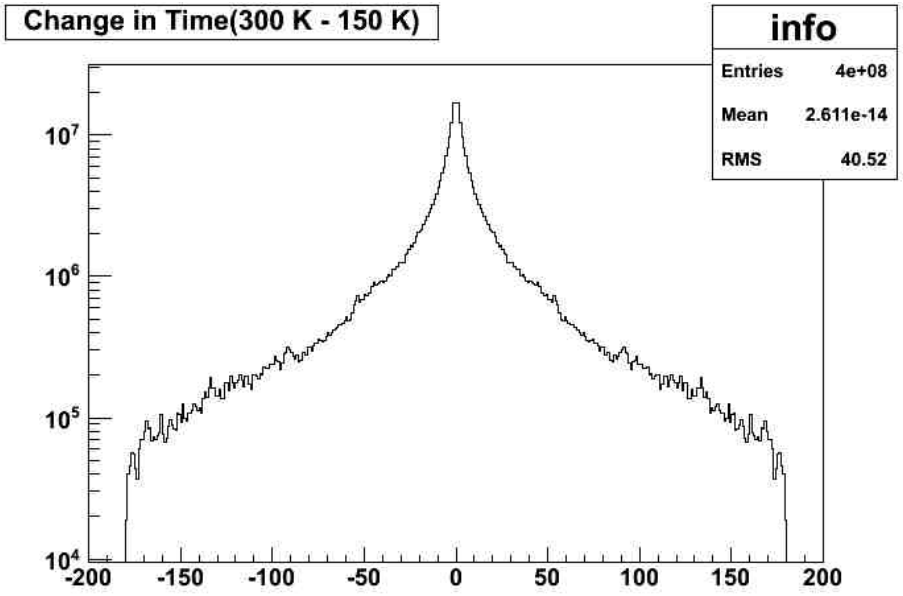

Figure A.4.3: Histogram of time differences (in μs) of all pulses within events.

A.5.2 Timing

The late charge distributions do not appear to depend on the timing windows used, other than a greater number of higher width pulses occurring earlier on in the pulse shapes (Figure A.5.2). This is not unexpected, since a larger portion of the scintillation pulse occurs in the prompt time window.

A.6 Systematic Uncertainties

In order to measure the time constants of the pulse shapes, the timing resolution, single photoelectron charge, and single photoelectron efficiency were determined. As an estimation of the systematic uncertainties on the pulse shape fits, these values were varied according to their error, and the fitting procedure was performed once more.

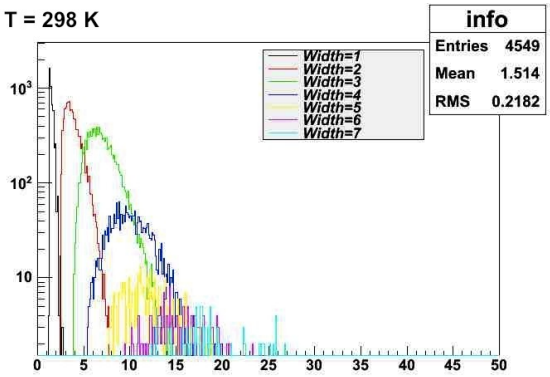

(a) Histogram of late charge according to width at 298 K.

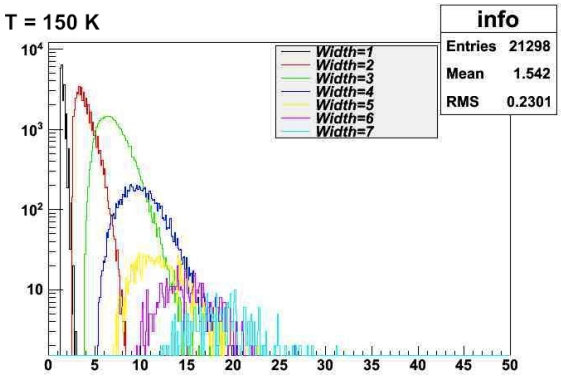

(b) Histogram of late charge according to width at 150 K

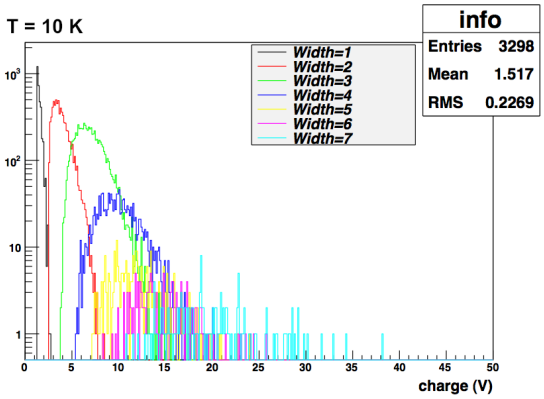

(c) Histogram of late charge according to width at 10 K

Figure A.5.1: Comparison of width distributions according to temperature.

The timing resolution was varied between 1.5 to 2.5 ns, while the single photoelectron charge, as measured by [28], was varied between 5.099 and 5.113 V.

For single photoelectron efficiency, the efficiency of the PMTs used in the TPB measurement were first determined to be 85% by [86]. Of course, we could not redo the measurement with a lowered threshold, so to get an idea of the effect this had on our data, we multiplied all charge measurements less than 10 V (chosen as an upper limit on the single photoelectron charge - see Figure 4.5.13 from Chapter 4) by 1.85 to artificially "boost" the single photoelectron charge in the data.

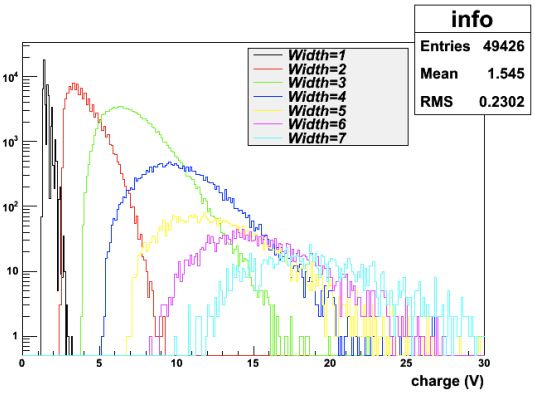

(a) Histogram of late charge according to width at 298 K to 150 K, from 20 μs to 50 μs.

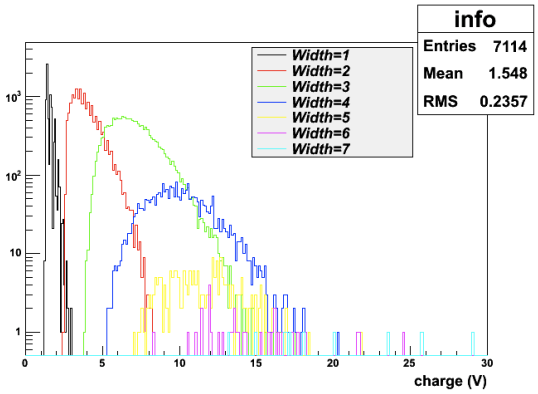

(b) Histogram of late charge according to width at 298 K to 150 K, from 50 μs to 100 μs.

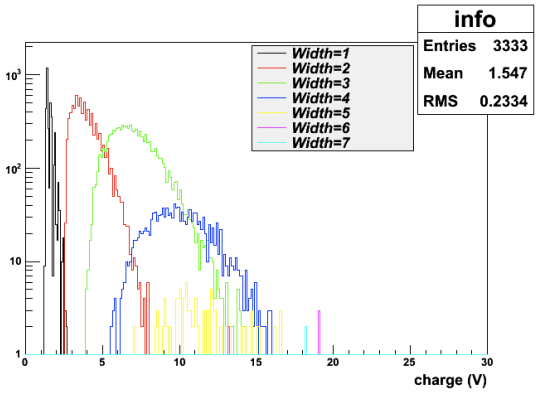

(c) Histogram of late charge according to width at 298 K to 150 K, from 100 μs to 100 μs.

Figure A.5.2: Comparison of width distributions according to time window.

These procedures were done at several sample temperatures between 300 K and 10 K, and the largest difference in the resulting fit values was taken as the systematic error for each effect. The errors were then added quadratically.

The results of this investigation are shown in Table A.1.

Parameter	Systematic Error
N_1	0.0003 (0.3)
N_2	0.0008 (0.5)
N_3	0.00006 (0.05)
N_4	0.00007 (0.06)
τ_1	0.01 μs
τ_2	0.1 μs
τ_3	0.5 μs
τ_4	1.5 μs
c_0	0.0000012 (0.001)

Table A.1: Systematic errors for pulse shape distribution. Note that the N_1 to N_4, and c_0 errors in brackets are for the normalized parameters.

	N1	t1	N2	t2	N3	t3	N4	t4	c0
N1	1	-0.70972	0.023406	0.021984	-0.021556	0.0034476	-0.015605	-0.015225	0.027579
t1	-0.70972	1	0.05663	0.10397	-0.0010355	0.066148	-0.043159	0.041281	-0.028893
N2	0.023406	0.05663	1	0.85338	0.036589	0.81699	-0.58207	0.4934	-0.31731
t2	0.021984	0.10397	0.85338	1	-0.015254	0.73728	-0.52471	0.43024	-0.272
N3	-0.021556	-0.0010355	0.036589	-0.015254	1	0.4615	-0.59159	0.72358	-0.56897
t3	0.0034476	0.066148	0.81699	0.73728	0.4615	1	-0.80265	0.75546	-0.52755
N4	-0.015605	-0.043159	-0.58207	-0.52471	-0.59159	-0.80265	1	-0.63125	0.29499
t4	-0.015225	0.041281	0.4934	0.43024	0.72358	0.75546	-0.63125	1	-0.84864
c0	0.027579	-0.028893	-0.31731	-0.272	-0.56897	-0.52755	0.29499	-0.84864	1

Figure A.7.1: Correlation matrix for the pulse shape fit at 87 K.

A.7 Correlations in the Pulse Shape Fits

Because it was necessary to introduce four time constants to adequately fit the pulse shapes from the TPB data, it is inevitable that certain parameters in the fit will be correlated. We provide here a typical correlation matrix for the pulse shape fits, at a sample temperature of 87 K (Figure A.7.1). The best we could do here was to vary fit parameters in order to ascertain the effects these correlations have on the final fit values. It was found that the systematic errors, as discussed above, are much larger than this effect.

A.8 Additional Light Yield and Pulse Shape Plots

Here we provide sample plots for the light yield (Figure A.8.1) distributions and pulse shape histograms (Figure A.8.2) at 298 K, 27 K, and 10 K.

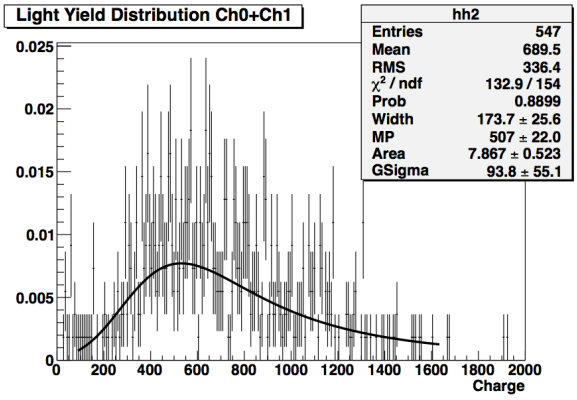

(a) Histogram of detected light at 298 K.

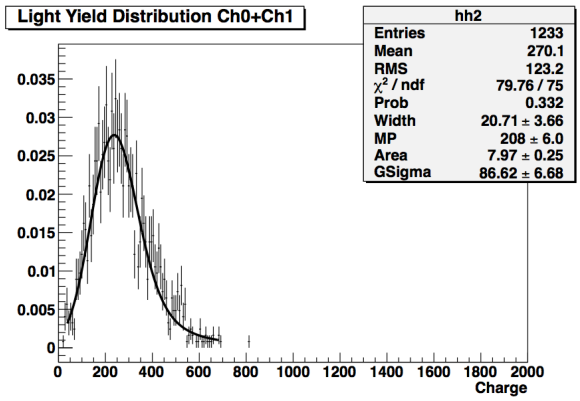

(b) Histogram of detected light at 27 K.

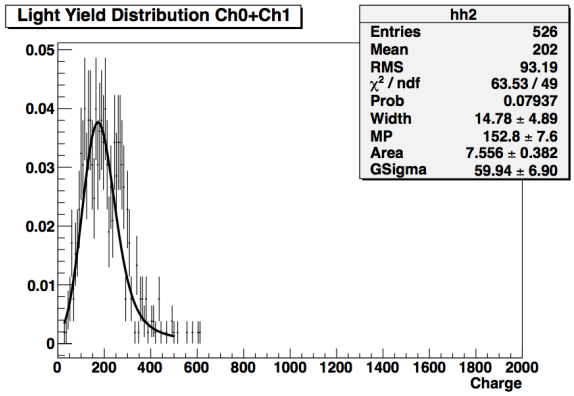

(c) Histogram of detected light at 10 K.

Figure A.8.1: Typical detected light distributions at various temperatures.

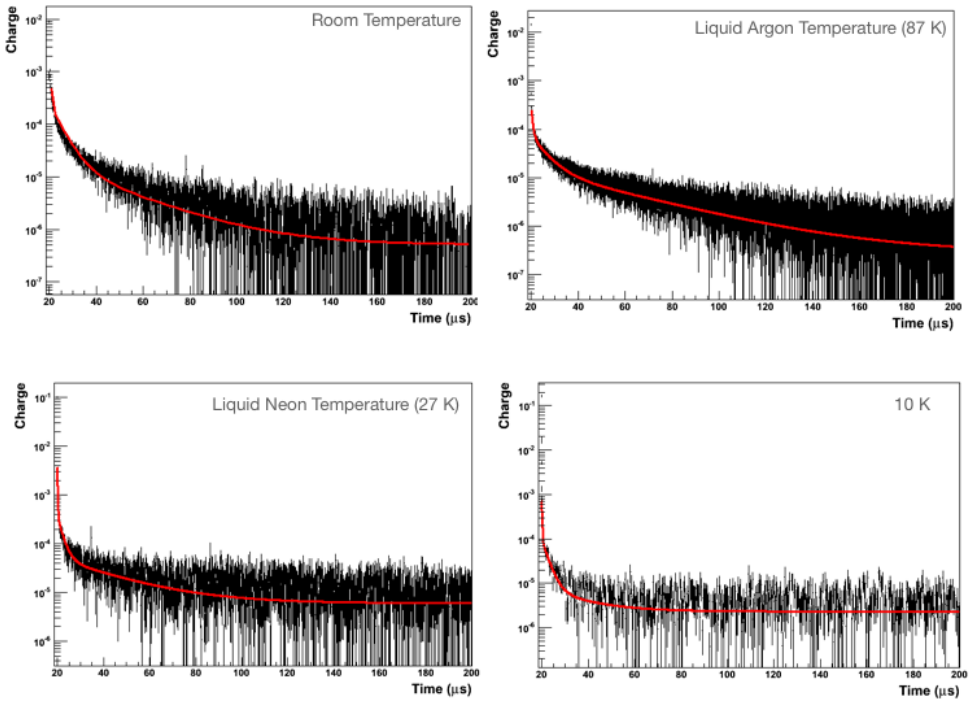

Figure A.8.2: Typical pulse shape distributions at various temperatures, normalized for comparison purposes, with constant bin size.